



VYSOKÉ UČENÍ TECHNICKÉ V BRNĚ
BRNO UNIVERSITY OF TECHNOLOGY



FAKULTA STROJNÍHO INŽENÝRSTVÍ
ÚSTAV PROCESNÍHO A EKOLOGICKÉHO
INŽENÝRSTVÍ
FACULTY OF MECHANICAL ENGINEERING
INSTITUTE OF PROCESS AND ENVIRONMENTAL
ENGINEERING

COMPUTATIONS OF FLUID FLOW AND HEAT TRANSFER FOR DESIGN OPTIMIZATION OF TUMBLE CLOTHES DRYER

VÝPOČTY PROUDĚNÍ A PŘENOSU TEPLA PRO OPTIMALIZACI KONSTRUKCE BUBNOVÉ
SUŠICKY PRÁDLA

DIPLOMOVÁ PRÁCE
MASTER'S THESIS

AUTOR PRÁCE
AUTHOR

Bc. MARTIN ČERMÁK

VEDOUCÍ PRÁCE
SUPERVISOR

doc. Ing. JIŘÍ HÁJEK, Ph.D.

BRNO 2013

This page has been intentionally left blank

This page has been intentionally left blank

Anotace

V rámci této práce byla provedena komplexní analýza elektricky vyhřívané bubnové sušičky prádla s cílem identifikovat možnosti optimalizace její konstrukce vedoucí ke zlepšení přestupu tepla. Pro řešení byl zvolen postup využívající výpočtovou dynamiku tekutin (CFD). K dosažení dostatečně detailního popisu zadaného problému byl využit komerční software Fluent společně se speciálně vyvinutým modelem přenosu tepla.

Klíčová slova

Bubnová sušička prádla, elektrické vytápění, spirálové topné těleso, CFD, model přenosu tepla, optimalizace

Annotation

Within this thesis a complex analysis of an electrically heated tumble clothes dryer was performed in order to identify design optimization possibilities leading to an improvement of a heat transfer. A computational fluid dynamics (CFD) approach involving an employment of the commercial software Fluent and development of a custom heat transfer model was selected to resolve the problem in a required level of detail.

Keywords

Tumble clothes dryer, resistance heating, helically coiled heating wire, CFD, heat transfer model, optimization

Bibliografická citace této práce

dle ČSN ISO 690

ČERMÁK, M. *Výpočty proudění a přenosu tepla pro optimalizaci konstrukce bubnové sušičky prádla*. Brno: Vysoké učení technické v Brně, Fakulta strojního inženýrství, 2013. 69 s. Vedoucí diplomové práce doc. Ing. Jiří Hájek, Ph.D..

Prohlášení o původnosti práce

Prohlašuji, že jsem tuto práci vypracoval samostatně s využitím uvedených zdrojů,
na základě konzultací a pod vedením vedoucího diplomové práce.

V Brně dne 23. května 2013

.....

Martin Čermák

Table of contents

1	List of symbols	9
2	Introduction	12
3	Tumble dryer description	13
3.1	Air flow characteristics	13
3.2	Electric heating.....	15
3.3	Drivetrain and regulation	17
4	Solution method overview	18
4.1	Heat transfer model	18
4.2	Fluid-wire interaction	19
5	Heat transfer model	20
5.1	Development of elemental relationships.....	20
5.1.1	Heat generation rate	20
5.1.2	Heating wire energy equation.....	21
5.1.3	Discretization of the heating wire energy equation.....	23
5.1.4	Convection heat transfer coefficient.....	25
5.1.5	Three phase circuit solution	26
5.2	Model description	28
5.3	Model abilities and limitations	30
5.4	Implementation.....	31
5.4.1	Flow field data export.....	32
5.4.2	Calculation of the volumetric heat source terms	33
5.4.3	Linear systems definition.....	38
6	Present Case CFD Analysis	41
6.1	Computational Domain and Boundary Conditions	41
6.2	Computational grid.....	44
6.3	Solver.....	47
6.4	Solution process	48
7	Results interpretation	52
7.1	Flow field	52
7.1.1	Heating blocks	52
7.1.2	Outlet.....	53
7.2	Heating unit	54
8	Optimization	57
8.1	Targeting.....	57
8.1.1	Overheating.....	57

8.1.2	Flow uniformity	61
8.1.3	Heating channel velocity	63
8.1.4	Heating coil geometry	66
8.2	Evaluation of optimization possibilities.....	67
9	Conclusion	68
10	References.....	69

Appendix A – Fluent UDF source code

Appendix B – Heat transfer model Matlab code

Appendix C – CFD results visualizations

Appendix D – Attached DVD content

1 List of symbols

Symbol	Description	Unit
A	Linear system coefficient matrix	-
A_{CONV}	Convective heat transfer heat exchange area	m^2
$A_{CONV,CV}$	Convective heat transfer heat exchange area at the control volume	m^2
A_{HB}	Cross-sectional area of the heating block channel.	m^2
A_{CH}	Cross-sectional area of the outlet channel	m^2
A_{RAD}	Radiation heat transfer heat exchange area	m^2
A_W	Heating wire cross-sectional area	m^2
\vec{b}	Vector of right hand sides	-
C_j^+	Discretized wire energy equation constant term	-
C_j^-	Discretized wire energy equation constant term	-
D	Outer diameter of the heating coil	m
d	Wire diameter	m
d_{eq}	Equivalent diameter	m
I	Current	A
I_{AMP}	Amplitude of a current	A
$I_{AMP,a}$	Amplitude of the current in a branch	A
$I_{AMP,b}$	Amplitude of the current in b branch	A
$I_{AMP,c}$	Amplitude of the current in c branch	A
I_{RMS}	Root mean square value of a current	A
I_Y	Y-index	-
I_Z	Z-index	-
I_W	Wire-index	-
$I_{W,CV}$	Wire-index at the control volume	-
I_B	Branch-index	-
I_{BR}	Vector of branch currents	A
I_{WB}	Wire-branch-index	-
k	Thermal conductivity of the wire material	$W \cdot m^{-1} \cdot K^{-1}$
L_C	CFD cell length	m
L_{CV}	Control volume length	m
L_{COIL}	Heating coil length	m
L_W	Heating wire length	m
\overline{Nu}	Average Nusselt number	-
n_B	Number of branches	-
n_{CVB}	Number of control volumes in one branch	-
n_{DRUM}	Drum rotation speed	min^{-1}
n_{HB}	Number of heating blocks in the considered heating unit configuration	-
n_{WB}	Number of wires in one branch	-
n_{ZU}	Number of elements in \vec{z}_{COORD} vector	-
P	Power	W
P_{AVG}	Average power	W
Pr	Prandtl number	-
\dot{Q}_{GEN}	Generated heat per unit time	W
\dot{Q}_{CONV}	Convective heat flux	W
\dot{Q}_{CV}	Transferred heat at the control volume per unit time	W
\dot{Q}_{RAD}	Radiation heat flux	W

$\dot{Q}_{COND,L}$	Conductive heat flux at the left wire boundary	W
$\dot{Q}_{COND,R}$	Conductive heat flux at the right wire boundary	W
R	Electric resistance	Ω
R_{1m}	Electric resistance of one meter of the heating coil	Ω
$R_{0,CV}$	Electric resistance at the control volume at the reference temperature	Ω
R_a	Electric resistance of the branch a	Ω
R_b	Electric resistance of the branch b	Ω
R_c	Electric resistance of the branch c	Ω
\vec{R}_{BR}	Vector of branch electric resistances	Ω
R_{br}	Branch resistance at the reference temperature (measured value)	Ω
\bar{R}	Branch resistance (overheating analysis)	Ω
Re	Reynolds number	-
r_{DRUM}	Drum radius	m
S_C	Helix pitch	m
$S\dot{Q}_{CV}$	Volumetric heat generation rate at the control volume	$W \cdot m^{-3}$
T_{AMB}	Ambient temperature	$^{\circ}C$
T_C	Air temperature at the CFD cell	$^{\circ}C$
T_{CV}	Air temperature at the control volume	$^{\circ}C$
T_{RS}	Temperature of remote surface (radiation)	$^{\circ}C$
T_{R0}	Electric resistance reference temperature	$^{\circ}C$
\vec{T}_W	Vector of unknown wire temperatures	$^{\circ}C$
\bar{T}_W	Average branch wire temperature	$^{\circ}C$
$T_{W,CV}$	Wire temperature at the control volume	$^{\circ}C$
V	Voltage	V
V_{amp}	Voltage amplitude	V
\dot{V}_{AIR}	Volumetric air flow rate	$m^3 \cdot h^{-1}$
V_{an}	Phase-to-neutral voltage	V
V_{bn}	Phase-to-neutral voltage	V
V_{cn}	Phase-to-neutral voltage	V
V_{aN}	Phase-to-midpoint voltage	V
V_{bN}	Phase-to-midpoint voltage	V
V_{cN}	Phase-to-midpoint voltage	V
V_N	Midpoint voltage	V
V_{RMS}	Root mean square value of voltage	V
v_{DRUM}	Drum velocity	$m \cdot s^{-1}$
\bar{v}_{HB}	Average heating channel velocity	$m \cdot s^{-1}$
v_{CX}	CFD cell x velocity	$m \cdot s^{-1}$
v_{CY}	CFD cell y velocity	$m \cdot s^{-1}$
v_{CZ}	CFD cell z velocity	$m \cdot s^{-1}$
v_{CV}	Control volume velocity	$m \cdot s^{-1}$
vol_C	CFD cell volume	m^3
vol_{CV}	Volume of CFD cells within one control volume	m^3
x_C	CFD cell centroid x coordinate	m
x_{CV}	Control volume x coordinate	m
x_L	X coordinate of the left wire boundary	m
y_{BC}	Heating block center point y coordinate	m
y_C	CFD cell centroid y coordinate	m
y_{AMP}	Amplitude of a general function	-

z_C	CFD cell centroid z coordinate	m
z_{COORD}	Vector of unique z CFD cell coordinates	m
α	Convective heat transfer coefficient	$W \cdot m^{-2} \cdot K^{-1}$
$\bar{\alpha}$	Overall convective heat transfer coefficient	$W \cdot m^{-2} \cdot K^{-1}$
α_{CV}	Convective heat transfer coefficient at the control volume	$W \cdot m^{-2} \cdot K^{-1}$
β	Resistivity temperature coefficient	K^{-1}
Δx_w	Wire element length	m
ε	Emissivity	-
λ_{air}	Thermal conductivity of air	$W \cdot m^{-1} \cdot K^{-1}$
ρ	Resistivity	$\Omega \cdot m$
ρ_0	Resistivity at the reference temperature	$\Omega \cdot m$
σ	Stefan-Boltzmann constant	$W \cdot m^{-2} \cdot K^{-4}$
ψ	Overheating factor	-
ω	Overheated region ratio	-

2 Introduction

The topic of this thesis arose from the collaboration between the laundry equipment manufacturer Primus CE and NETME Centre – a research and development center attached to the Faculty of Mechanical Engineering at Brno University of Technology. During the initial talks aimed at the details of the collaboration, the need to address an optimization of electrically heated tumble clothes dryers was expressed by the Primus company representatives. As a result the task of this thesis was formulated.

To ensure an appropriate selection of a solution method, a further discussion revealing the details of the task was necessary. Since the dryer geometry was designed in the time when tools such as computational fluid dynamics (CFD) were not available, the main concern of the manufacturer was the influence of the geometry on the heat transfer. A special emphasis was placed on an investigation of overheating and its connection with the dryer design.

The view of the problem from a broader perspective perfectly represents the changes in engineering in the current era. Great improvements in computer power and software development allow the manufacturers of standard domestic appliances to utilize tools such as the abovementioned CFD to improve a design and therefore to support a competitiveness of the company. Even though in many cases it is still unsuitable to employ purely computational methods and an experimental work together with experienced personnel able to predict the relevant dependencies prevails, a number of industrial applications of numerical problem solutions has been increasing significantly in the last few years. In this context it is essential to mention the frequent misuse of commercial CFD or FEM packages leading to completely incorrect results. These situations underline a great value of know-how required to achieve relevant results in simulations of a fluid flow or in other applications of FEM/FVM methods.

The structure of the thesis can be split into two main logical parts. In the first part all the steps necessary to obtain data crucial for a description of the present case are presented. The second part investigates improvement possibilities in both qualitative and quantitative ways.

3 Tumble dryer description

A tumble clothes dryer is a standard domestic appliance that uses hot air to remove moisture from wet laundry. Depending on a target customer, there are several conventional energy sources used for air heating. While small domestic tumble dryers use electric energy, larger industrial dryers can be equipped with steam or gas burner heating. This thesis is concerned with the electrically heated variants.



Fig. 1 - Layout of Primus T24/T35 tumble clothes dryer [5]

Fig. 1a shows a layout of the high capacity tumble clothes dryer produced by the Primus company. In the highest capacity series there are currently two models available – T24 and T35. The main difference between the two models lies in the volume of the drum and heating unit power. Because the drum diameter is identical for the both models, the larger volume of T35 is achieved by increasing the drum length and therefore the depth dimension of the whole device, as can be seen in fig. 1b.

3.1 Air flow characteristics

The flow through the dryer described above can be characterized as a suction based fan driven flow with significant heat and mass transfer. Drying air enters the device through the set of perforations located at the back side of the dryer and continues upwards through the inlet channel. Fig. 2 shows the visualization of the dryer with and without the back cover. It can be seen that inlet channel is partly blocked by the drivetrain which influences the flow immediately after the entry.

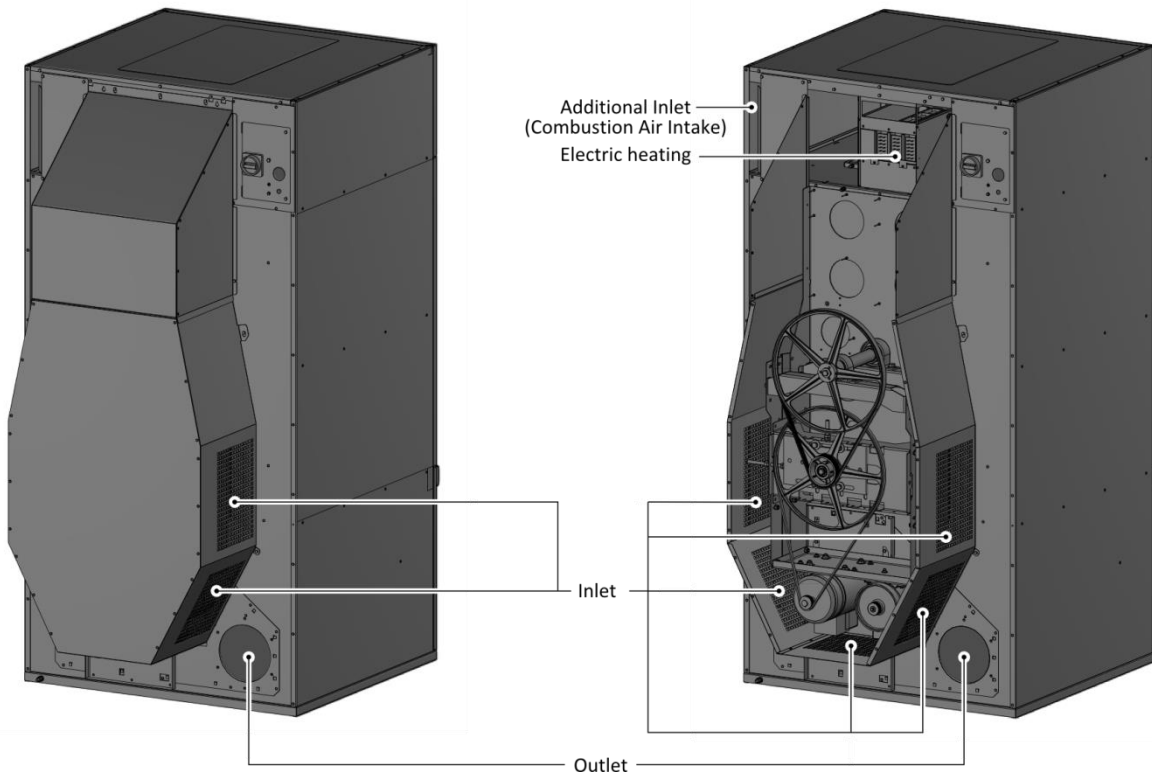


Fig. 2 - Back view of the T24/T35 dryer

As the air reaches the top of the inlet channel, it is forced to change a direction and enter the top chamber where the heating unit is installed. It is important to note now that in the top left corner of the chamber there is an additional opening through which additional air is being sucked into the device. The main purpose of this opening is to provide combustion air for the gas version of the dryer, nevertheless with regard to the parts unification tendencies it is also present in the version with electric heating.

After the air passes through the heating unit it reaches the region where it interacts with the rotating perforated drum. As a result the stream splits into two parts. The air that penetrates the drum forms the main drum flow which gets in contact with wet laundry and absorbs excessive moisture. The part of the air that is pulled to the side by the drum rotation flows around the drum and forms the bypass flow which does not participate in the drying process. Fig. 3a and fig. 3b illustrate the internal dryer geometry and the sectional view of the region where the abovementioned stream splitting takes place.

The last part air has to pass before entering a fan is a fluff filter which prevents cloth particles and other impurities from getting into the fan and consequently into a duct system.

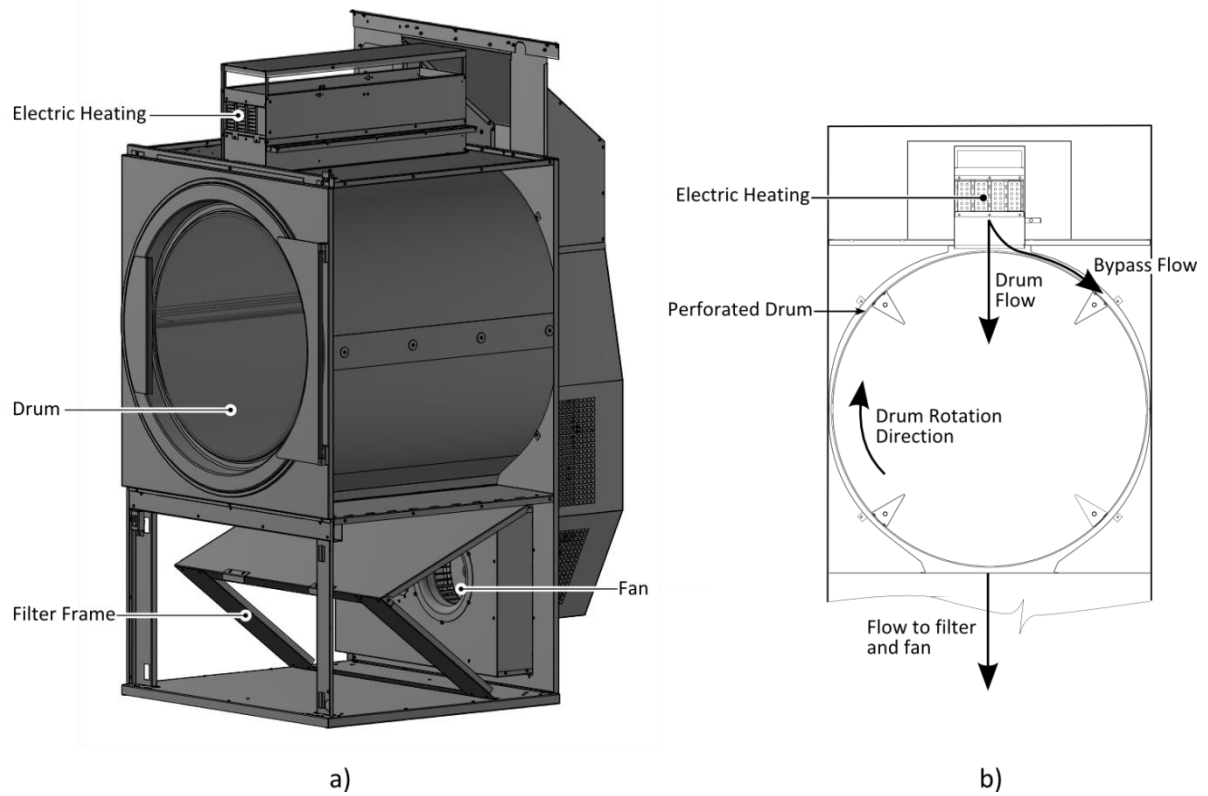


Fig. 3 – Front and sectional view of T24/T35 dryer

3.2 Electric heating

Heating unit used in the electric models of T24/T35 dryer is based on the unified frame which is identical for all the heating power variations. Overall heating power is achieved by appropriate combination of heating blocks with the nominal power of 4.5 KW and 6 KW.

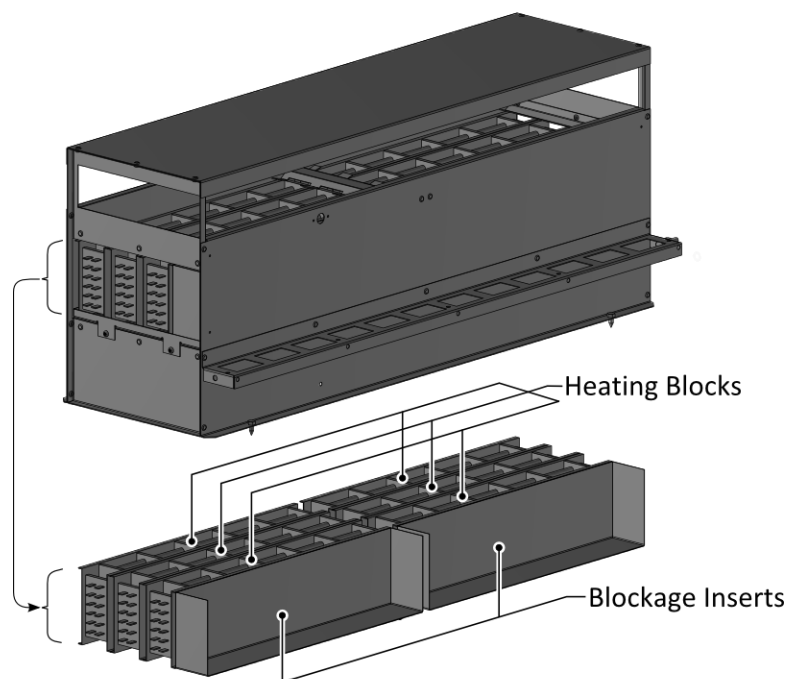


Fig. 4 – Heating unit visualization

From fig. 4 it is clear that when less than eight blocks is used, blockage inserts are placed into all empty slots in order to prevent the air from bypassing the heating channel. The distributions of heating blocks and blockage inserts in 30, 36 and 48KW variants are shown in fig. 5a, fig. 5b, and fig. 5c respectively. Within the scope of this thesis the 36KW variant was further examined. However an emphasis was placed on a simple applicability of developed solution methods to all the heating unit configurations.

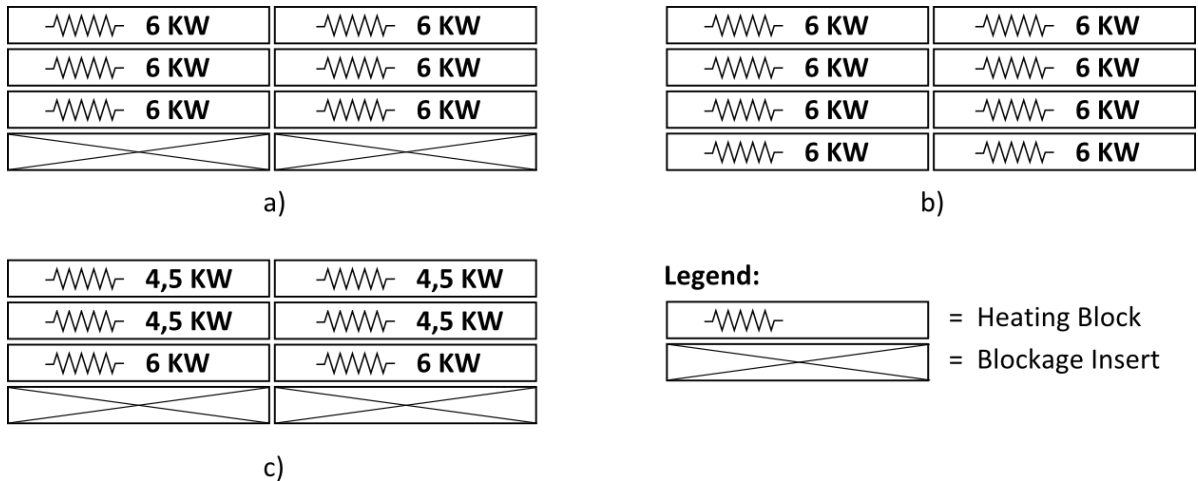


Fig. 5 – Distribution of heating blocks in a) 36KW b) 48KW c) 30KW heating unit

The heating block, depicted in fig. 6a, is a simple device consisting of three basic parts – heating wires formed into helical coils, wire supports and a terminal board. As can be seen from fig. 6b, a set of twelve wires is divided into three branches. One branch is formed by four wires connected in series. The terminal board contacts allow the heating block to be connected in a variety of ways. In the considered case a three phase wye connection with absent neutral line has been used. The electric circuit diagram of the connection is shown in fig. 6c.

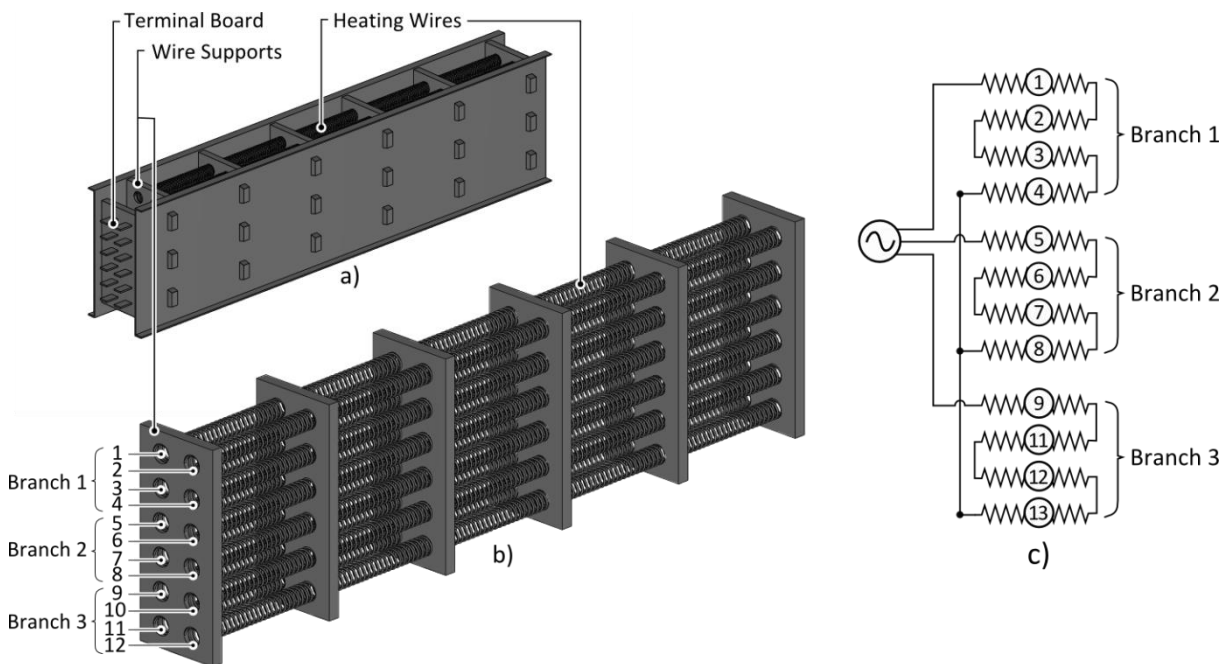


Fig. 6 – Heating block description

As has been mentioned above, there are two variants of heating blocks used to form the heating unit of the required power. The difference in power is achieved by changing the heating wire diameter and adjusting the helix parameters. In both variants the outer block dimensions and materials are identical. Tab. 1 summarizes the parameters of 6 KW and 4.5 KW heating blocks.

	6 KW	4,5 KW
Wire diameter [mm]	0.8	0.7
Helix pitch [mm]	2.4	2.3
Helix outer diameter [mm]	8	7.6

Tab. 1 - Heating blocks parameters

3.3 Drivetrain and regulation

The energy necessary to drive the drum and the fan is supplied by either one or two electric motors. The single motor configuration is used in models where the drum rotates only in one direction, whereas in the models with drum reversal possibility a double motor configuration is required to drive the fan and the drum separately. In both cases a rotational speed is constant and it is not being regulated by the control unit.

The most important parameters of the drying process are the air flow rate and the air temperature. Because the present design of the dryer does not allow a regulation of the heating unit power, the two abovementioned parameters are coupled together. Therefore the optimal air flow rate is necessary to keep the air temperature within an allowed range. This is achieved by placing a throttle in the outlet channel. Since the flow rate is affected by a head loss of a duct system through which the humid air leaves the facility where the dryer is installed, the throttle has to be adjusted during the installation process to balance the duct system head loss.

In order to prevent the laundry from overheating, a thermocouple is installed bellow the heating unit in the position shown by fig. 7. The thermocouple is connected to the control unit which breaks the heating unit electric power supply when the measured temperature exceeds a given limit.

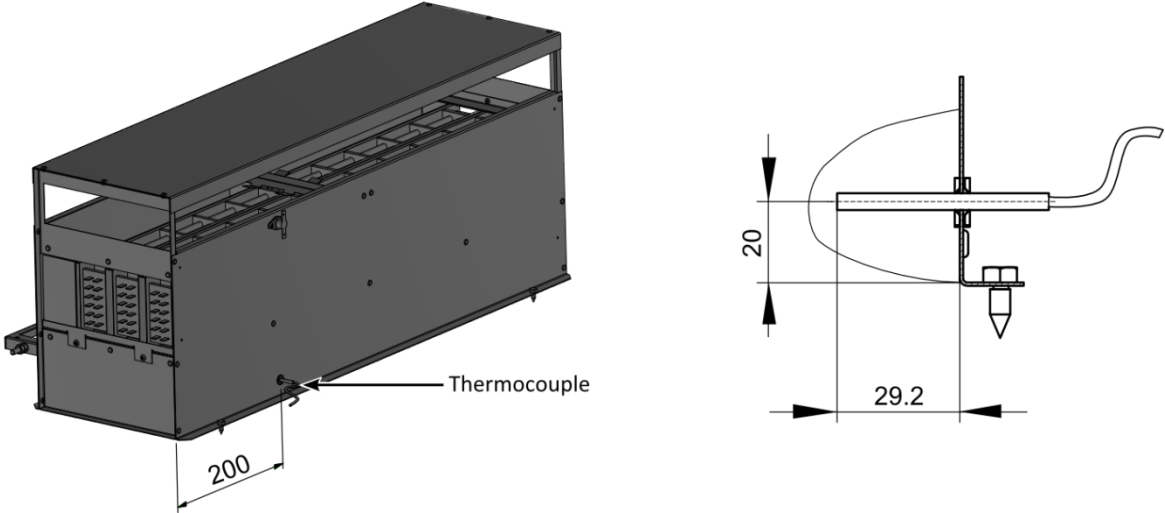


Fig. 7 – Temperature regulation sensor position

4 Solution method overview

In order to allow a reader to be aware of all the logical connections, this chapter aims to give the basic solution procedure overview and to discuss the elemental features and simplifications. The details of individual steps can be found in the subsequent chapters.

With regard to the optimization nature of the task, a solution method capable of resolving the flow field details is needed in order to identify the improvement possibilities. This need is fully met by computational fluid dynamics (CFD) approach which has therefore been selected as the main solution method. While leaving the CFD details to be sought in one of the many literature sources, brief description can be formulated as following. The fluid flow governing equations describing the elemental fluid flow laws are applied to the discretized flow domain which results in a system of equations. The converged numerical solution of the system reveals the values of all the flow variables at each cell of the discretized domain.

The assessment of the flow domain discretization possibilities has identified the need to further analyze the discretization method of the helically coiled heating wires region. Because a full discretization of the region adjacent to the heating wires requires a high number of cells resulting in high computing power requirements, a simplified approach was sought. From a general engineering point of view, it is common to employ a modeling approach. When applied to the considered case, the modeling approach avoids the detailed resolution of the heating wire region and introduces a computational relationship which is able to describe the heat transfer and fluid-wire interaction based on the main flow variables and experimental values. In this particular case the helical coil geometry was replaced by the substitutive geometry shown in fig. 8 and subsequently an alternative implementation of the heat transfer and fluid-wire interaction was introduced.



Fig. 8 – Visualization of the substitutive geometry

4.1 Heat transfer model

In order to describe the selected heat transfer modeling approach, it is appropriate to start with the formulation of the energy equation used by CFD solvers. Ansys Fluent, the CFD solver to be used in this case, solves the energy equation in the form:

$$\frac{\partial}{\partial t}(\rho E) + \nabla \cdot (\vec{v}(\rho E + p)) = \nabla \cdot \left(k_{eff} \nabla T - \sum_j h_j \vec{J}_j + (\bar{\tau}_{eff} \cdot \vec{v}) \right) + S_h \quad Eq. 4.1$$

where the left hand side represents the time and convective derivatives of the total energy, the first three terms on the right hand side represent the energy transfer because of the conduction, species diffusion and viscous dissipation respectively and where S_h is the volumetric heat source term as described in Ansys Help [1]. The last mentioned term is essential for the model formulation. Based on the heat transfer calculation described below, the volumetric heat source terms of the substitutive geometry cells are set and therefore the air passing through the cells is heated up. This situation is demonstrated on the test case shown in fig. 9a, fig. 9b and fig. 9c. Fig. 9a shows the domain discretization, fig. 9b highlights the cells where the volumetric heat sources are applied and fig. 9c visualizes the resulting temperature field where white and red colors represent low and high temperatures respectively.

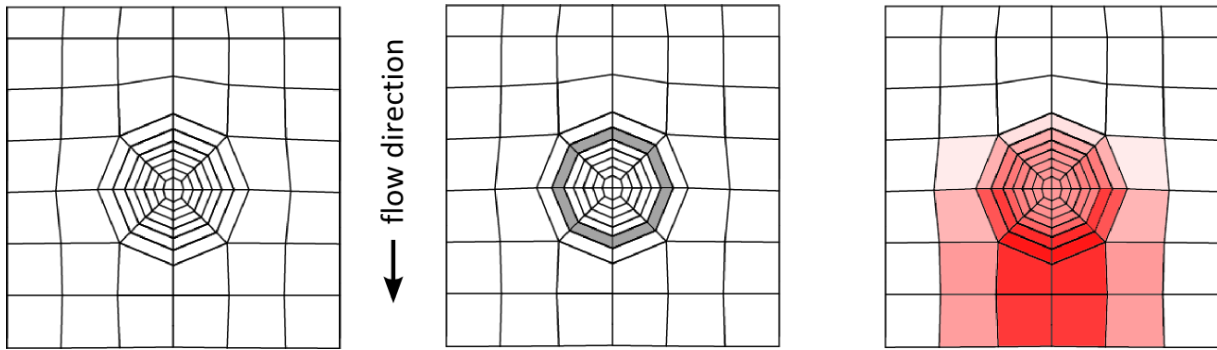


Fig. 9 – Illustration of volumetric heat source terms utilization.

The model utilizes experimental studies of convective heat transfer coefficients from helically coiled wires in cross flow performed by Comini et al.[3] together with the discretized energy equation of the heating wire in order to calculate the heat transfer rate. The flow field data necessary for the heat transfer calculation, such as air velocity or temperature, are provided by the CFD solver.

It is important to emphasize the different meaning of the terms "energy equation" and "energy equation of the heating wire". While the energy equation is one of the fluid flow governing equations solved by a CFD solver, the energy equation of the heating wire is the mathematical formulation of the heating wire energy balance and it is used only within the heat transfer model.

4.2 Fluid-wire interaction

Because the heating wire poses a flow obstruction, a successful simulation using the simplified geometry described above has to be able to predict the influence of the wire on the air flow. If experimental measurements summarizing aero dynamical properties of helically coiled heating wires in cross flow are available, the fluid-wire interaction model can be formulated with use of porous media concept. Unfortunately the relevant literature source has not been found. Moreover the experimental study of the convective heat transfer coefficient from helically coiled heating wires in cross flow performed by Comini et al.[3], closely described in chapter 5.1.4, suggests a minor significance of the fluid-wire interactions. A combination of these two facts resulted in the neglect of the fluid-wire interaction. Thus the substitutive geometry does not influence the flow and serves only as a definition of the region where the volumetric heat source terms are distributed.

5 Heat transfer model

The crucial part of the solution method was the formulation and implementation of the heat transfer model. As outlined in the previous chapter, the goal of the model is to predict the heat transfer from the complicated heating coil geometry.

5.1 Development of elemental relationships

A successful model of an engineering problem should be based on a solid knowledge of elemental principles present in the considered case. The following part of the thesis gathers all the necessary theoretical background and develops relationships to be used in the formulation of the model.

5.1.1 Heat generation rate

Resistance heating, also known as Joule heating, resistive heating or ohmic heating, is a process where electric energy is transformed into heat energy. When electric current passes through a conductor, energy dissipation takes place as a result of collisions of charge carriers and elemental particles of the conductor. From a macroscopic point of view, the increase in the kinetic energy of the elemental particles of the conductor is observed as an increase of the conductor temperature.

The quantitative description of the heat generation rate is based on the basic direct current power formula:

$$P = IV \quad \text{Eq. 5.1}$$

where P is the power, I is the current and V is the voltage drop. Because the current is the amount of the charge transported per time unit and the voltage is the amount of energy necessary to move a particle of unit charge across the potential difference V , it is clear that the product of the two is the amount of energy per time unit necessary to maintain the charge flow I across the potential difference V . In the simple circuit consisting of a voltage source and a resistor, the power calculated by eq. 5.1 represents the amount of energy per time unit which the voltage source has to exert in order to keep the voltage drop between its plus and minus contacts equal to V . Because the only way how the energy flow rate supplied by the voltage source can be used is heat dissipation at the resistor, the energy conservation principle requires those energy flow rates to be equal in magnitude. Therefore the power calculated by the formula eq. 5.1 is equal to the heat generation rate of the resistor in a direct current circuit.

The considered heating unit described in chapter 3.2 utilizes the standard electric grid as an energy source. Therefore it is necessary to modify eq. 5.1 to the form suitable for alternating current calculations. It is possible to formulate the instantaneous power given by:

$$P(t) = I(t)V(t) \quad \text{Eq. 5.2}$$

where $P(t)$, $I(t)$ and $V(t)$ are instantaneous power, current and voltage drop respectively. Nevertheless instead of instantaneous quantities it is appropriate to use time averaged quantities, namely root mean square values. If purely resistive load is considered, i.e. a voltage and current are in phase as shown in fig. 10, the average power is given by:

$$P_{AVG} = I_{RMS} V_{RMS} \quad \text{Eq. 5.3}$$

where P_{AVG} is the average power, I_{RMS} is the root mean square value of the current and V_{RMS} is the root mean square value of the voltage drop.

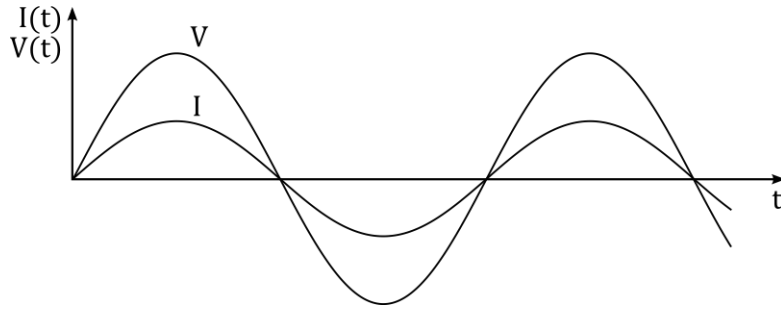


Fig. 10 – Purely resistive load – the current and voltage in phase

It can be proven that the root mean square value of a sine function is:

$$f(y)_{RMS} = \frac{y_{AMP}}{\sqrt{2}} \quad \text{Eq. 5.4}$$

where y_{AMP} is the amplitude of the sine function. With use of eq. 5.4 and Ohm's law, eq. 5.3 becomes:

$$P_{AVG} = I_{RMS}^2 R = \frac{I_{AMP}^2}{2} R \quad \text{Eq. 5.5}$$

where I_{AMP} is the current amplitude and R is the resistance of a resistor.

5.1.2 Heating wire energy equation

When an electric current starts to flow through a heating wire, a transient process involving heat transfer and an increase in the wire temperature begins. The wire temperature grows until an equilibrium state is reached. During the equilibrium state all the heat generated by the electric current is transferred and no heat is accumulated in the wire. A stability of the equilibrium state is enhanced by the usage of materials that show an increase of resistivity with temperature. This can be proven by applying Ohm's law on eq. 5.4 which gains:

$$P_{AVG} = \frac{U_{RMS}^2}{R} \quad \text{Eq. 5.6}$$

An increase in temperature causes an increase of a wire resistance, which results in a decrease of a heat generation rate. This self-regulation property helps to prevent the wire from overheating.

A mathematical description of the heating wire is derived from the energy balance on the wire element shown in fig. 11.

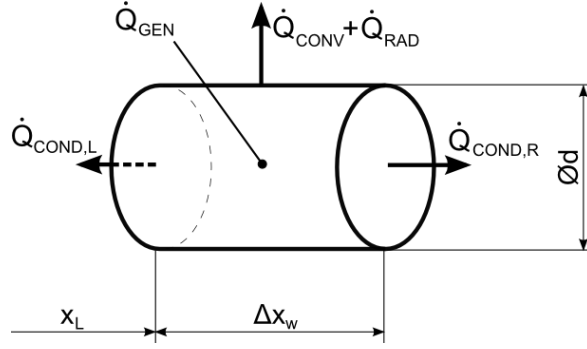


Fig. 11 – Heating wire element with visualization of heat flow rates

Since a steady state formulation is needed, a basic relationship that fulfills the energy conservation principle reads:

$$\dot{Q}_{GEN} = \dot{Q}_{CONV} + \dot{Q}_{RAD} + \dot{Q}_{COND,L} + \dot{Q}_{COND,R} \quad \text{Eq. 5.7}$$

where \dot{Q}_{GEN} is the heat generation rate, \dot{Q}_{CONV} is the convection heat transfer rate, \dot{Q}_{RAD} is the radiation heat transfer rate, $\dot{Q}_{COND,L}$ is the conduction heat transfer rate at the left boundary and $\dot{Q}_{COND,R}$ is the conduction heat transfer rate at the right boundary. The four heat transfer rate terms can be further expressed as

$$\dot{Q}_{CONV} = \alpha(T_W - T_{AMB})A_{CONV} = \alpha(T_W - T_{AMB})\pi d\Delta x_w \quad \text{Eq. 5.8}$$

$$\dot{Q}_{RAD} = \varepsilon\sigma(T_W^4 - T_{RS}^4)A_{RAD} \quad \text{Eq. 5.9}$$

$$\dot{Q}_{COND,L} = k \left. \frac{dT_W}{dx} \right|_{x=x_L} A_{COND} = k \left. \frac{dT_W}{dx} \right|_{x=x_L} \frac{\pi d^2}{4} \quad \text{Eq. 5.10}$$

$$\dot{Q}_{COND,R} = k \left. \frac{dT_W}{dx} \right|_{x=x_L+\Delta x_w} A_{COND} = k \left. \frac{dT_W}{dx} \right|_{x=x_L+\Delta x_w} \frac{\pi d^2}{4} \quad \text{Eq. 5.11}$$

where α is the convective heat transfer coefficient, T_W is the wire temperature, T_{AMB} is the ambient air temperature, A_{CONV} is the convection heat transfer area, d is the wire diameter, Δx_w is the wire element length, ε is the emissivity, σ is the Stefan-Boltzmann constant, T_{RS} is the remote surface temperature, k is the wire material thermal conductivity, A_{RAD} is the radiation heat transfer area, $\left. \frac{dT}{dx} \right|_{x=x_L}$ is the temperature gradient at the left boundary and $\left. \frac{dT}{dx} \right|_{x=x_L+\Delta x_w}$ is the temperature gradient at the right boundary.

Since the resistivity temperature dependence of materials used for heating wires shows a linear character, its mathematical formulation reads:

$$\rho(T_W) = \rho_0 + \beta\rho_0(T_W - T_{R0}) \quad \text{Eq. 5.12}$$

where $\rho(T_W)$ is the resistivity at the temperature T_W , β is the resistivity temperature coefficient, ρ_0 is the reference resistivity and T_{R0} is the temperature at which the reference resistivity is given. With use of the basic equation relating resistivity and resistance

$$\rho = R \frac{A_W}{L_W} \quad \text{Eq. 5.13}$$

where R is the wire resistance, A_W is the wire cross sectional area and L_W is the wire length, eq. 5.12 can be written as:

$$R(T_W) = R_0 + \beta R_0(T_W - T_{R0}) = R_0[1 + \beta(T_W - T_{R0})] \quad \text{Eq. 5.14}$$

where $R(T_W)$ is the resistance at the temperature T_W and R_0 is the reference resistance given at temperature T_{R0} .

Substituting eq. 5.5, eq. 5.8, eq. 5.10, eq. 5.11 and eq. 5.14 into eq. 5.7 and neglecting the radiation heat transfer term yields:

$$\frac{I_{AMP}^2}{2} R_0[1 + \beta(T_W - T_{R0})] = \alpha(T_W - T_{AMB})A_{CONV} + k \frac{dT}{dx}\Big|_{x=x_L} A_{COND} + k \frac{dT}{dx}\Big|_{x=x_L+\Delta x_w} A_{COND} \quad \text{Eq. 5.15}$$

which is the final form of the heating wire energy equation.

5.1.3 Discretization of the heating wire energy equation

A discrete nature of the CFD approach, together with complicated analytical solution of the differential form of the heating wire energy equation, demands a discrete solution to be used. Eq. 5.15 implies the need to approximate only the temperature gradients at the left and right boundaries provided that a constant thermal conductivity k is assumed. Fig. 12 illustrates the discretization problem.

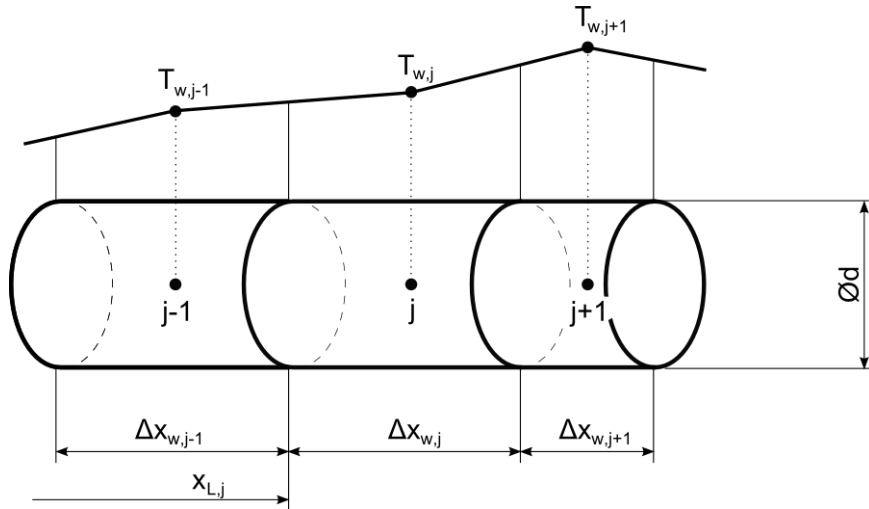


Fig. 12 – Illustration of the heating wire equation discretization

The purely diffusive nature of the conduction terms in eq. 5.15 suggests the first order central differencing approach to be used to approximate the heat conduction fluxes. In other words this means a linear interpolation of the cell temperatures marked T_W in fig. 12. The temperature gradients can therefore be expressed as:

$$\frac{dT}{dx}\Big|_{x=x_{L,j}} = \frac{T_{W,j} - T_{W,j-1}}{\frac{\Delta x_{w,j} + \Delta x_{w,j-1}}{2}} \quad \text{Eq. 5.16}$$

$$\left. \frac{dT}{dx} \right|_{x=x_L+\Delta x_{w,j}} = \frac{T_{W,j+1} - T_{W,j}}{\frac{\Delta x_{w,j+1} + \Delta x_{w,j}}{2}} \quad \text{Eq. 5.17}$$

where $T_{W,j}$, $T_{W,j-1}$ and $T_{W,j+1}$ are the temperatures at cells j , $j-1$ and $j+1$ respectively. To simplify the subsequent rearrangement it is convenient to substitute the denominators in eq. 5.16 and eq. 5.17 as:

$$\left. \frac{dT}{dx} \right|_{x=x_{L,j}} = \frac{T_{W,j} - T_{W,j-1}}{\Delta x_{w,j}^-} \quad \text{Eq. 5.18}$$

$$\left. \frac{dT}{dx} \right|_{x=x_L+\Delta x_{w,j}} = \frac{T_{W,j+1} - T_{W,j}}{\Delta x_{w,j}^+} \quad \text{Eq. 5.19}$$

where

$$\Delta x_{w,j}^- = \frac{\Delta x_{w,j} + \Delta x_{w,j-1}}{2} \quad \text{Eq. 5.20}$$

$$\Delta x_{w,j}^+ = \frac{\Delta x_{w,j+1} + \Delta x_{w,j}}{2} \quad \text{Eq. 5.21}$$

Substituting eq. 5.30 and eq. 5.31 into eq. 5.15 yields:

$$\frac{I_{AMP}^2}{2} R_0 [1 + \beta(T_W - T_{R0})] = \alpha(T_W - T_{AMB}) A_{CONV} + k \frac{T_{W,j} - T_{W,j-1}}{\Delta x_{w,j}^-} A_{COND} + k \frac{T_{W,j+1} - T_{W,j}}{\Delta x_{w,j}^+} A_{COND} \quad \text{Eq. 5.22}$$

After rearranging eq. 5.22 so that terms including the unknown wire temperatures are on the left hand side and the constant terms are on the right hand side, we get:

$$T_{W,j} \left(\frac{I_{AMP}^2}{2} \beta - \frac{k A_{COND}}{\Delta x_{w,j}^+} - \frac{k A_{COND}}{\Delta x_{w,j}^-} - \alpha A_{CONV} \right) + T_{W,j+1} \left(\frac{k A_{COND}}{\Delta x_{w,j}^+} \right) + T_{W,j-1} \left(\frac{k A_{COND}}{\Delta x_{w,j}^-} \right) = \frac{I_{AMP}^2}{2} R_0 (\beta T_{R0} - 1) - \alpha T_{AMB} A_{CONV} \quad \text{Eq. 5.23}$$

A repeating occurrence of $\frac{k A_{COND}}{\Delta x_{w,j}^+}$ and $\frac{k A_{COND}}{\Delta x_{w,j}^-}$ suggests introduction of the constant terms

$$C_j^+ = \frac{k A_{COND}}{\Delta x_{w,j}^+} \quad \text{Eq. 5.24}$$

$$C_j^- = \frac{k A_{COND}}{\Delta x_{w,j}^-} \quad \text{Eq. 5.25}$$

The final form of the discretized heating wire equation therefore reads:

$$T_{W,j} \left(\frac{I_{AMP}^2}{2} \beta - C_j^+ - C_j^- - \alpha A_{CONV} \right) + T_{W,j+1} C_j^+ + T_{W,j-1} C_j^- = \frac{I_{AMP}^2}{2} R_0 (\beta T_{R0} - 1) - \alpha T_{AMB} A_{CONV} \quad \text{Eq. 5.26}$$

An application of eq. 5.26 on a heating wire discretized by n cells results in a system of linear equations which can be written in a matrix form as

$$\mathbf{A}\vec{T}_w = \vec{b} \quad \text{Eq. 5.27}$$

where \mathbf{A} is the coefficient matrix, \vec{T}_w is the vector of the unknown wire temperature and \vec{b} is the vector of the right hand sides. With regard to the form of eq. 5.26, \mathbf{A} is a tridiagonal $n \times n$ matrix while \vec{T}_w and \vec{b} are column vectors containing n elements.

5.1.4 Convection heat transfer coefficient

The model based approach discussed in chapter 4 requires a heat transfer coefficient from helically coiled heating wires in cross flow to be determined. Comini et al.[3] have concluded the experimental study of the method for calculating the required convective heat transfer coefficient, which serves as the basis for the model development in this thesis.

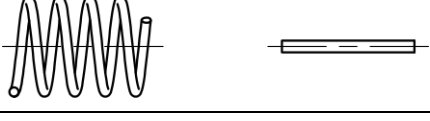
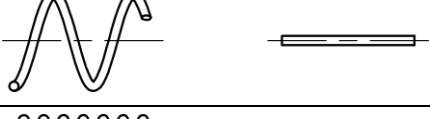
As stated in Comini et al.[3], “*despite the widespread use of open-coil air heaters, forced convection heat transfer from helical coiled resistance wires in cross flow has not been considered in the literature*”. The authors decided to develop a prediction model based on the Churchill and Bernstein correlation, which predicts the forced convection heat transfer coefficient from a cylinder in cross flow and reads:

$$\overline{Nu} = 0.30 + \frac{0.62Re^{1/2}Pr^{1/3}}{[1 + (0.40/Pr)^{2/3}]^{1/4}} \left[1 + \left(\frac{Re}{282000} \right)^{5/8} \right]^{4/5} \quad \text{Eq. 5.28}$$

where \overline{Nu} is the average Nusselt number, Re is the Reynolds number and Pr is the Prandtl number. In order to modify the correlation to be suitable for predicting the convective heat transfer properties of a coiled heating wire instead of a cylinder, the formulations of \overline{Nu} and Re length scales were altered. While the original correlation uses the cylinder diameter as the length scale, the modified correlation introduces an equivalent diameter defined by the relationship:

$$\frac{d_{eq} - d}{D - d} = \exp \left[1 - \left(\frac{S_C}{d} \right)^{1/3} \right] \quad \text{Eq. 5.29}$$

where d_{eq} is the equivalent diameter, d is the wire diameter, D is the helix diameter and S_C is the helix pitch. The comparison of several heating coil configurations and corresponding equivalent diameters is shown in tab. 2.

Geometrical characteristics [mm]	Equivalent diameter [mm]	Visualization
$d = 0.8$ $D = 8$ $S_C = 2.2$	$d_{eq} = 1.3$	
$d = 0.8$ $D = 8$ $S_C = 3.4$	$d_{eq} = 0.8$	
$d = 0.8$ $D = 6.8$ $S_C = 2.4$	$d_{eq} = 1.1$	
$d = 0.7$ $D = 7.6$ $S_C = 2.3$	$d_{eq} = 0.9$	
$d = 0.7$ $D = 7.6$ $S_C = 6$	$d_{eq} = 0.7$	
$d = 0.7$ $D = 10.7$ $S_C = 1.5$	$d_{eq} = 2.5$	

Tab. 2 – Visualization of heating coils and corresponding equivalent diameters

The wind tunnel measurements performed by Comini et al.[3] show an agreement of the measured and predicted Nusselt numbers within 12% and therefore the modified correlation is suitable for the convective heat transfer coefficient prediction. Even though the wake effect is said to be negligible, a caution should be taken when a low helix pitch configuration is used since the amount of inner-spaces is decreased and the interactions between upstream and downstream coils might become significant.

5.1.5 Three phase circuit solution

The heating wire equation (eq. 5.15) derived in chapter 5.1.2 requires the currents in each of the branches to be determined. Thus a mathematical analysis of the three phase circuit described in chapter 3.2 is inevitable.

The key aspect of the considered circuit is the absence of a neutral line. For the sake of clarity it is appropriate to start the discussion with a description of a circuit including a neutral line. Such a connection ensures constant voltages between the phase lines and the neutral line. Each of the branches can be solved separately and currents are determined by a simple application of the Ohm's law. A comparison of the both variants is shown in fig. 13.

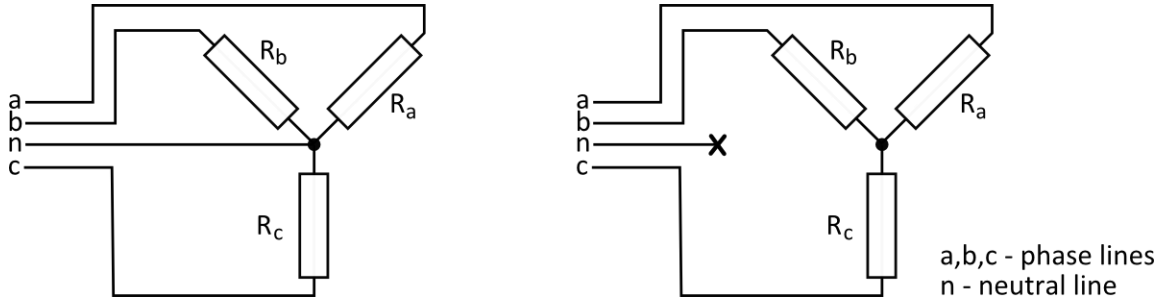


Fig. 13 – Comparison of Wye connection with and without a neutral line

In case of an unbalanced load, i.e. when the resistances of individual branches are not equal, the solution procedure is identical and the only consequence is non-zero current through the neutral line. The consideration of an unbalanced load is appropriate because of the thermal dependence of resistivity. Each of the branches reaches a different steady state wire temperature profile caused by different heat transfer properties across the domain. The resulting resistance is directly dependent on the temperature profile and therefore if it is not possible to guarantee a uniform heat transfer properties across the domain, the unbalanced load is probable to occur.

If the neutral line is not present, the possibility to solve each of the branches separately ceases. The solution, adapted from Alexander [4], can be described with a use of the diagram shown in fig. 14.

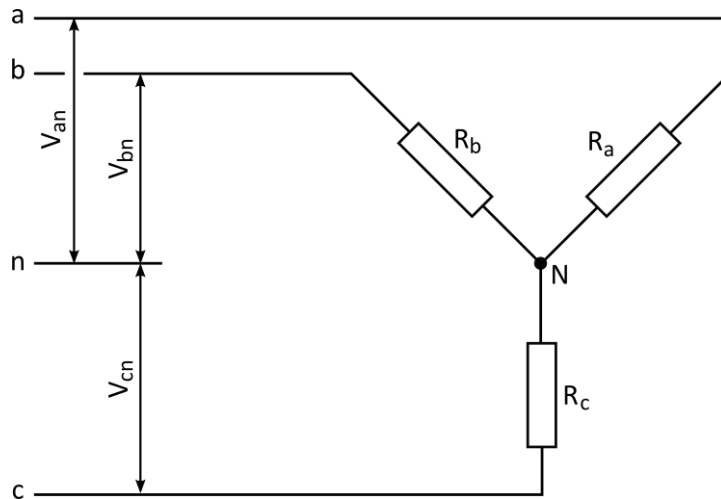


Fig. 14 – Labeled diagram of the considered circuit

Contrary to the balanced load, where the voltage between midpoint N and an arbitrary neutral source is zero, the unbalanced load causes a non-zero midpoint-to-neutral voltage. The voltage can be calculated from the current balance at the midpoint N which reads:

$$\frac{V_N - V_{an}}{R_a} + \frac{V_N - V_{bn}}{R_b} + \frac{V_N - V_{cn}}{R_c} = 0 \quad \text{Eq. 5.30}$$

where V_N is the voltage between the midpoint N and a neutral source, V_{an} , V_{bn} and V_{cn} are the phase-to-neutral voltages and R_a , R_b and R_c are the resistances of the branches. Solving eq. 5.30 for V_N yields:

$$V_N = \frac{R_b R_c U_{an} + R_a R_c U_{bn} + R_a R_b U_{cn}}{R_b R_c + R_a R_c + R_a R_b} \quad \text{Eq. 5.31}$$

The alternating current nature of the problem requires the solution to take into account a phase shift between individual phase-to-neutral voltages. It is common to utilize a complex number representation which can be easily visualized by phasors. The phasor diagram of the standard grid phase-to-line voltages is shown in fig. 15.

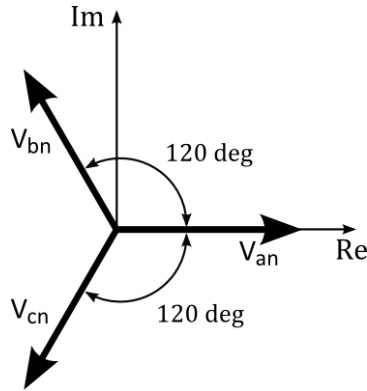


Fig. 15 – Phasor diagram

The complex form of the phase-to-neutral voltages reads:

$$\begin{aligned} V_{an} &= V_{amp} \\ V_{bn} &= -V_{amp} \sin 120^\circ + i V_{amp} \cos 120^\circ \\ V_{cn} &= -V_{amp} \sin 120^\circ - i V_{amp} \cos 120^\circ \end{aligned} \quad \text{Eq. 5.32}$$

where V_{amp} is the amplitude of the phase-to-line voltage. Within this thesis a central European standard $V_{amp} = 230V$ was used.

After substituting eq. 5.32 into eq. 5.31 and solving for V_N , the voltage drops across the resistors can be determined as:

$$\begin{aligned} V_{aN} &= V_{an} - V_N \\ V_{bN} &= V_{bn} - V_N \\ V_{cN} &= V_{cn} - V_N \end{aligned} \quad \text{Eq. 5.33}$$

and subsequently the amplitudes of currents through the branches to be used in eq. 5.15 can be calculated as:

$$\begin{aligned} I_{AMP,a} &= \left| \frac{V_{aN}}{R_a} \right| \\ I_{AMP,b} &= \left| \frac{V_{bN}}{R_b} \right| \\ I_{AMP,c} &= \left| \frac{V_{cN}}{R_c} \right| \end{aligned} \quad \text{Eq. 5.34}$$

where the vertical lines represent a magnitude of a complex number.

5.2 Model description

The main strategy of the modeling approach lies within the discretization of the heating coils and subsequent application of the discretized heating wire energy equation to all of the elements. Thus it is necessary to modify the relationships to account for the helical geometry instead of the straight wire assumed in the original formulation. In order to simplify the calculation, only longitudinal variation of the coiled wire temperature is assumed. This simplification suggest a discretization to be

made also only in the longitudinal direction. It is convenient to relate the discretization of the coiled heating wires with the CFD computational grid as the latter calculation of the volumetric heat source terms can be performed directly without an interpolation. The visualization of the discretization is shown in fig. 16.

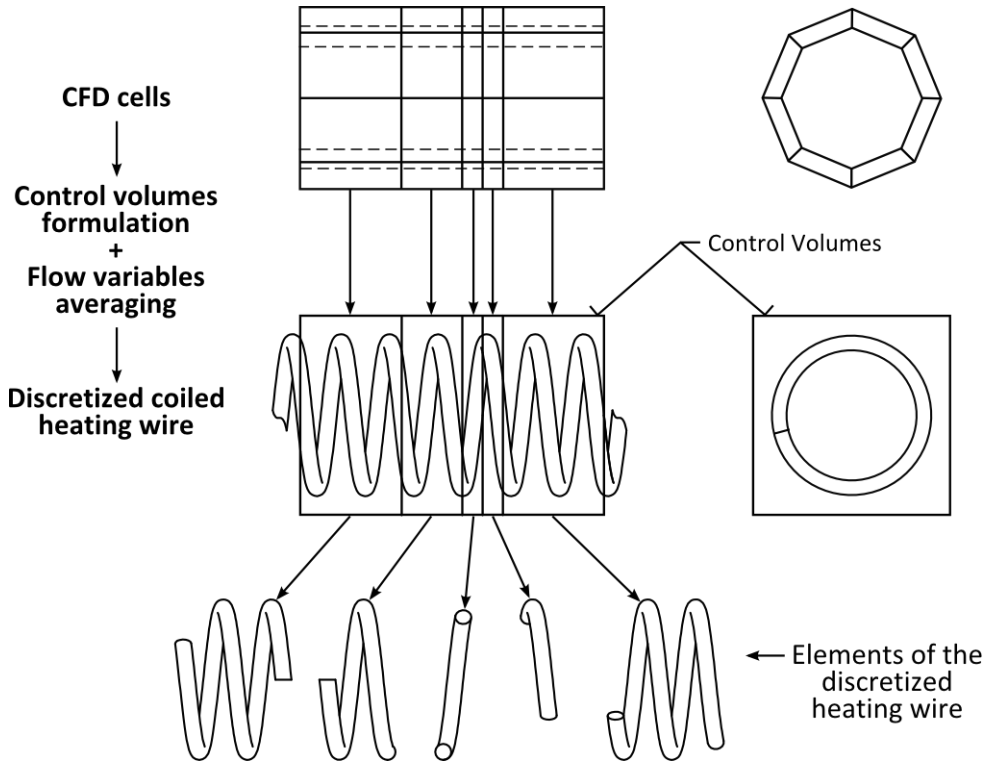
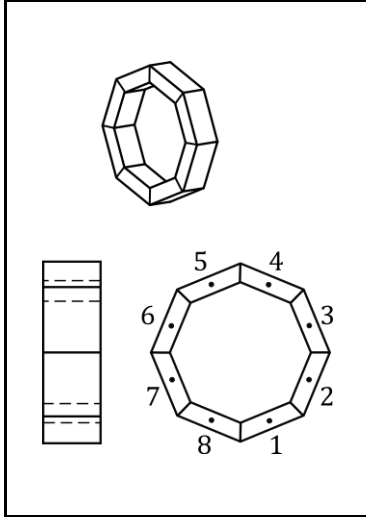
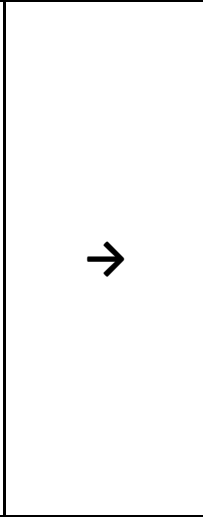
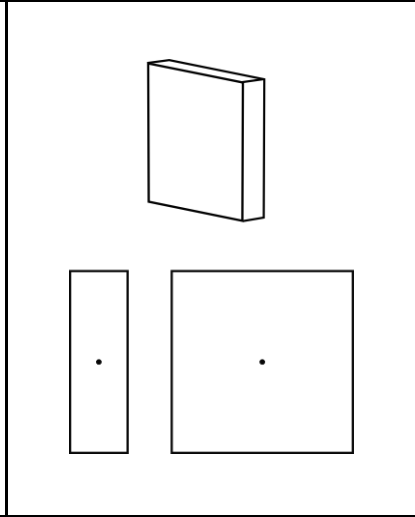


Fig. 16 – Discretization of the heating coil

For the further calculation it is necessary to define the flow variables and wire characteristics at every control volume. Since all the quantities are assumed to be constant across one control volume, the flow variables at 8 cells constituting one control volume have to be merged together. The illustration of the merging procedure together with the specification of mathematical functions used to merge the individual quantities is demonstrated in tab. 3.

			
	8 Cells	Merging	1 Control volume
Temperature	T_C	Averaging	T_{CV}
Velocity	$v_{CX}, v_{CY}, v_{CZ} \Rightarrow v_{C,mag}$	Averaging	v_{CV}
CFD cells Volume	vol_C	Summation	vol_{CV}
Length	L_C	Identical	L_{CV}
X Coordinate	x_C	Identical	x_{CV}
Wire-index	I_W	Identical	$I_{W,CV}$

Tab. 3 – Formulation of the control volume quantities based on CFD cells quantities

While the averaging of the temperature and the identity of the last three quantities are straightforward, it is important to note that the vol_{CV} quantity does not describe the volume of the control volume, but the volume of the CFD cells enclosed within the particular control volume. The $v_{C,mag}$ term in the second row stands for the velocity magnitude calculated from the x, y and z components.

Additional quantities, namely convective heat transfer coefficient, electric resistance and convective heat exchange area, are necessary to determine at each of the control volumes. The convective heat transfer coefficient can be determined based on the correlation described in chapter 5.1.4. The electric resistance is calculated from the known value of the resistance per one meter of the heating coil and therefore it is dependent only on the length of the control volume. The convective heat exchange area is also dependent only on the length of the control volume as the wire diameter and the helix parameters are constant.

Before the linear systems for each of the branches can be defined, it is necessary to determine the branch currents. This can be done by following the procedure described in chapter 5.1.5. Subsequently the linear systems are solved for the unknown wire temperature T_W . This allows a quantification of the heat transferred at each of the control volumes and therefore a calculation of the volumetric heat source terms relevant to the CFD cells enclosed by the particular control volume.

5.3 Model abilities and limitations

The developed model is capable to predict a heat transfer from the helically coiled heating wires and quantify the results in terms of volumetric heat source terms and the temperature profiles of the heating wires. Contrary to the balance approach for which the original correlation was developed, the model formulated within this thesis is able to predict detailed heat transfer characteristics across the flow domain. However a suitability of the model formulation is not granted by any of the assumptions and only experimental measurements showing an agreement of the predicted and

measured values can support the validity of this approach. Since the cross flow condition, assumed in the experimental study of the convective heat transfer coefficient, is violated in the wire supports region, the transferred heat and wire temperatures in this region are expected to be over or under-predicted.

Because of the complicated geometry a radiation heat transfer was neglected. As air in the atmospheric composition and temperatures reached in the dryer does not significantly participate in the radiation heat transfer, the main expected source of error caused by the neglect of the radiation heat transfer lies in the increase in the surface temperature of the metal parts that surround the heating coils and subsequent convective heat transfer from the parts to the air.

Since the experimental data used to formulate the model does not include the influence of the free stream turbulence levels, also the model is unable to predict the relationship between the turbulence properties and the heat transfer.

5.4 Implementation

The need to employ a custom code demanded a programming platform to be chosen. Ansys Fluent offers a possibility to implement custom code calculations as user defined functions (UDF). By using a C programming language and predefined macros, one can easily access the flow variables, perform additional calculations and integrate the calculation results into the solution process. Even though the Fluent's UDF interface offers all the necessary tools, it has been decided to use it only for data export/import and to perform the main body of the model related calculations in Matlab. The reason for this is the user friendly environment allowing an effective debugging together with a great number of predefined functions allowing a fast solution of elementary vector and matrix operations. A negative consequence of the Matlab approach is an increase in the computational time caused by the need to export the data from Fluent, process it and import it back. However, during a development stage, this approach appears to be perfectly suitable. The final deployment of the model should nevertheless utilize some of the lower level programming languages to guarantee a maximum computational efficiency. A flowchart of the model implementation is shown in fig. 17. The following chapters discuss the individual steps in detail.

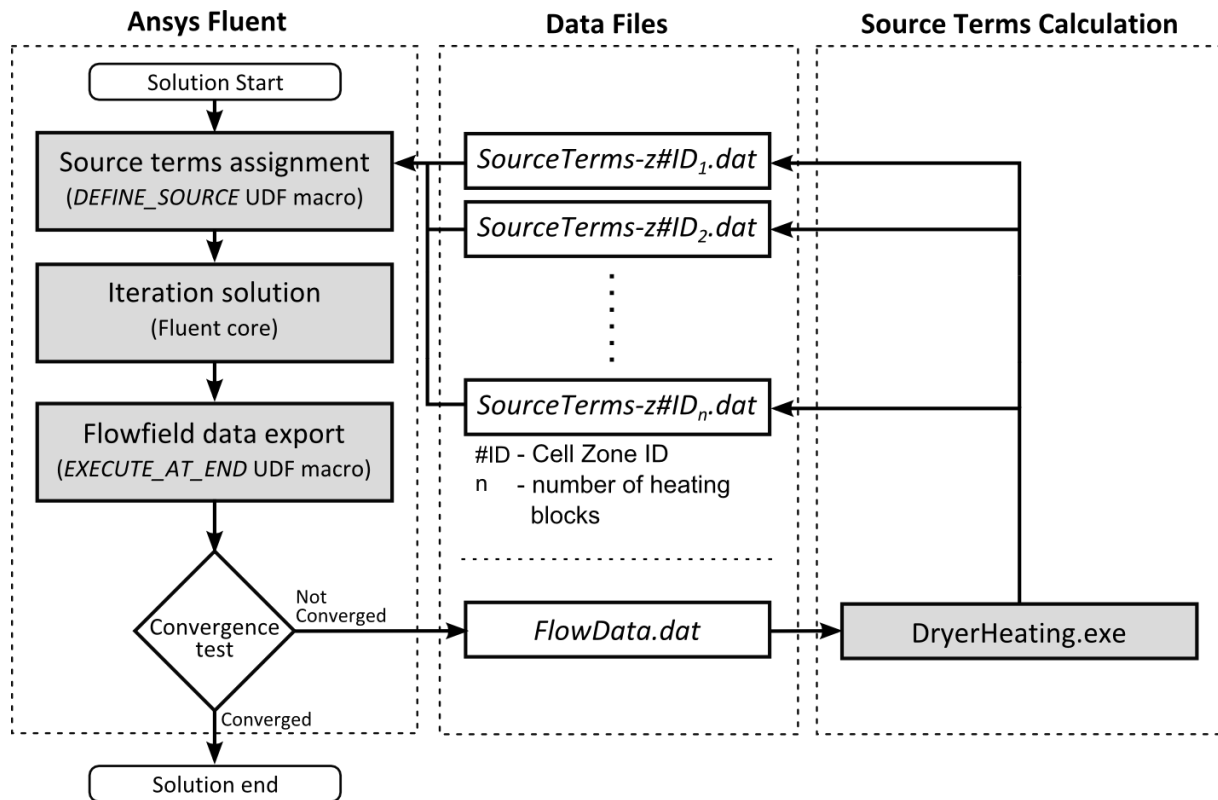


Fig. 17 – Model flowchart

5.4.1 Flow field data export

Since the heat transfer from the heating wires is dependent on the flow variables, the first step of the procedure is to obtain the relevant flow field data and export it in a suitable form. The data export has to be performed every iteration. Thus it is suitable to utilize the *execute_at_end* UDF macro which executes the nested code at the end of each iteration.

The gathered data are exported into space-separated ASCII file *FlowData.dat*. The structure of the file is described in tab. 4. It is important to note that only the data corresponding to the heating cell zones are exported (see chapter 6.2 for the definition of the term 'heating cell zone').

Column number	1	2	3	4	5	6	7	8	9	10	11
Property	Cell ID	X - Velocity	Y - Velocity	Z - Velocity	Temperature	X - Centroid position	Y - Centroid position	Z - Centroid position	Cell Volume	Cell Z length	Cell Zone ID
Notation	-	v_{CX}	v_{CY}	v_{CZ}	T_C	x_C	y_C	z_C	vol_C	L_C	-

Tab. 4 – Structure of the flow variables data file

After all the data are written and the file is closed, the standalone *DryerHeating.exe* application is executed by the *system* command from within the *execute_at_end* macro. The need to execute an external application was a key argument for using a compiled UDF type instead of an interpreted one. Even though the compiled UDF type requires an external C compiler to be installed, the great

benefit, besides being faster, is the possibility to include standard C libraries and consequently use functions such as *system*. The source code of the UDF is attached as appendix A.

5.4.2 Calculation of the volumetric heat source terms

As outlined in the fig. 17, the calculation of the volumetric heat source terms is performed by the external standalone executable application which was compiled from the Matlab source file. The description of the calculation follows. A reader is encouraged to refer to appendix B for the full Matlab code. An overview of the calculation process is sketched in fig. 18

Because the calculation is to be performed separately for each of the heating blocks, it is appropriate to employ a for-loop over the number of the blocks and repeat the same algorithm for each of the blocks. The data relevant to the currently solved heating block are identified based on the *cell zone ID* column in the *FlowData.dat* file.

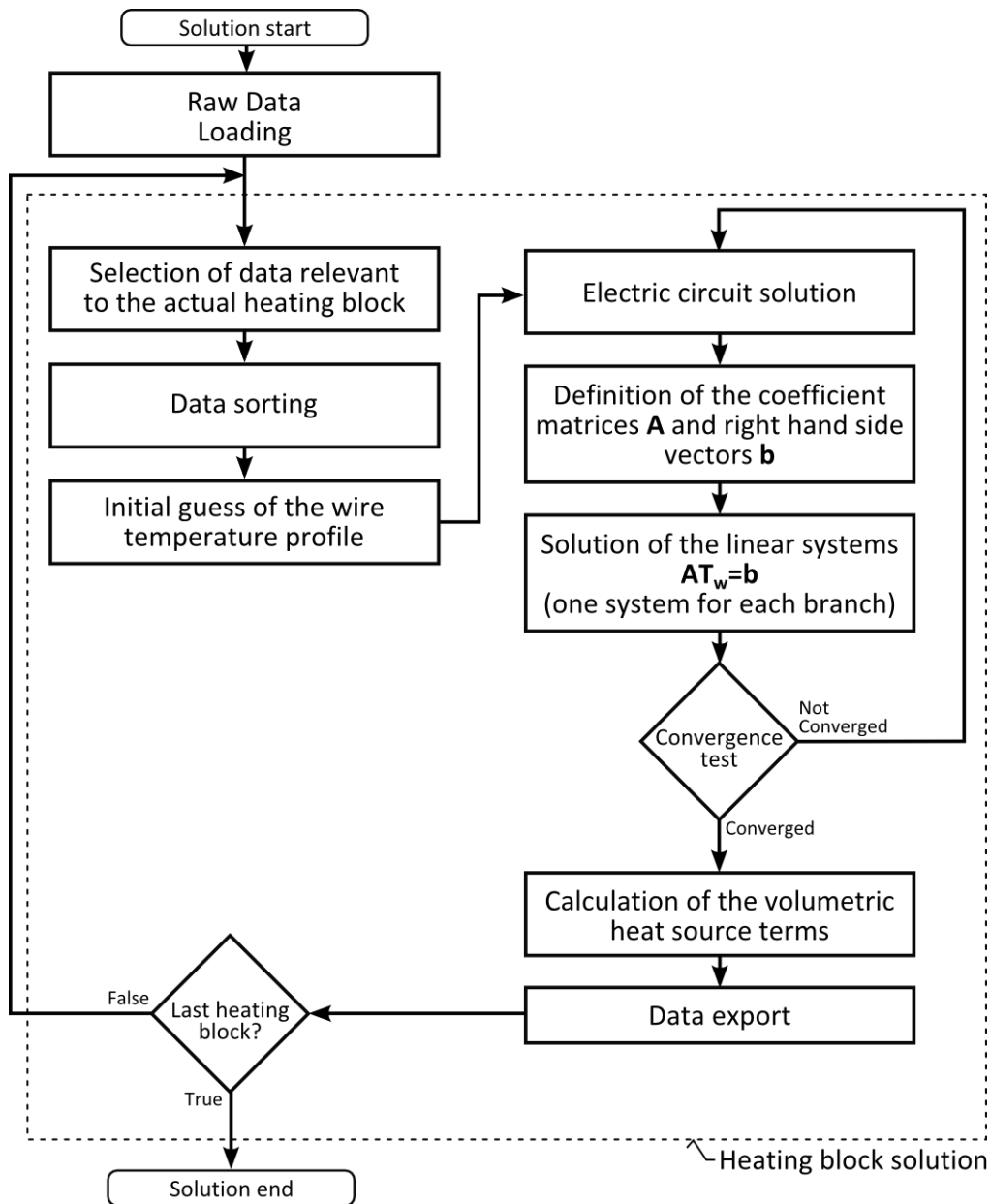


Fig. 18 – Matlab code flowchart

In the next step an extensive data manipulation is inevitable in order to process the data into a form suitable for a solution of the linear systems resulting from the application of the discretized heat wire equation to each of the branches. The linear systems cannot be explicitly solved for T_w because the current term I_{AMP} which is present on both the left and the right hand side of eq. 5.26. The magnitude of I_{AMP} is dependent on the resistances of each of the branches within the block and since these resistances are functions of T_w , a necessity to utilize an iterative approach arises.

To start the iterative solution, the wire temperature profiles have to be guessed. Subsequently the resistances can be calculated and used to determine the currents through the individual branches. At this stage, the coefficient matrices and the vectors of the right hand sides can be defined, allowing a solution of the linear systems. At each iteration the currents are adjusted with regard to the actual wire temperatures. After the solution has converged, the volumetric heat source terms can be determined and exported.

It can be noted here that the Matlab code was formulated in a way that allows a future usage of the model to take into account a variable heating coil geometry in each of the heating blocks. This aspect is necessary when the heating unit configuration including both the 4.5KW and 6KW heating blocks is considered. The variable heating geometry implementation is based on the fact that the coil and wire parameters are stored as vectors. The code utilizes a *dist.dat* data file to specify the vector index to be used for the particular heating block represented by the heating cell zone ID.

5.4.2.1 Data sorting

The main goal of the data sorting is to allow a simple data access during the assembly of the coefficient matrices and right hand side vectors. Every cell is assigned a set of indices that uniquely relate the particular cell to the logical groups such as a heating wire or a branch. The visualization of the indexing system is sketched in fig. 19. The Y-index and Z-index fully specify the wire position within the block. The branch-index and wire-index are used in the code as loop indices and also as the basis for the determination of the wires connectivity.

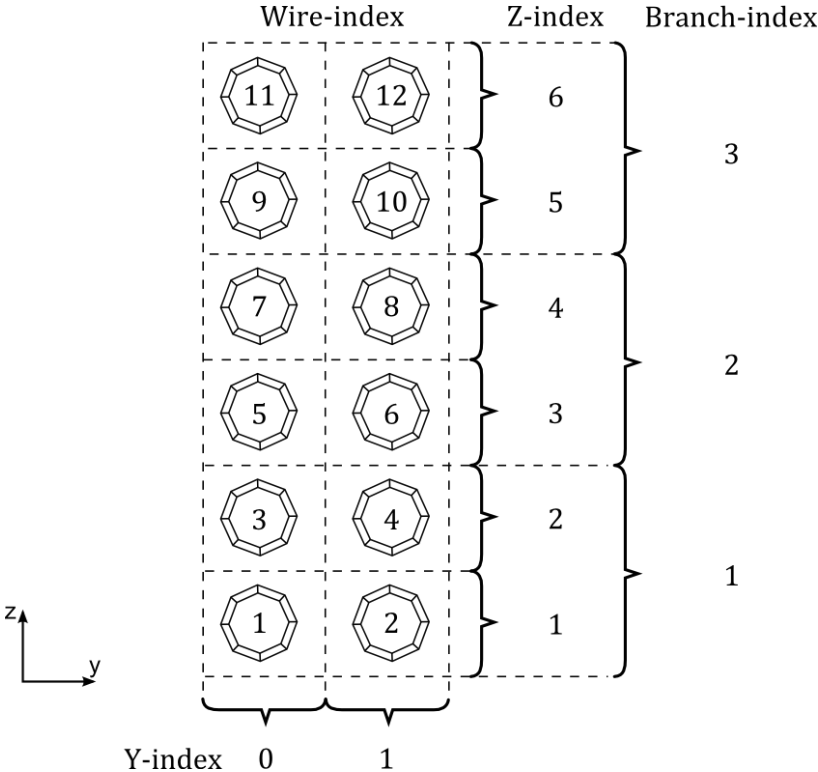


Fig. 19 – Indexing system description

The Y-index can be defined as:

$$I_Y = \begin{cases} 1 & \text{for } y_C > y_{BC} \\ 0 & \text{for } y_C < y_{BC} \end{cases} \quad \text{Eq. 5.35}$$

where I_Y is the Y-index, y_C is the y coordinate of the cell centroid and y_{BC} is the y coordinate of the heating block center point, defined as:

$$y_{BC} = \frac{\max(y_C) + \min(y_C)}{2} \quad \text{Eq. 5.36}$$

The formula used to determinate the Z-index reads:

$$I_Z = \text{ceil} \left(\frac{z_C^{\vec{Z}COORD}}{n_{ZU}/n_{ZW}} \right) \quad \text{Eq. 5.37}$$

where I_Z is the Z-index, $z_C^{\vec{Z}COORD}$ is the position of the cell centroid z coordinate in the vector of unique z cell coordinates $\vec{Z}COORD$, n_{ZU} is the number of elements in $\vec{Z}COORD$ vector, n_{ZW} is the number of heating wires per block in z-direction and $\text{ceil}()$ is the function that rounds the argument to the closest higher integer. The sketch illustrating the elements of the $\vec{Z}COORD$ vector is shown in fig. 20.

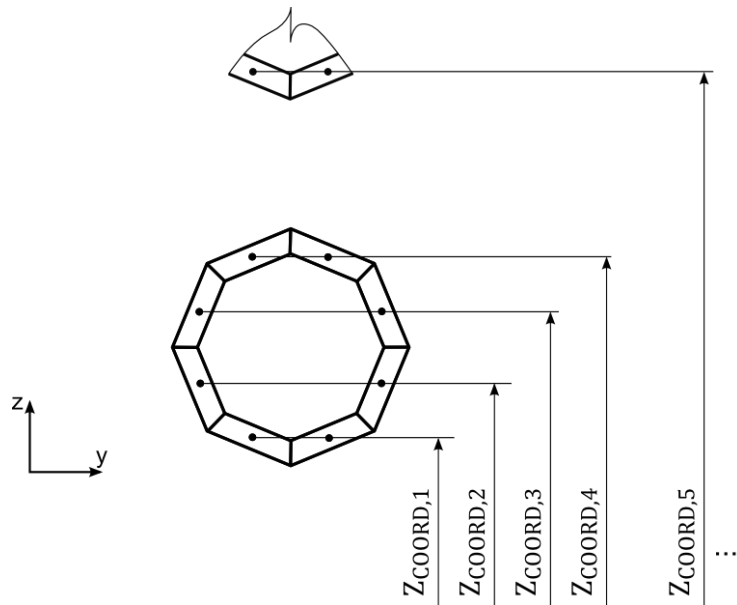


Fig. 20 – Illustration of unique z cell coordinates

The wire-index and the branch-index are given by relationships:

$$I_W = 2 I_Z - I_Y \quad \text{Eq. 5.38}$$

$$I_B = \text{ceil} \left(\frac{I_Z}{n_{ZB}} \right) \quad \text{Eq. 5.39}$$

where I_W is the wire-index, I_B is the branch index and n_{ZB} is the number of heating wires in z direction in one branch.

To allow a solution to take into account the connectivity of the wires, which is sketched in fig. 21a, the wire-branch-index is introduced. As can be seen in fig. 21b, the indexing describes the order in which the set of four wires is connected to form one branch.

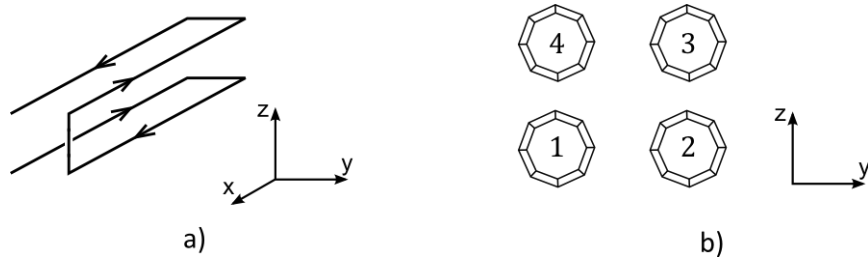


Fig. 21 – a) Wires connectivity within a branch b) Wire-branch-index visualization

To determine the wire-branch-index in terms of indices defined earlier in this chapter, the following relationship is used:

$$I_{WB} = I_W - 4(I_B - 1) - [I_Z - (2I_B - 1)](-1)^{I_Y} \quad \text{Eq. 5.40}$$

5.4.2.2 Data storage

In order to store the data for all the control volumes within the heating block, an appropriate Matlab data structure ensuring a simple data access during the subsequent assembly of the linear system coefficients has to be chosen. With regard to the connectivity of the heating wires within the branch, it is beneficial to introduce a $n_{CVB} \times n_B$ data storage matrix for each of the control volume quantities ($n_{CVB} = n_{WB}n_X$ is the number of control volumes in one branch, n_{WB} is the number of wires in one branch, n_X is the number of control volumes in the x-direction and n_B is the number of branches in one heating block). Besides the abovementioned control volume quantities also the wire temperature is stored in $n_{CVB} \times n_B$ matrix. The vectors of unknown wire temperatures are constructed based on this matrix before the linear system is solved.

It is convenient to assemble the data storage matrix in two steps. In the first step, a temporary set of vectors is created for each of the heating wires in order to store the merged and calculated values at all the control volumes. In the second step, the temporary vectors are combined to form the data storage matrix. The combination has to account for the connectivity of the branches. The visualization of the data storage matrix assembly process is illustrated in fig. 22.

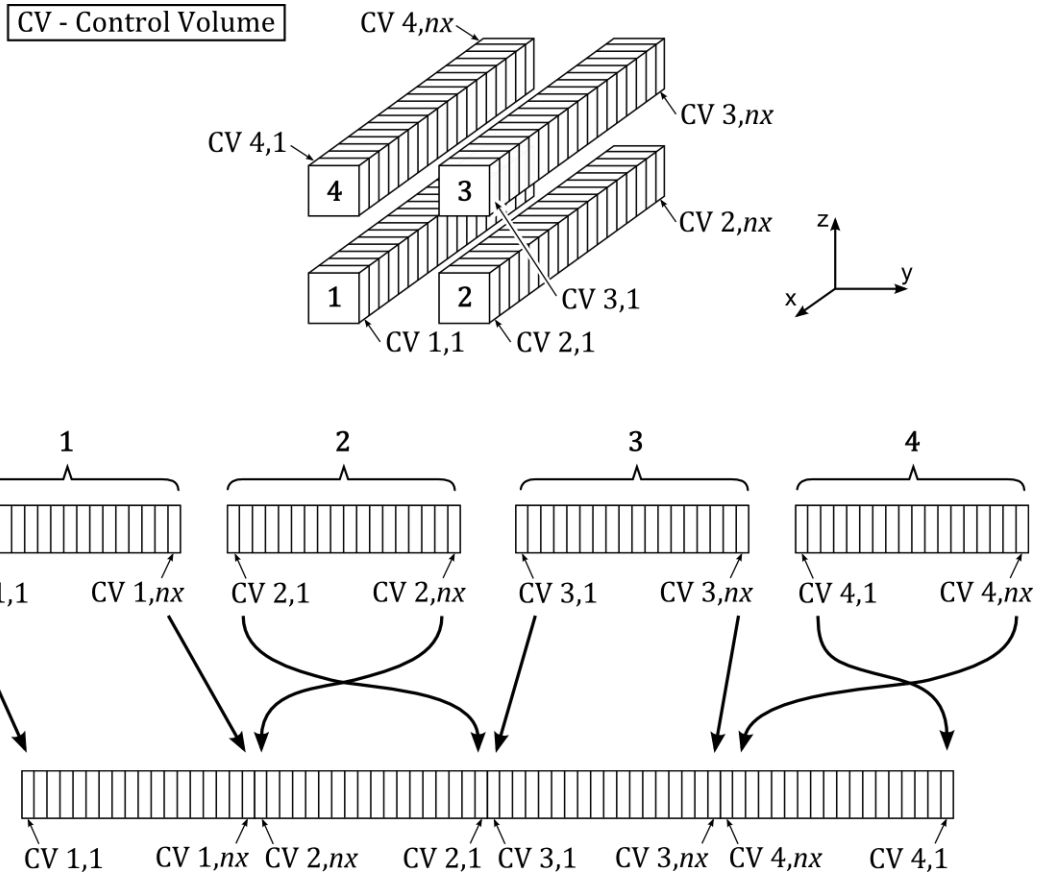


Fig. 22 – Data storage matrix assembly

At the top of fig. 22 the control volumes representing one branch of the heating block are shown. The indices of the control volumes are identical to the indices of the temporary vectors. To describe the wire connectivity (sketched in fig. 21a) it is necessary to assemble the matrix so that the control volume $CV 1,nj$ neighbors with $CV 2,1$, $CV 2,nj$ neighbors with $CV 3,1$, etc. as depicted at the bottom part of fig. 22. To achieve this, the algorithm mirrors the temporary vectors with even branch-wire-indices. Each of the columns of the resulting data matrix stores the data relevant to one particular branch, which is convenient as the latter linear system calculation is solved for each of the branches separately.

5.4.2.3 Calculation of control volume quantities

Besides the flow variables and CFD cells characteristics listed in tab. 3, additional quantities present in eq. 5.26 have to be defined at each of the control volumes. These quantities are the convective heat transfer coefficient α_{CV} , the convection heat exchange area $A_{CONV,CV}$ and the cold electrical resistance of the part of the wire enclosed by the particular control volume $R_{0,CV}$.

The convective heat transfer coefficient α_{CV} can be calculated as:

$$\alpha_{CV} = \frac{\overline{Nu} \lambda_{air}}{d_{eq}} \quad \text{Eq. 5.41}$$

where λ_{air} is the thermal conductivity of air. The definitions of \overline{Nu} and d_{eq} can be found in chapter 5.1.4. Since \overline{Nu} is the function of the Reynolds number and therefore of the air velocity, the convective heat transfer coefficient varies across the control volumes based on the averaged velocity v_{CV} .

The relationship used to determine the convection heat transfer area $A_{CONV,CV}$ reads:

$$A_{CONV,CV} = (\pi D)(\pi d) \frac{L_{CV}}{S_C} = \frac{\pi^2 D d L_{CV}}{S_C} \quad \text{Eq. 5.42}$$

The control volume resistance $R_{0,CV}$ is given as:

$$R_{0,CV} = R_{1m} L_{CV} \quad \text{Eq. 5.43}$$

Where R_{1m} is the resistance of one meter of the heating coil, which was calculated from the experimentally measured cold branch resistance R_{br} as:

$$R_{1m} = \frac{R_{br}}{4L_{COIL}} \quad \text{Eq. 5.44}$$

where L_{COIL} is the length of the heating coil. It is important not to confuse the term 'length of the heating coil' with the length of the wire used as a semi-product to form the coiled wire geometry.

5.4.3 Linear systems definition

With all the necessary data sorted and the coiled wire geometry discretized, it is possible to apply the discretized heating wire energy equation to the coiled heating wire, which for the j th control volume in the k th branch reads:

$$\begin{aligned} T_{W,CV,j,k} \left(\frac{I_{BR,k}^2}{2} \beta - C_{j,k}^+ - C_{j,k}^- - \alpha_{CV,j,k} A_{CONV,CV,j,k} \right) + T_{W,j+1,k} C_{j,k}^+ + T_{W,j-1,k} C_{j,k}^- \\ = \frac{I_{BR,k}^2}{2} R_{0,CV,j,k} (\beta T_{R0} - 1) - \alpha_{CV,j,k} T_{CV,j,k} A_{CONV,CV,j,k} \end{aligned} \quad \text{Eq. 5.45}$$

where $T_{W,CV}$ is the $n_{CVB} \times n_B$ matrix of the unknown wire temperature, C^+ and C^- are the $n_{CVB} \times n_B$ matrices of the constant terms and \vec{I}_{BR} is the vector of the currents through the branches. In order to determine the wire temperature at all the control volumes, one linear system for each of the branches has to be solved. The matrix notation of the linear systems can be written as:

$$\mathbf{A}_k \vec{T}_{wk} = \vec{b}_k \quad k = 1..n_B \quad \text{Eq. 5.46}$$

where \mathbf{A}_k is the coefficient matrix of the k th branch, \vec{T}_{wk} is the vector of the unknown wire temperature for the k th branch and \vec{b}_k is the right hand sides vector for the k th branch. The coefficient matrix \mathbf{A}_k can be defined as:

$$(\mathbf{A}_k)_{m,n} = \begin{cases} \frac{I_{BR,k}^2}{2} \beta - C_{m,k}^+ - C_{m,k}^- - \alpha_{CV,m,k} A_{CONV,CV,m,k} & \text{for } m = n \\ C_{m,k}^+ & \text{for } m = n - 1 \\ C_{m,k}^- & \text{for } m = n + 1 \end{cases} \quad \text{Eq. 5.47}$$

which results in a tridiagonal $n_{CVB} \times n_{CVB}$ matrix. The vector of the unknown wire temperature T_{wk} can be extracted from the $T_{W,CV}$ matrix as:

$$(T_{wk})_m = (T_{W,CV})_{m,k} \quad m = 1, 2, \dots, n_{CVB} \quad \text{Eq. 5.48}$$

The right hand side vector b_k is given by

$$(b_k)_m = \frac{I_{BR,k}^2}{2} R_{0,CV,m,k} (\beta T_{R0} - 1) - \alpha_{CV,m,k} T_{CV,m,k} A_{CONV,CV,m,k} \quad m = 1, 2, \dots, n_{CVB} \quad Eq. 5.49$$

Because both the coefficient matrix and the right hand side vector contain the \vec{I}_{BR} vector which is dependent on the wire temperature, the solution of the wire temperature field cannot be calculated explicitly. An iteration approach is therefore utilized and described below.

5.4.3.1 Iterative solution of the wire temperature field

The first inevitable step for an arbitrary iteration process is the initial guess. In the present case the temperature field has to be guessed in order to allow the branch resistances and subsequently the branch currents to be determined. A constant temperature guess of 250°C is used in the Matlab code.

In the beginning of every iteration, the branch resistances are determined as:

$$(R_{BR})_k = \sum_{i=1}^{n_{CVB}} R_{0,CV,i,k} [1 + \beta (T_{W,CV,i,k} - T_{R0})] \quad k = 1..n_B \quad Eq. 5.50$$

where $(R_{BR})_k$ is the k th element of the vector of branch resistances \vec{R}_{BR} . With known branch resistances the currents can be determined based on the three phase circuit solution procedure described in chapter 5.1.5.

Now the coefficient matrix and the right hand side vector can be assembled. The assumption of adiabatic boundary conditions implies:

$$\begin{aligned} C_{j=n_{WB},k}^+ &= 0 \\ C_{j=1,k}^+ &= 0 \end{aligned} \quad k = 1..n_B \quad Eq. 5.51$$

The complete linear systems were solved by *linsolve* matlab function. However if the model is to be implemented in some of the lower level programming languages, the solution can be obtained by an implementation of numerical algorithms such as LU decomposition, Gauss-Seidel method, etc.

At the end of every iteration the two norm value of the $T_{W,CV}^i - T_{W,CV}^{i-1}$ matrix is calculated and used as the convergence criterion (the superscript i stands for the current iteration and $i - 1$ stands for the previous iteration). The iteration procedure is repeated until the convergence criterion value is larger than the required accuracy ε . For the calculations performed within this thesis, the value $\varepsilon = 10^{-6}$ was used.

5.4.3.2 Calculation and export of the volumetric heat source terms

With known values of the wire temperature at each of the control volumes, the calculation of the volumetric heat source terms is straightforward. The amount of transferred heat at each of the control volumes is given by:

$$(\dot{Q}_{CV})_{m,n} = \alpha_{CV,m,n} (T_{W,CV,m,n} - T_{CV,m,n}) A_{CONV,CV,m,n} \quad Eq. 5.52$$

where \dot{Q}_{CV} is the matrix of the transferred heat. To obtain the value of the volumetric heat source, the transferred heat has to be divided by the reference volume, which for this case is the volume of

the eight CFD cells enclosed by each of the control volumes (stored in the vol_{CV} matrix). Therefore the volumetric heat source is given by:

$$(S\dot{Q}_{CV})_{m,n} = \frac{(\dot{Q}_{CV})_{m,n}}{(vol_{CV})_{m,n}} \quad \text{Eq. 5.53}$$

where $S\dot{Q}_{CV}$ is the $n_{CVB} \times n_B$ matrix of the volumetric heat sources.

As the last step, the data has to be exported in a format suitable for the subsequent use in fluent. It is necessary to specify the volumetric heat source value at each of the CFD cells represented by the cell ID, which requires an identification of cell ID values related to each of the control volumes. The related cell ID values can be identified in the raw data matrix based on the x-position value x_{CV} and the wire-index $I_{W,CV}$. The obtained Cell ID values are linked together with the corresponding volumetric heat source values and wire temperatures and exported into data files. A separate data file with structure given by tab. 5 is used for each of the heating blocks as indicated in the flowchart in fig. 17.

Column	1	2	3
Property	Cell ID	Volumetric Heat Source Term value	Wire temperature

Tab. 5 – Data structure of the volumetric heat source terms data file

6 Present Case CFD Analysis

Within this chapter all the steps and considerations performed in order to obtain the flow field solution are discussed. The simplifications and relationships introduced in chapters 4 and 5 are utilized and applied to the CFD solver environment. To realize the CFD simulation, a software combination of Gambit 2.4.6, Ansys Fluent 14.0 and Matlab R2010b has been used.

6.1 Computational Domain and Boundary Conditions

The first step of a general CFD problem is the formulation of a computational domain with regard to the goals of a simulation. The confined flow nature of the considered case implies the dryer walls to form the domain boundaries. In order to fully define the domain, upstream and downstream boundaries have to be specified. This selection is usually a trade-off between accuracy and computing power requirements, because a larger domain, ensuring a higher accuracy, obviously demands a higher number of discretization cells and therefore higher computing power requirements.

The upstream boundary is crucial for the development of the velocity profile within the domain. Since the velocity magnitude is one of the key parameters of the convective heat transfer coefficient from the helically coiled heating wires, it has been decided to include the inlet channel in the domain to allow the velocity profile at the top chamber inlet to develop. The visualization of the inlet channel geometry is shown in fig. 23. The detailed geometry of the drivetrain was replaced by a substitutive model consisting of orthogonal objects only since such a configuration is easy to discretize with hexahedral elements.

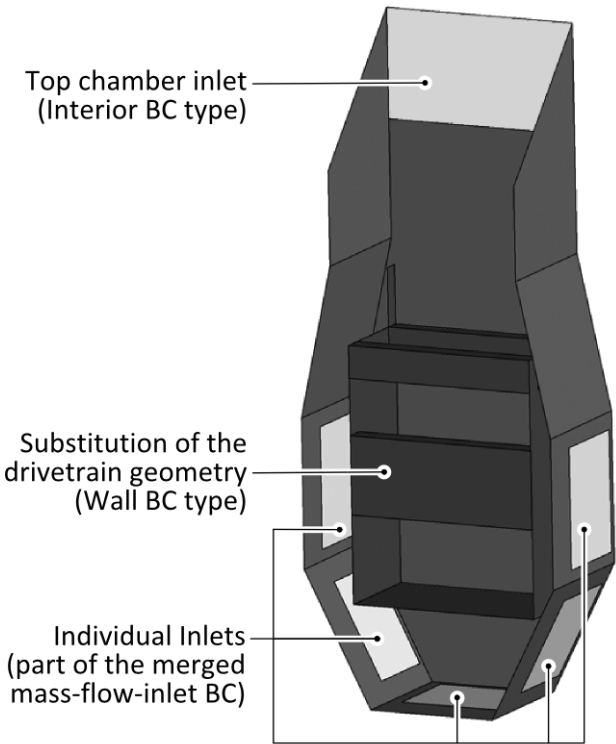


Fig. 23 – Inlet channel geometry

As described in chapter 3.1, air can enter the dryer either through the set of perforations at the bottom of the inlet channel or through the combustion air intake located on the left side of the top

chamber. Since the only known value is the total air flow rate measured at the outlet, an accurate solution of this multiple inlet configuration demands a computational domain enclosing all the inlets. Such a domain configuration ensures a flow field solution allowing for a non-uniform distribution of the mass flow across the individual inlet parts. The assessment of the inlet uniformity significance together with an estimation of additional cells requirement resulted in the domain definition shown in the fig. 24. By merging all the inlet parts into one mass-flow-inlet boundary condition, the given mass flow rate is uniformly divided across the total inlet surface.

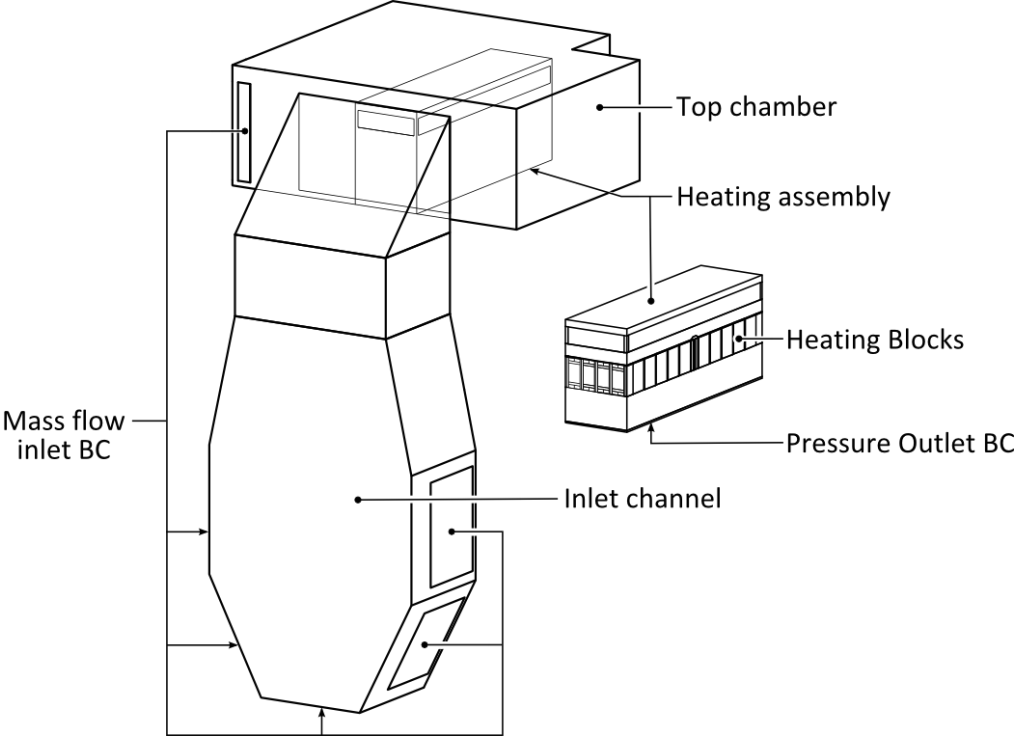


Fig. 24 – Computational domain visualization

The selection of the downstream domain boundary is visible in fig. 24. Proximity of the rotating perforated drum demands a discussion of the selection impact. The qualitative analysis of the rotating drum influence is visualized in fig. 25. It is highly probable that the flow leaving the heating unit will be pulled to the side of the channel under the influence of the rotating drum, which can result in a formation of eddies. The eddies are likely to reduce the mass flow through the heating blocks located on the leeward (right in the fig. 25) side of the heating unit. In the worst case scenario, a reversed flow through the heating blocks may occur.

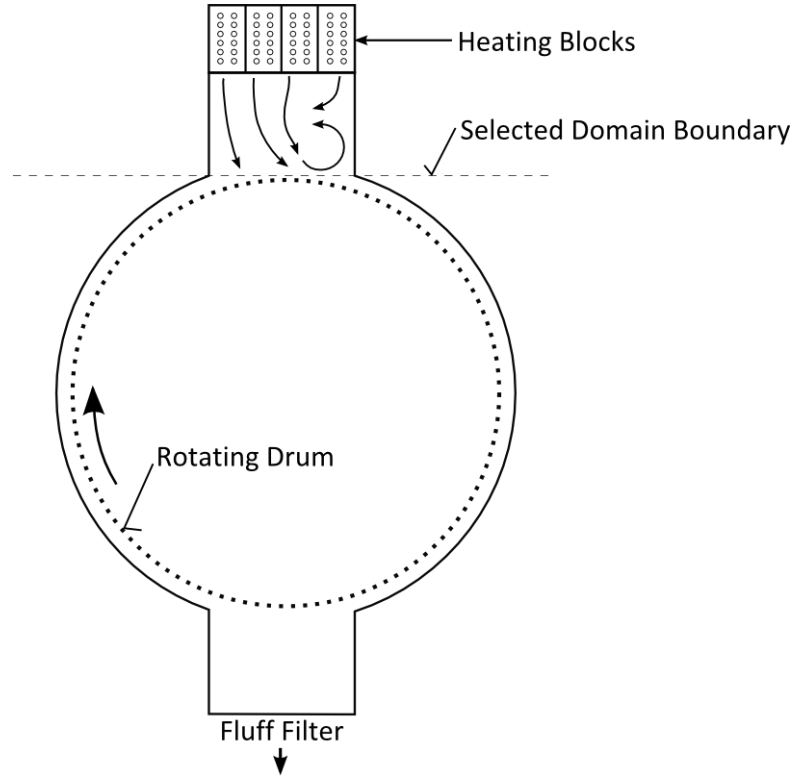


Fig. 25 – The influence of the rotating drum on the heating channel flow

A basic quantitative analysis of the rotating drum influence can be based on the comparison of the drum and air velocities. The drum velocity can be calculated as:

$$v_{DRUM} = 2\pi n_{DRUM} r_{DRUM} = 2\pi \cdot 40 \text{min}^{-1} \cdot 0.465 \text{m} = 1.95 \text{ [m} \cdot \text{s}^{-1}]$$

where v_{DRUM} is the drum velocity, n_{DRUM} is the rotational speed of the drum in rpm and r_{DRUM} is the radius of the drum. The velocity of the air at the heating unit outlet is given by

$$v_{AIR} = \frac{\dot{V}_{AIR}}{A_{CH}} = \frac{950 \text{ [m}^3 \cdot \text{h}^{-1}]}{0.15 \text{ [m}^2]} = 1.76 \text{ [m} \cdot \text{s}^{-1}]$$

where v_{AIR} is the air velocity, \dot{V}_{AIR} is the air volumetric flow rate and A_{CH} is the cross-sectional area of the channel. The comparison of the calculated velocities reveals a slight dominance of the drum velocity. Thus the pulling effect described above cannot be neglected. However a simple solution taking into account the pulling effect while keeping the original domain boundary has not been found. Therefore the only possible solution is to move the outlet boundary further downstream and to include the drum geometry in the computational domain. If no simplifications are introduced, a number of additional cells can be estimated as

$$n_{DC} = n_{PER}n_{C,PER} + n_{IN} + n_{OUT}$$

Where n_{DC} is the number of cells required for the discretization of the drum region, n_{PER} is the number of perforations, $n_{C,PER}$ is the number of cells required to discretize one perforation, n_{IN} is the number of cells required to discretize the internal region of the drum and n_{OUT} is number of cells required to discretize the outer drum region. Using estimated values $n_{PER} = 2500$ (shorter drum version used in T24 model), $n_{C,PER} = 100$, $n_{IN} = 75\,000$, $n_{OUT} = 30\,000$, the number of required cells is

$$n_{DC} = 2\,605\,000$$

which is unacceptable due to immense computing power requirements. Moreover a brief literature research has not discovered any source applicable to the drum geometry in order to formulate a simplified model of the drum flow. As a result, it is inevitable to use the original definition of the computational domain and do not include the drum in the simulation.

The downstream boundary type was selected to be a pressure outlet. The value of the gauge pressure was set to zero. Since the main pressure drop is expected to take a place in the drum region, this assumption is considered to be valid within the required accuracy.

6.2 Computational grid

A grid generation procedure has to take into account several requirements. Beside a choice of discretization elements type, a grid size has to be appropriate to the required accuracy, available computing power and physical processes to be resolved. Too coarse grid can degrade the solution accuracy while too fine grid can exceed the computing hardware limits.

The assessment of the level of detail of the computational domain suggests the required average grid cell size to vary across the domain as sketched in fig. 26.

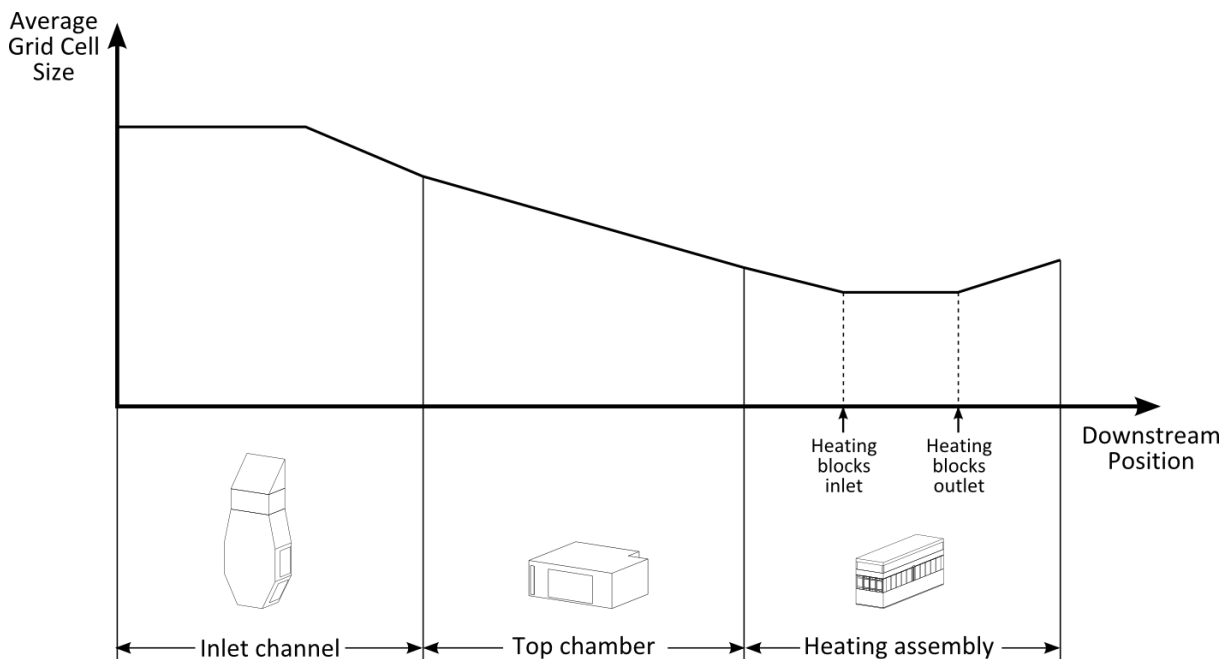


Fig. 26 – Qualitative description of the required average grid cell size

To ensure a smooth coarsening of the grid, it is appropriate to start the grid generation process in the heating block region, where the finest grid is necessary in order to describe the heat transfer from the heating wires within the required accuracy. As described in chapter 4, the heating wire geometry was replaced by the substitutive geometry. The discretization of this geometry, depicted in fig. 27, serves as the starting point for the coarsening process and therefore had to be done as the first step.

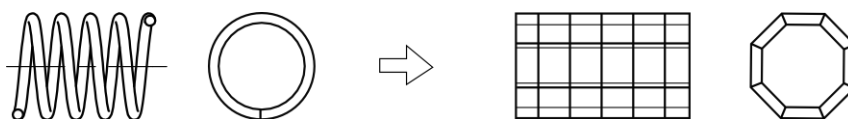


Fig. 27 – Simplification and discretization of the heating wire geometry

Subsequently the heating block geometry was discretized as shown in fig. 28. The fine discretization of the inner coil region was chosen due to the need to resolve the flow through the wire supports. The favorable geometry of the heating block allowed the Sweeping (Cooper) method to be applied in order to form a three dimensional grid.

The cells in the region where the source terms are to be set, marked grey in the fig. 28, were grouped into one cell zone (further referenced as the heating cell zone). Consequently the entire domain contains as many heating cell zones as many heating blocks are present in the heating unit. The reason for this grouping, partly outlined in chapter 4, is clear from the detailed heat transfer model description in chapter 5.

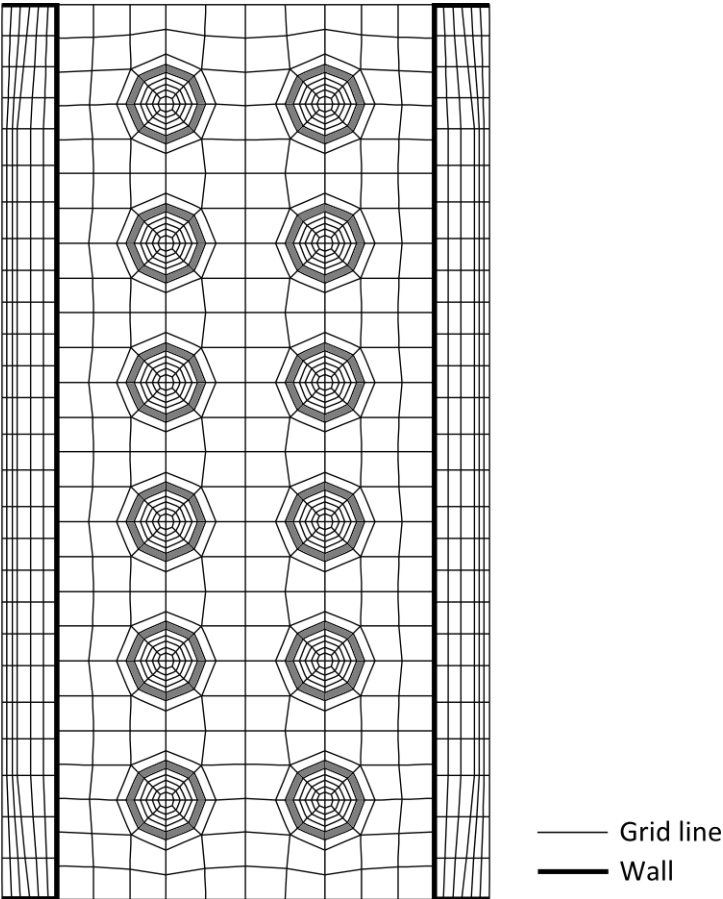


Fig. 28 – A cross sectional view of the heating block grid

The grid coarsening strategy can be demonstrated on the cross sectional views of the top chamber visualized in fig. 29. After the geometry is split into logical parts, the Pave meshing scheme is applied to the source faces to make a transition between fine and coarse regions. The two dimensional mesh is then extruded to the perpendicular direction with use of the Sweep volume meshing method. A coarsening in both directions is achieved by appropriate selection of vertical or horizontal source faces.

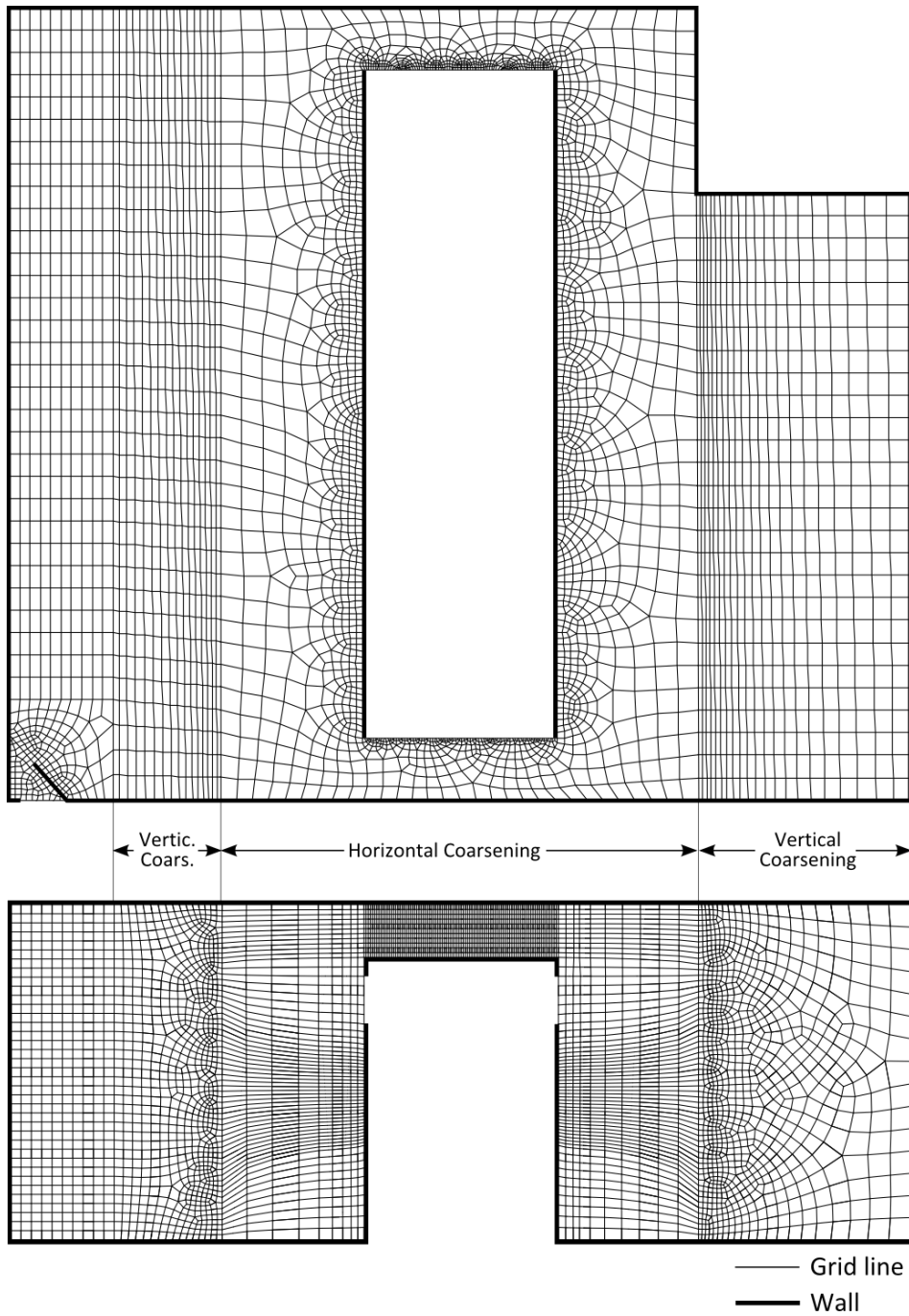


Fig. 29 – Top chamber grid visualization

The abovementioned method of bidirectional pave-sweep coarsening was used also in the top region of the inlet channel as shown in fig. 30.

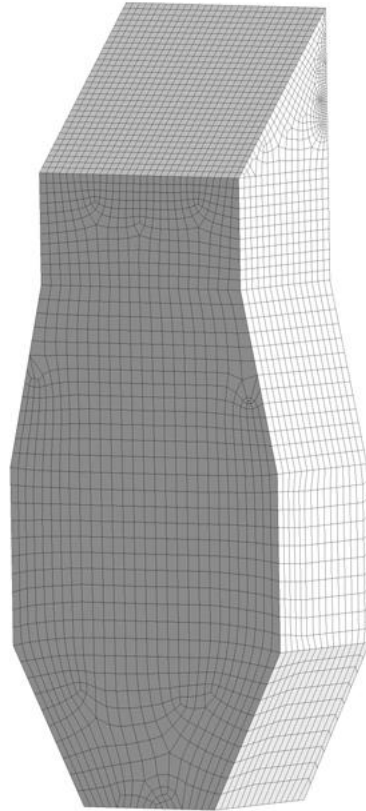


Fig. 30 – Inlet channel computational grid

The resulting grid properties are summarized in tab. 6. The worst quality of the unstructured grid cells is within the allowable limit (0.9) and therefore the grid is expected to be able to provide a converging solution.

	Cells number	Hexahedra cells		Tetrahedra / Pyrmid cells	
		Number	Maximum EquiSize Skew	Number	Maximum EquiSize Skew
Inlet channel	27 630	27 630	0.76	0	-
Top chamber	307 999	307 999	0.83	0	-
Heating assembly	1 212 190	1 187 092	0.76	25 098	0.86
Overall geometry	1 547 819	1 522 721	0.83	25 098	0.86

Tab. 6 – Grid summary

6.3 Solver

As mentioned in the introduction of this chapter, Ansys Fluent v14.0 has been selected as a CFD solver. Tab. 7 summarizes the selected settings. The discussion of the most important parameters and assumptions follows below the table.

Logical Section	Property	Setting
Solver	Dimension	3D
	Double precision	yes
	Type	Pressure-based
	Time	Steady state
	Energy equation	On
	Turbulence model	Realizable k- ϵ Standard wall function
	Gravity	On
Material Properties	Density	Incompressible ideal gas
	Heat capacity	Piecewise polynomial interpolation
	Viscosity	Constant - 1.7894e-05 [kg·m ⁻¹ ·s ⁻¹]
	Thermal conductivity	Constant - 0.0242 [W·m ⁻¹ ·K ⁻¹]
	Molecular weight	Constant - 28.966 [kg·kmol ⁻¹]
Inlet Boundary	Boundary condition type	Mass-flow-inlet
	Mass flow rate	0.3167 [kg·s ⁻¹]
	Turbulence specification method	Intensity and hydraulic diameter
	Turbulence intensity	10%
	Hydraulic diameter	0.25
	Temperature	20°C
Outlet Boundary	Boundary condition type	Pressure outlet
	Gauge pressure	0 [Pa]

Tab. 7 – Solver settings

The low speed nature of the considered flow problem allows the flow to be considered incompressible, which implies the density not to be related to the pressure. The temperature variations of the density are possible to resolve using the ‘Incompressible ideal gas’ approach which uses an equation of state together with the reference pressure level to determine the density value. Since the flow is expected to be turbulent, it is crucial to utilize an appropriate turbulence model. In last several years, the two equations turbulence models such as $k-\epsilon$ have become dominant in industrial CFD applications because of the favorable accuracy-to-costs ratio. Despite the fact that the $k-\epsilon$ model is known to fail when the isotropic turbulence assumption is violated and also to under-predict separated flows, it has been selected as the turbulence model in the current case due to high computing power requirements of more accurate models such as Reynolds stress model or LES.

The qualitative reasoning of the selection of the boundary conditions was discussed in chapter 6.1. While the values of the temperature and inlet turbulence characteristics are straightforward, it is appropriate to note that the value of the inlet mass flow rate was determined based on the measured values provided by the manufacturer.

6.4 Solution process

The Fluent iteration process with the computational grid and solver settings described in chapters 6.2 and 6.3 resulted in a converging solution. However, the solution included a reversed flow in 1579 faces of the outlet, which is illustrated in the fig. 31.

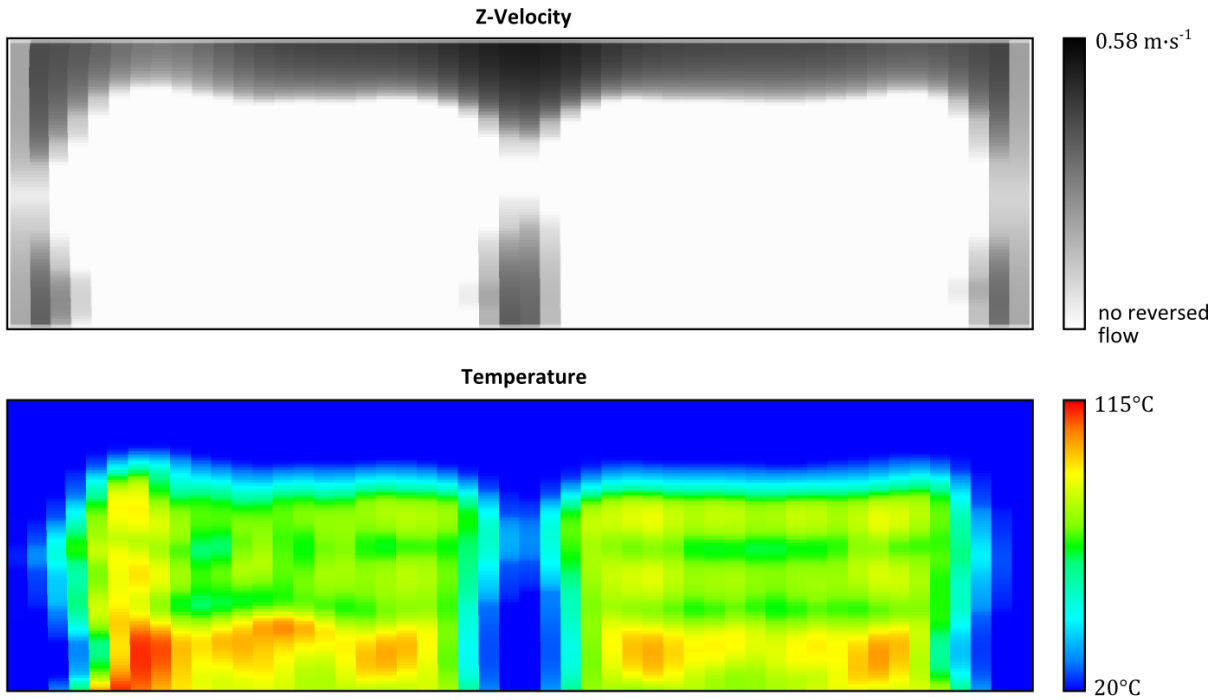


Fig. 31 – Illustration of the reversed flow at the outlet

The presence of the reversed flow suggests an inappropriate selection of the downstream domain boundary. Nevertheless, as discussed in details in chapter 6.1, the downstream boundary cannot be moved because of the high computing power requirements caused by the drum discretization. As can be seen mainly from the temperature field at the outlet, air with the free stream properties enters the domain through the outlet and poses a non-realistic boundary condition. Since the determination of the temperature and turbulence levels for the reversed flow is impossible, the obtained solution is unacceptable and it has been decided to introduce a thin porous zone at the outlet to suppress the reversed flow. The visualization of the porous zone is shown in fig. 32.

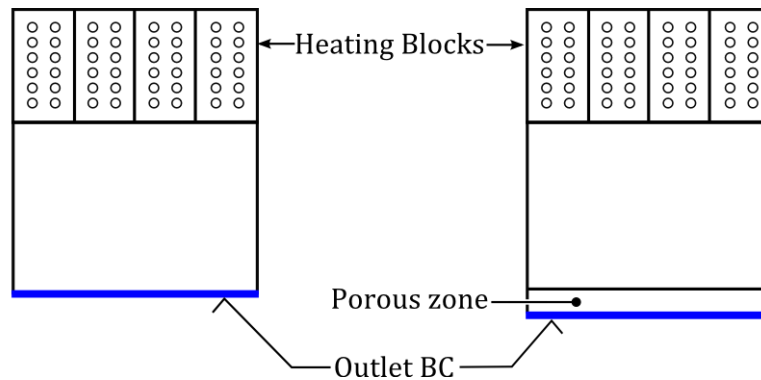


Fig. 32 – Porous zone near the outlet boundary

Tab. 8 summarizes the values of the porous zone settings.

Property		Value
Direction-1 Vector		(1,0,0)
Direction-2 Vector		(0,1,0)
Relative Velocity Resistance Formulation		On
Viscous resistance	Direction-1	0
	Direction-2	0
	Direction-3	1e+08
Fluid porosity		1

Tab. 8 – Porous zone settings

With the modified geometry including the porous zone, the second iteration process was performed. The formation of reversed flow was successfully suppressed. To allow the continuity equation residue to drop below the stochastic Fluent convergence criterion $1e-3$ it was necessary to calculate 1078 iterations. The development of the residues together with other quantities monitored in order to verify the convergence is shown in fig. 33, fig. 34 and fig. 35.

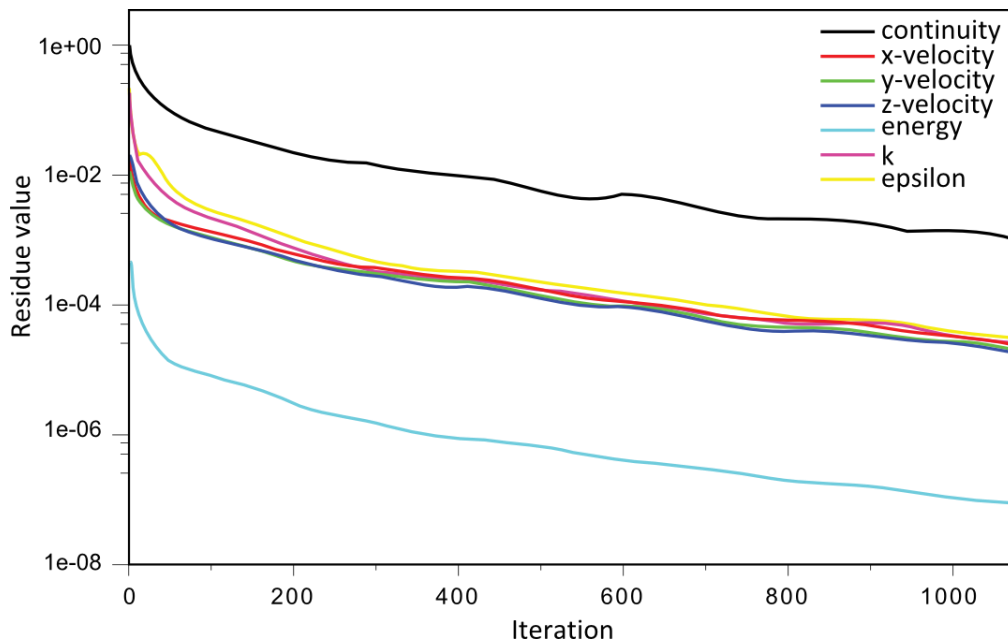


Fig. 33 – Convergence history - residues

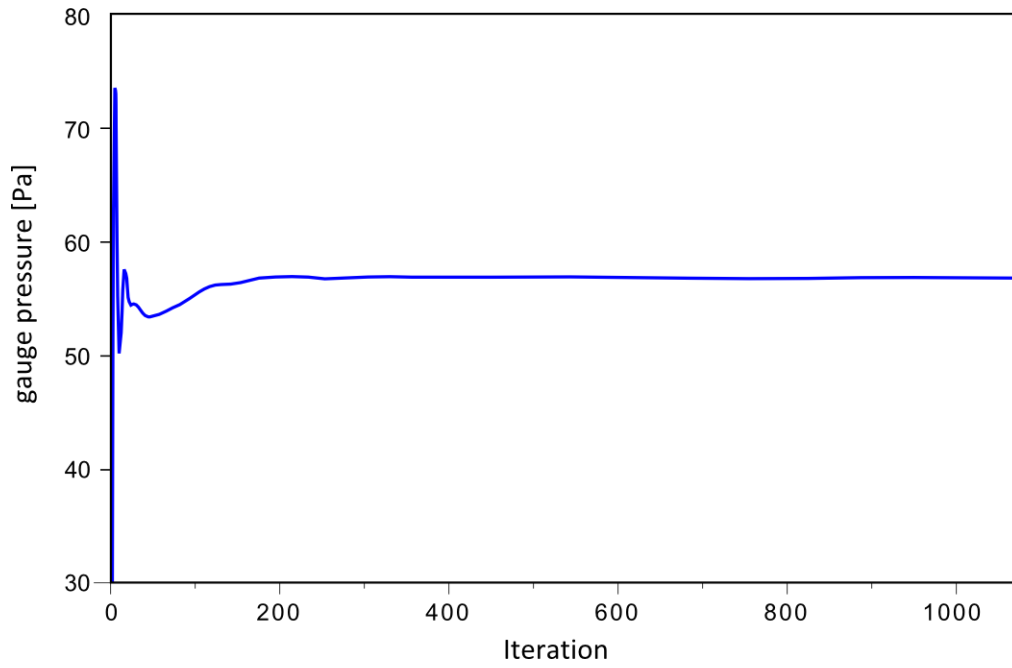


Fig. 34 – Convergence history – average pressure at the inlet

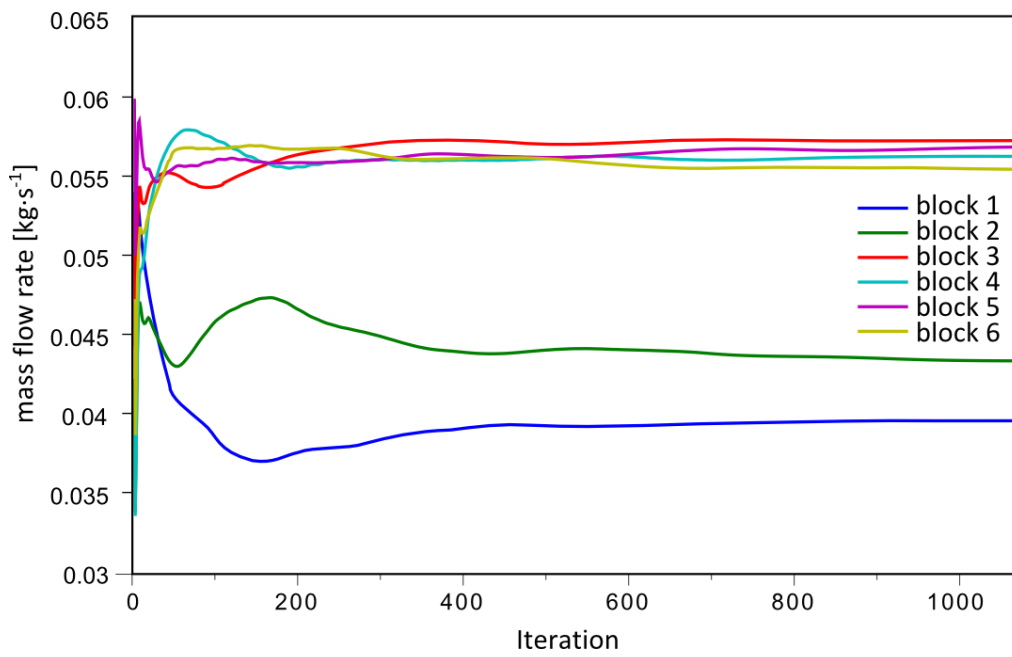


Fig. 35 – Convergence history – mass flow rates through the heating blocks

7 Results interpretation

In this chapter the data obtained by the CFD simulation are analyzed in detail. The correct interpretation of the data is essential to the identification of the weak spots and therefore to the subsequent optimization targeting.

7.1 Flow field

The following text presents the crucial aspects of the resulting flow field. Only a limited number of flow visualizations directly relevant to the text is included and a reader is encouraged to find the complete set of flow field data in appendix C.

7.1.1 Heating blocks

Since the main goal of the task is to improve the heat transfer, it is relevant to place emphasis on the investigation of the flow field within the heating blocks. Before the data are presented and interpreted it is appropriate to define the heating blocks numbering system used in the subsequent figures and tables. The numbering system and the position of the particular heating blocks within the dryer are clear from fig. 36.

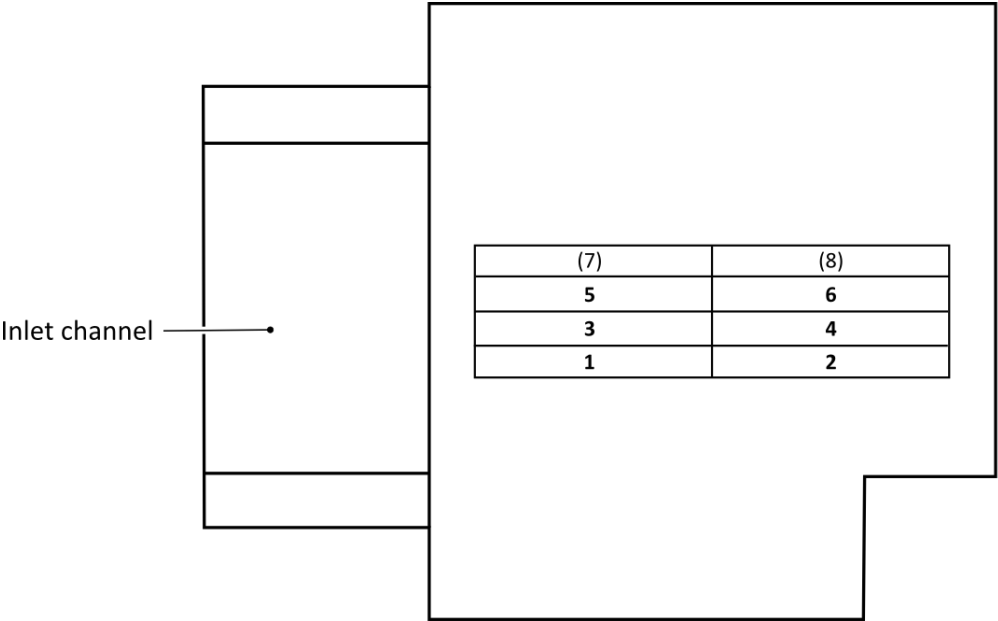


Fig. 36 – Visualization of the heating blocks numbering system

As an intuitive evaluation of the dryer geometry suggests, the flow through the heating blocks is not uniform. The level of non-uniformity can be demonstrated on the velocity contour plot in fig. 37.

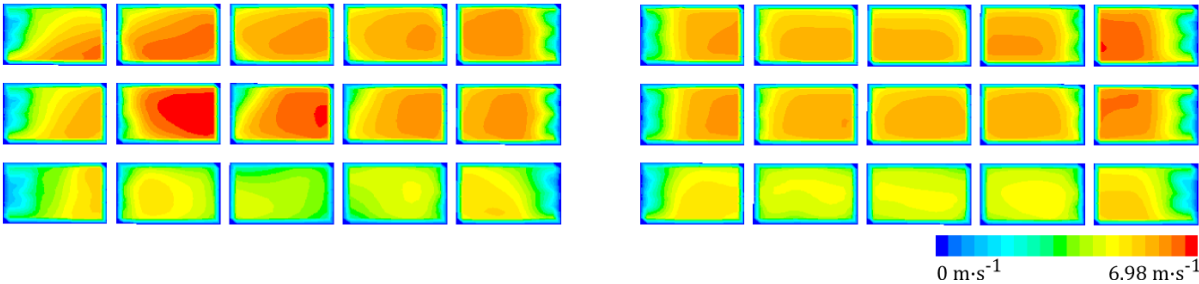


Fig. 37 – Contours of velocity magnitude at the outlet of the heating unit

It can be seen that the air velocity in the channels of the heating blocks situated in the center of the heating unit is significantly higher than in the rest of the blocks. The variation in velocity field logically implies a variation in mass flow rate. The quantified representation of the mass flow rate variation is shown in tab. 9.

	Heating block					
	1	2	3	4	5	6
Mass flow rate [$\text{kg}\cdot\text{s}^{-1}$]	0.0407	0.0446	0.0584	0.0575	0.0580	0.0566
Mass flow rate [%]	12.9	14.1	18.5	18.2	18.4	17.9
Mass flow rate sum [$\text{kg}\cdot\text{s}^{-1}$]	0.3159					

Tab. 9 – Comparison of the mass flow rates through individual heating blocks

From tab. 9 it can also be seen that the sum of the mass flow rates through the heating blocks differs from the inlet boundary mass flow rate, which was set to $0.3167 \text{ kg}\cdot\text{s}^{-1}$. This inequality is a direct consequence of the cumulation of small errors in the continuity equation at each of the discretization cells.

7.1.2 Outlet

Due to the problematic placement of the outlet boundary, described in chapter 6.1, an evaluation of the flow variables at the outlet can be done only with caution and the influence of the rotating drum has to be taken into account. The visualization of two most important quantities, namely temperature and z-velocity, is shown in fig. 38 and fig. 39 respectively.

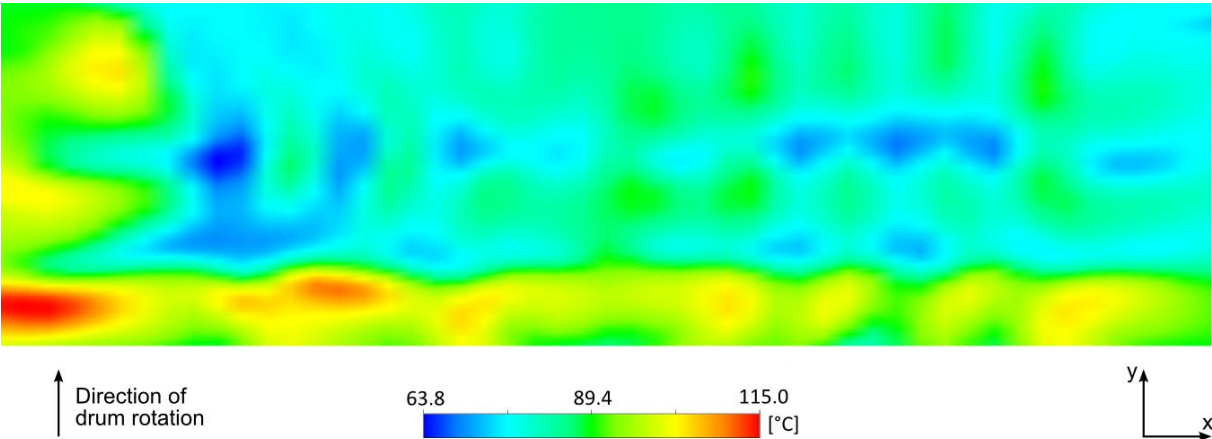


Fig. 38 – Contours of temperature at outlet

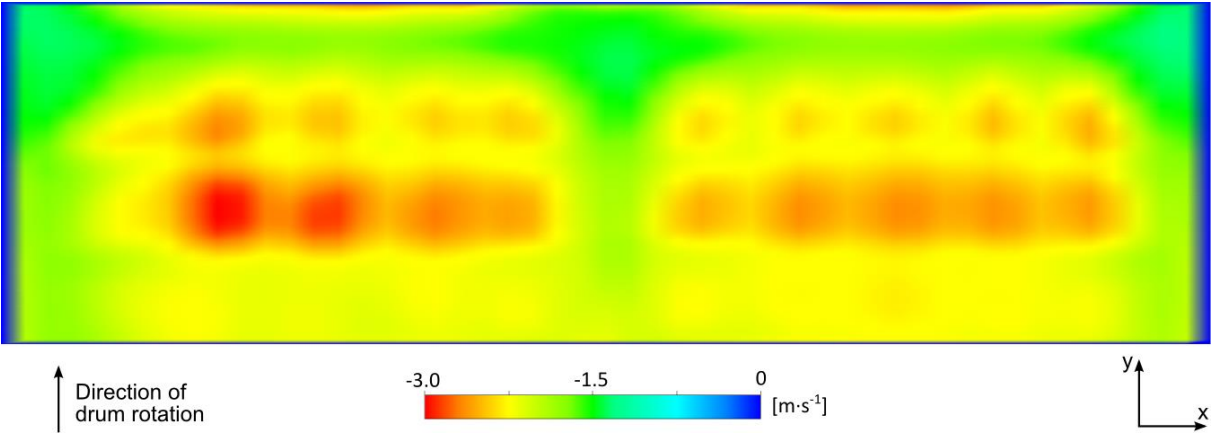


Fig. 39 – Contours of Z velocity at outlet

The temperature field clearly shows the high temperature regions to be situated on the left and bottom sides. While the increased temperatures on the left side of the outlet can be explained by the dominance of the secondary flow (see chapter 8.1.2 and fig. 48 for the definition of the term secondary flow) at the left terminal board region, the concentration of the hot air at the bottom of the outlet visualization is assumed to be a consequence of the flow non-uniformity caused by the blockage inserts present in the considered configuration of the heating unit. With regard to the direction of the drum rotation, the temperature distribution in y direction can be considered favorable as the bypass flow, which does not participate in the drying process (see fig. 3), is formed mainly by the colder air and therefore the energy losses are reduced.

It can be noted now that the position of the thermocouple described in chapter 3.3 can be considered appropriate as the maximum temperatures are expected to be in the region where the thermocouple is installed.

The z-velocity field suggests higher velocities on the left side of the outlet. This can be, similarly to the temperature field, explained by the dominance of the secondary flow at the left terminal board region which is adjacent to the inlet channel and therefore more air can pass through it.

7.2 Heating unit

The data calculated by the developed model offer a detailed insight into the heat transfer characteristics across the heating unit. The most important outcome is the quantification of the total transferred heat, which is, together with powers of individual heating blocks, listed in tab. 10.

	Heating block					
	1	2	3	4	5	6
Power [W]	3077	3079	3080	3079	3053	3043
Total power [W]	18 411					

Tab. 10 – Heat generated by the heating unit

The variation in the power, seen in tab. 10, can be explained by the non-uniformity of the flow field described above. However a direct correlation is impossible to formulate at the current stage and therefore a uniformity influence is further addressed in the subsequent chapter.

Another important quantity to be analyzed is the wire temperature. Since the wire temperature profiles share the same trend, for the further discussion it is appropriate to show only one sample as has been done in fig. 40 and fig. 41. Both the figures represent the wire temperature profile of the first branch in the heating block number 6. The straightforward representation with respect to the spatial coordinate x, shown in fig. 40, tends to bias the individual profiles. Therefore in fig. 41 the data were expanded to form a continuous profile by relating the temperature to the control volume number. The numbering of the control volumes is explained in chapter 5.4.2.2.

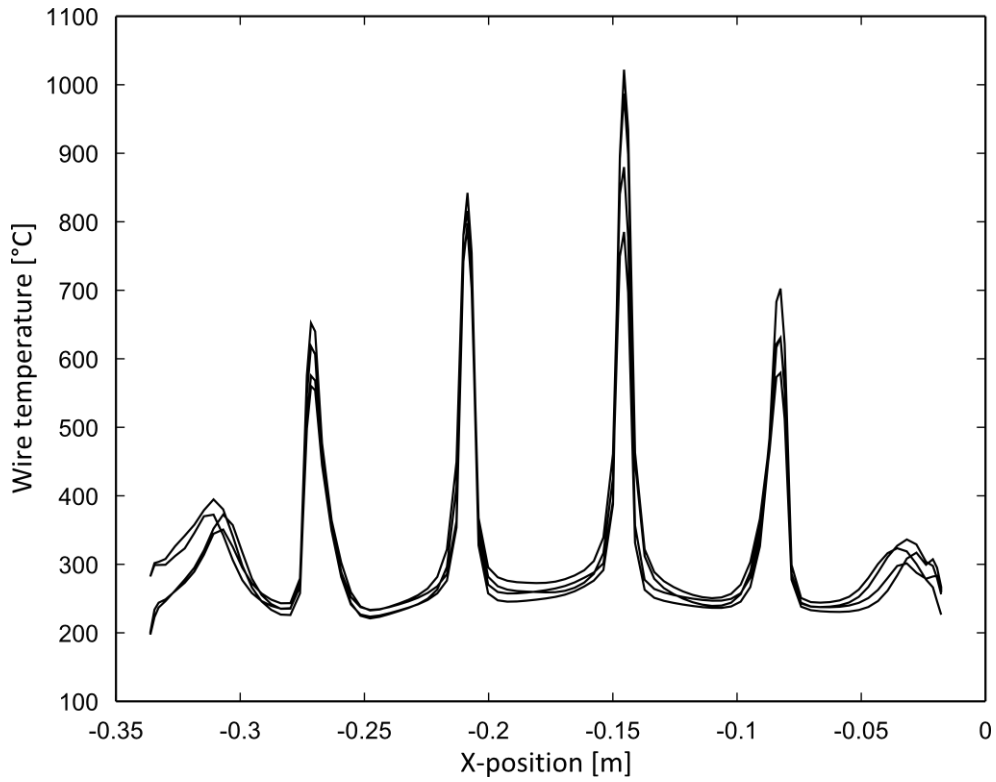


Fig. 40 – Heating wire temperature profile

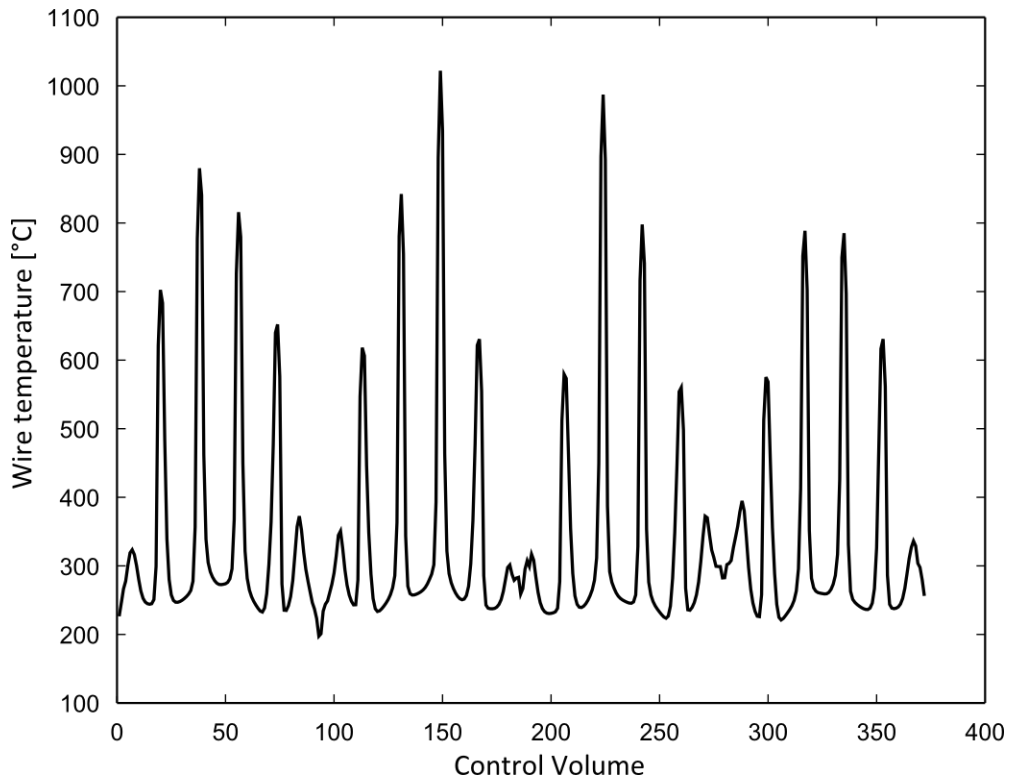


Fig. 41 – Heating wire temperature profile (expanded data relevant to one branch)

It can be seen that the overheating is localized at the regions where the wires are enclosed by the wire supports. The peak temperatures reach significant values and therefore a detailed analysis of the influence of the overheating on the heating unit power is necessary.

To evaluate the behavior of the electric properties of the heating blocks, the relevant data were grouped into tab. 11.

Heating block	Branch	Current	Voltage	Resistance
1	1	6.29	163.14	25.95
	2	6.30	162.71	25.81
	3	6.33	162.06	25.61
2	1	6.29	163.03	25.90
	2	6.31	162.70	25.79
	3	6.33	162.17	25.63
3	1	6.29	163.13	25.92
	2	6.31	162.70	25.78
	3	6.33	162.08	25.59
4	1	6.29	163.12	25.92
	2	6.31	162.75	25.80
	3	6.33	162.03	25.58
5	1	6.23	163.26	26.19
	2	6.25	162.71	26.01
	3	6.28	161.93	25.77
6	1	6.21	163.29	26.29
	2	6.23	162.78	26.12
	3	6.27	161.84	25.82

Tab. 11 – Heating unit electric circuit quantities

From the comparison it is clear that the load imbalance is negligible in the considered case and it is possible to simplify the calculation by assuming a constant voltage drop at each of the branches as when the connection with present neutral line is used.

8 Optimization

Based on the findings presented in the previous chapter, it is possible now to investigate the particular possibilities of the design optimization.

8.1 Targeting

To specify the optimization strategy it is first necessary to assess the influence of all the parameters and verify the feasibility of optimization steps associated with the particular parameter. If more than one parameter appears to significantly influence the objective quantity, it is necessary to find an appropriate combination of the parameters to achieve a maximum possible improvement.

8.1.1 Overheating

As the overheating is one of the main concerns expressed by the dryer manufacturer, it was examined with the highest priority. To evaluate the influence of the overheating on the heating unit power a balance calculation was used as the first step. The calculation utilizes the modified Churchill and Bernstein correlation developed by Comini et al.[3] to determine the overall convective heat transfer coefficient valid for the entire heating block. To evaluate the transferred heat by using the relationship

$$\dot{Q}_{CONV} = \alpha(\overline{T}_W - T_{AMB})A_{CONV} \quad Eq. 8.1$$

first the average branch wire temperature \overline{T}_W has to be determined. While Comini et al.[3] used experimental values of current and voltage to calculate the wire temperature, a purely computational nature of the approach selected for this thesis requires a computational method for the determination of the wire temperature. Similarly to the model formulation, an iterative solution of the wire temperature based on a simplified heating wire equation applied to the overall branches was used. Because the overall approach implies an omission of the conductive terms and because the radiation heat transfer was neglected, the simplified heating wire equation reads:

$$\frac{I_{AMP}^2}{2}\overline{R} = \overline{\alpha}(\overline{T}_W - T_{AMB})A_{CONV} \quad Eq. 8.2$$

where \overline{R} is the overall branch resistance and $\overline{\alpha}$ is the overall convective heat transfer coefficient. In the beginning of every iteration the resistance is calculated based on either the guessed wire temperature or the wire temperature from the previous iteration. The overheating is taken into account by introducing the overheating factor ψ and the overheated region ratio ω . The overheating factor ψ can be defined as the ratio of the superficial temperature of the overheated region $T_{W,OH}$ to the wire temperature calculated by the abovementioned iterative procedure. The overheated region ratio ω is defined as the ratio of the overheated volume of the heating wire to the overall volume of the heating wire. For the considered geometry the overheated region ratio can be expressed as:

$$\omega = \frac{V_{SUPPORTS}}{V_{WIRE}} = \frac{6 L_{SUPPORT}}{L_{COIL}} = \frac{6 \cdot 5}{320} = 0.094 \quad Eq. 8.3$$

where $L_{SUPPORT}$ is the length of the wire support. The overheating factor definition reads:

$$\psi = \frac{T_{W,OH}}{\overline{T}_W} \quad Eq. 8.4$$

The overall branch resistance can be expressed in terms of ψ and ω as:

$$\bar{R} = R_{BR}[1 + \omega\beta(\psi\bar{T}_W - T_{R0}) + (1 - \omega)\beta(\bar{T}_W - T_{R0})] \quad \text{Eq. 8.5}$$

Subsequently the current I_{AMP} can be determined by the application of the Ohm's law which allows a solution of eq. 8.2 for \bar{T}_W . It is important to note that the value of \bar{T}_W used in eq. 8.1 is not modified to take the overheated region temperature $T_{W,OH}$ into account. This can be justified by the fact that the heat transfer takes place mainly in the region outside of the wire supports where the temperature \bar{T}_W is assumed. The results of the calculation are summarized in tab. 12.

	Overheating factor			
	1	2	2.5	3
Block power [W]	3095.5	2827.6	2717.8	2620.0

Tab. 12 – Comparison of heating blocks power for various overheating factors

It can be seen that the higher overheating factors are related to a reduced heat generation rate and therefore it is reasonable to assume that a reduction of the peak temperatures can lead to an increase in the power of the heating unit. To estimate the achievable increase in the heating unit power it is possible to use the wire temperature profiles from the CFD simulation, limit the peak temperatures to the chosen value and use the limited profiles for the calculation of the generated heat. The illustration of the profile before and after limiting process is shown in fig. 42 and fig. 43 respectively.

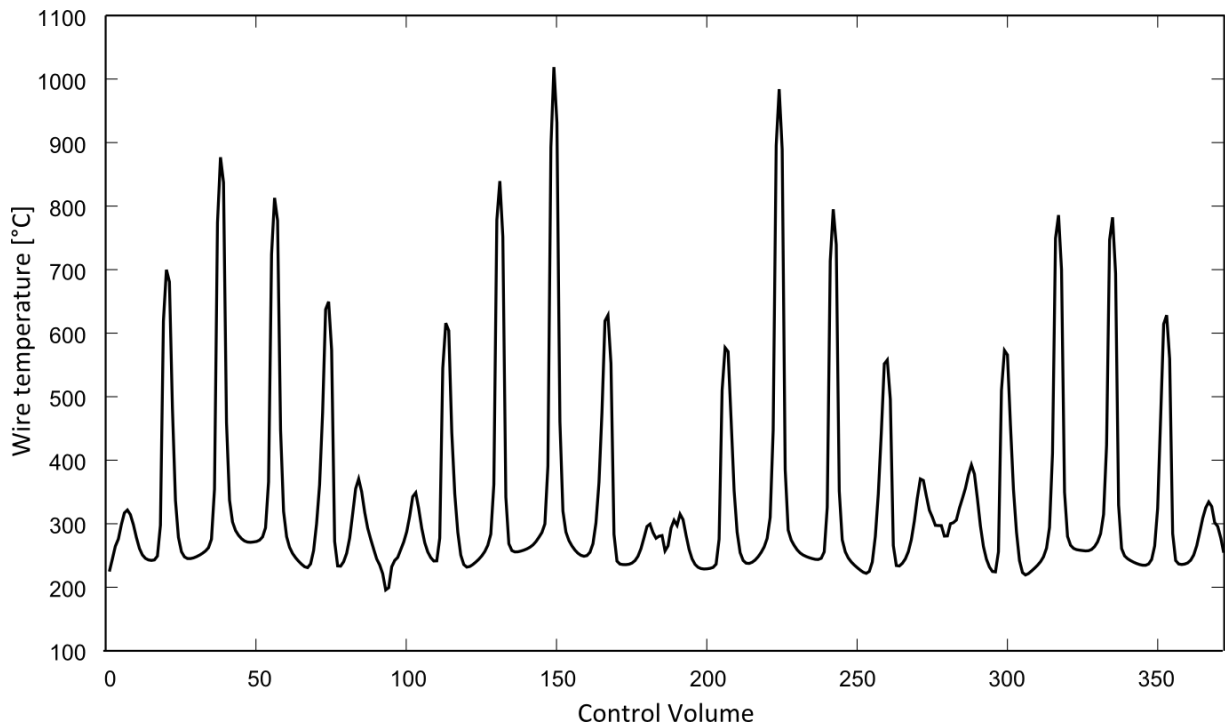


Fig. 42 – Non-trimmed wire temperature profile used to estimate the overheating sensitivity

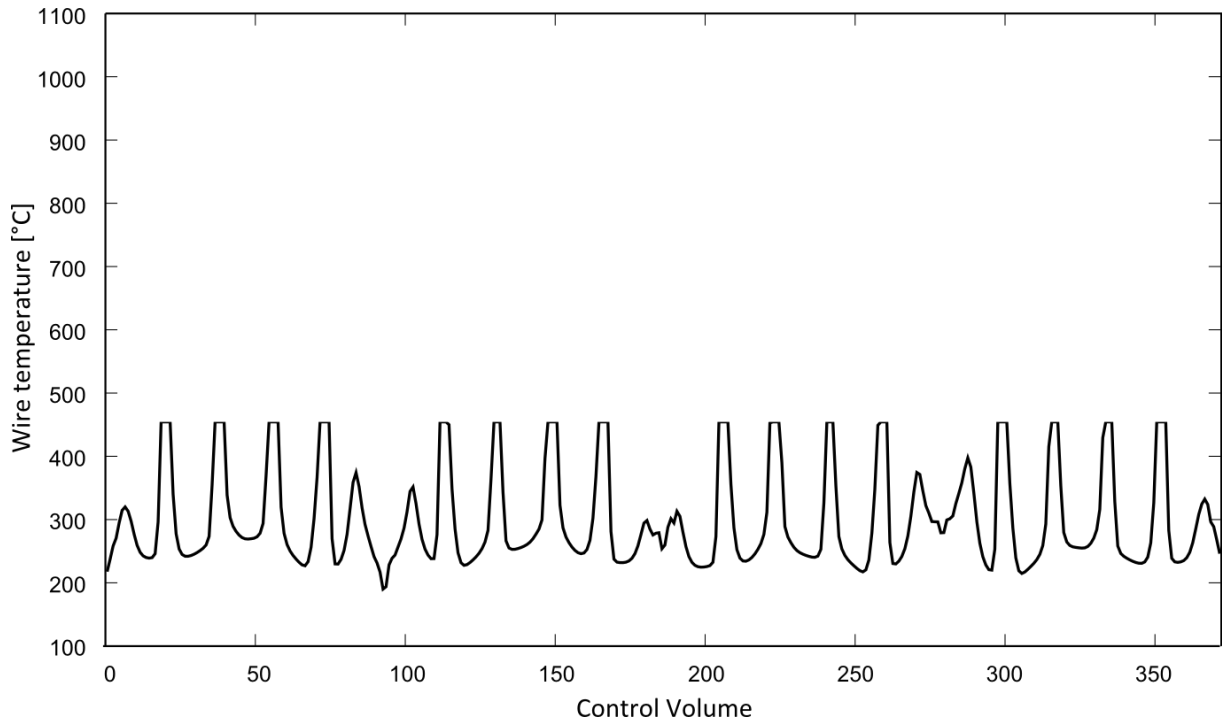


Fig. 43 - Trimmed wire temperature profile used to estimate the overheating sensitivity

The values of the heat generation rate calculated for the wire profiles limited to the temperature 450°C are listed in tab. 13.

	Heating block power [W]						Total power [W]
	1	2	3	4	5	6	
Original profile	3 077.0	3 078.6	3 080.1	3 079.4	3 053.1	3 042.8	18 411.0
Limited profile	3 082,7	3 084,5	3 084,9	3 083,4	3 063,7	3 052,1	18 451,4

Tab. 13 - Comparison of heating block powers for trimmed and non-trimmed temperature profile

An evaluation of the resulting data suggests that the increase in the heating unit power achievable by the reduction of the peak temperatures is negligible and therefore it is not suitable to further develop this optimization possibility.

To fully understand the dependence of the generated heat on the wire temperature profile it is appropriate to apply the relationship given by eq. 5.6 to a case where a heating coil is connected to a constant voltage source and subsequently to expand the relationship into the form suitable for the formulation of conclusions. The derivation starts with the basic relationship:

$$\dot{Q} = \frac{U_{RMS}^2}{R} \quad \text{Eq. 8.6}$$

The resistance R can be, for a general heating coil where only a longitudinal wire temperature variation is assumed, expressed as:

$$R = \int_W R_{1m} [1 + \beta(T_W(x) - T_{R0})] dx \quad \text{Eq. 8.7}$$

where $T_W(x)$ is a general function expressing the wire temperature as a function of the spatial coordinate x and the symbol W below the integral sign denotes an integral over the entire heating wire. Rearranging and splitting the integral yields:

$$R = \int_W R_{1m} dx + R_{1m} \beta \int_W (T_W(x) - T_{R0}) dx \quad \text{Eq. 8.8}$$

The first term on the right hand side is equal to the branch resistance and therefore can be written as:

$$\int_W R_0 dx = R_{br} \quad \text{Eq. 8.9}$$

By substituting eq. 8.8 and Eq. 8.9 into Eq. 8.6 we get:

$$\dot{Q} = \frac{U_{RMS}^2}{R_{br} + R_{1m} \beta \int_W (T_W(x) - T_{R0}) dx} \quad \text{Eq. 8.10}$$

It is clear that the main parameter determining the difference in the generated heat for two geometrically identical heating coils is the temperature integral present in the denominator. Since the temperature integral can be interpreted as the area under the temperature profile curve, it is possible to conclude that even though a local overheating increases the value of the integral and therefore lowers the heat generation rate, it is the overall shape of the temperature profile that is crucial to the resulting heat generation rate. This can be illustrated by fig. 44 where two profiles with the same value of the temperature integral are compared. It can be seen that the first profile clearly reaches higher peak temperatures. However as the values of the temperature integrals are the same, both the profiles result in the same heat generation rate.

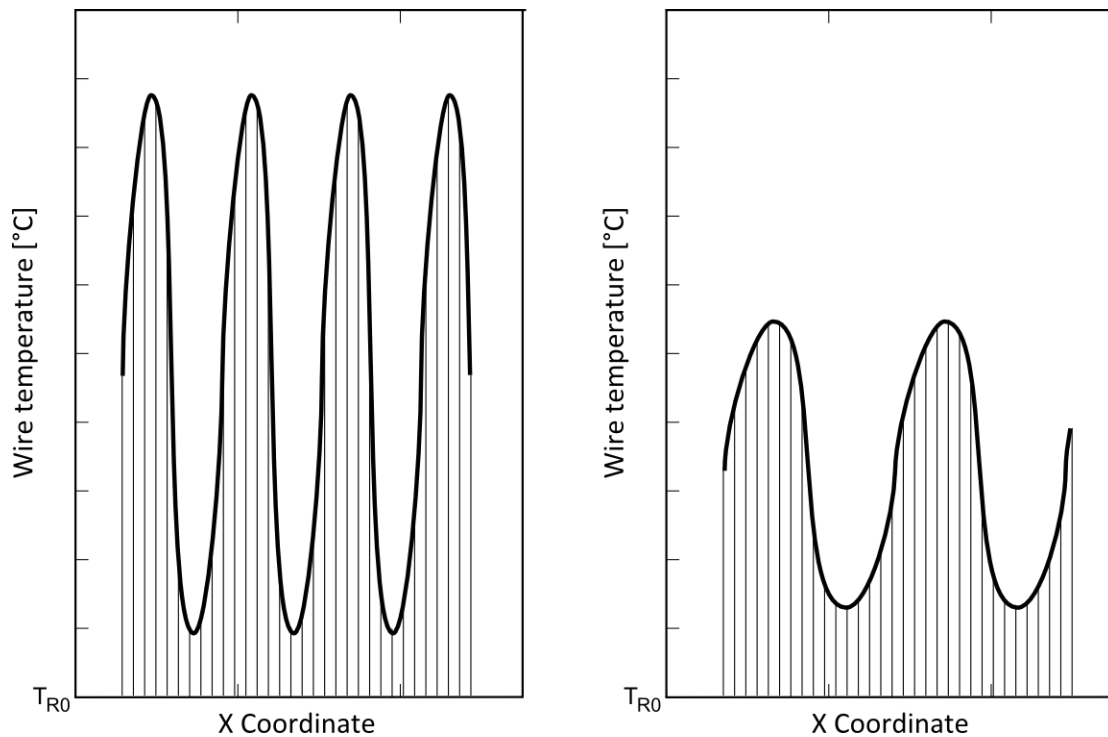


Fig. 44 – Comparison of two wire temperature profiles with the same temperature integral value

Based on the analyses performed within this chapter, a conclusion regarding the overheating significance can be made. Despite the fact that the overheating reduces the heat generation rate, its reduction does not lead to a significant increase of the heating unit power. Therefore provided that the peak temperatures are below the material limit, it is not necessary to address this problem in the optimization process. Based on the material datasheet supplied by the heating blocks manufacturer, the maximum operating temperature of the heating wires varies from 1050°C to 1100°C. As the maximum wire temperature predicted by the model is 1030°C, the temperature limit is not exceeded.

8.1.2 Flow uniformity

The non-uniform flow through the heating blocks described in chapter 7.1 raises the question of the influence of the non-uniformity on the heating unit power. To quantify the influence a CFD test case was created. The heating unit region was extracted from the original computational domain and provided with the inlet and outlet channel as shown in fig. 45. Such a configuration assures a uniform flow through the heating blocks.

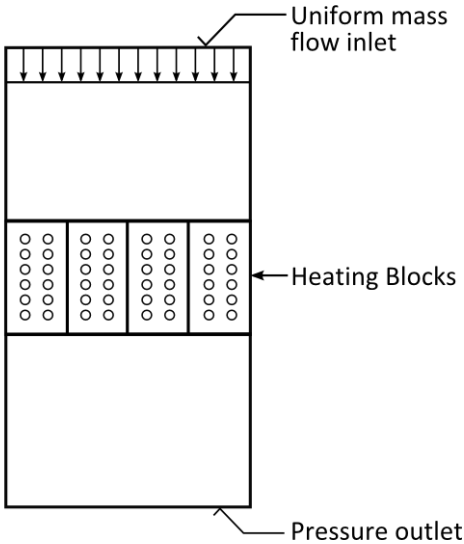


Fig. 45 – Uniform flow CFD simulation domain

The results of the CFD simulation are shown in tab. 14. Contrary to the expectations, the total heat generation rate is lower for the uniform flow test case.

		Heating block power [W]						Total power
		1	2	3	4	5	6	
Power [W]	Uniform	3 062.7	3 062.5	3 064.3	3 064.5	3 057.3	3 057.4	18 368.6
	Real	3 077.0	3 078.6	3 080.1	3 079.4	3 053.1	3 042.8	18 411.0

Tab. 14 – Comparison of the heating block powers for real and uniform flow field

To explain the results it is necessary to reveal the details of the simulations. This can be done by plotting the wire temperature profiles. To prevent the text from excess figures, only two samples demonstrating a general trend were chosen and are shown in fig. 46 and fig. 47. In the high temperature region an increase in peak temperatures can be observed while the low temperatures region shows both an increase and decrease in temperatures.

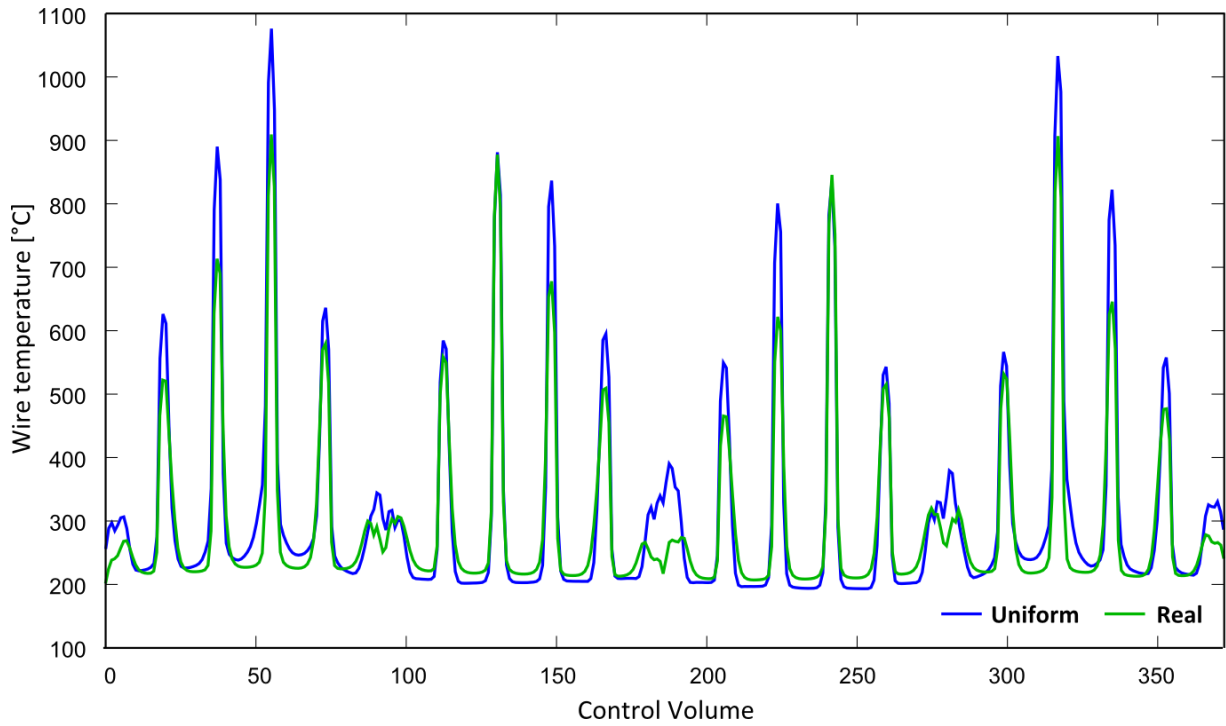


Fig. 46 – Wire temperature profiles for the heating block 1 and branch 1

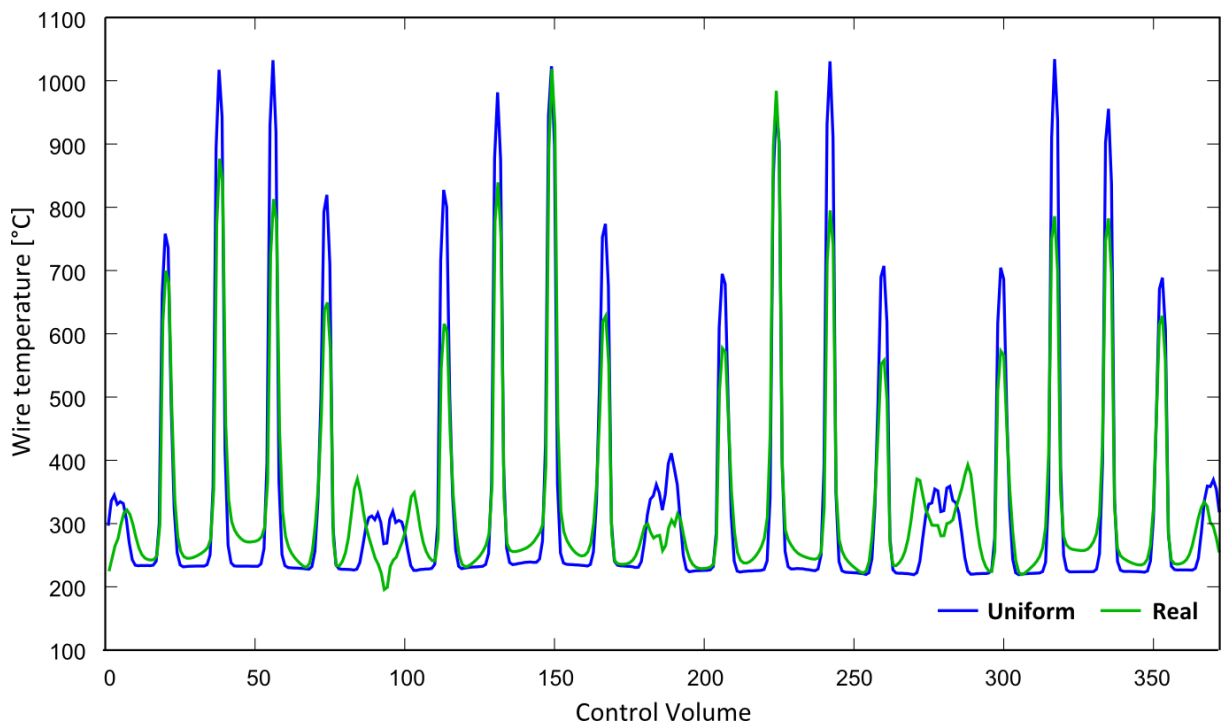


Fig. 47 - Wire temperature profiles for the heating block 6 and branch 1

The results of the uniform flow CFD simulation can be explained by a qualitative examination of the flow pattern within the heating blocks. As visualized in the fig. 48 it is possible to identify two main streams of incoming air, namely the primary and secondary flow.

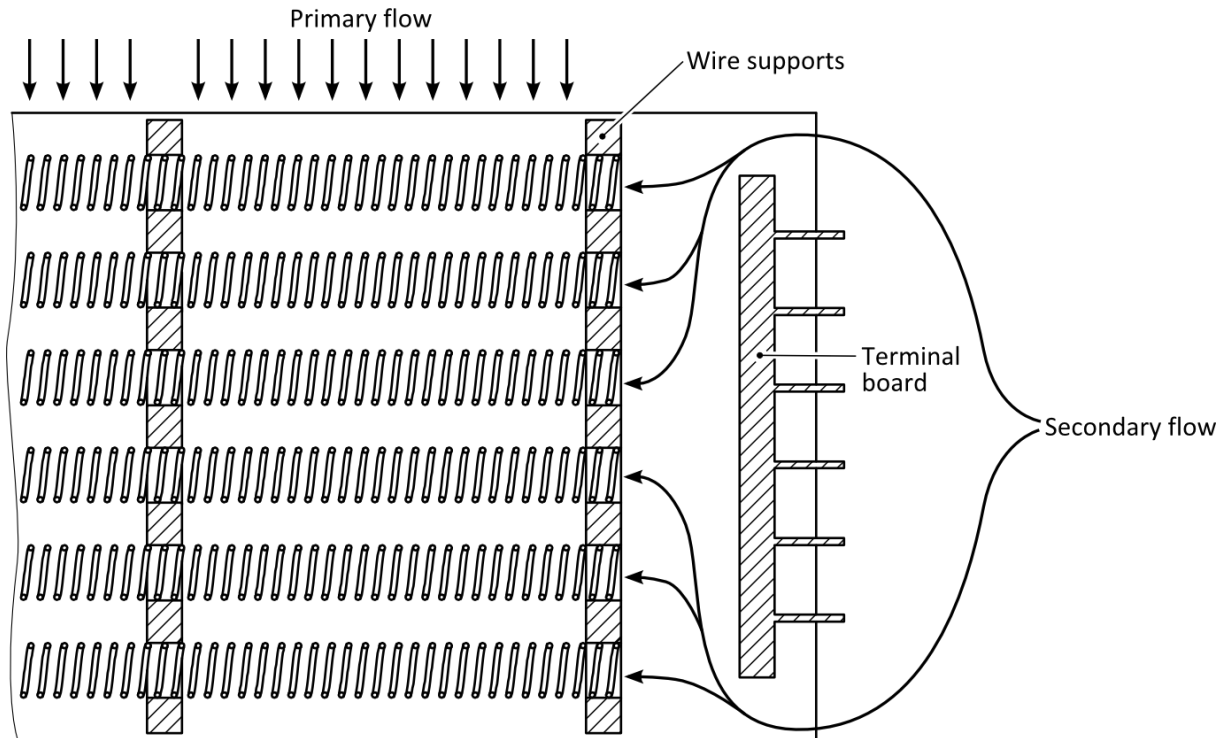


Fig. 48 – Visualization of the primary and secondary flows

While the primary flow enters the heating blocks at the top from the heating channel inlet, the secondary flow is formed by air that penetrates the heating blocks through the terminal board region and through the openings in the wire supports. Since the secondary flow is suppressed by the computational domain formulation in the uniform flow simulation, it is possible to assume that the change of the wire temperature profile is caused by the suppression. Particularly the wire temperature increase in the low temperatures region are expected to be fully related to the secondary flow characteristics as the reduced flow through the wire supports logically results in the reduction of the heat transfer and therefore in the increase in the wire temperature.

Based on the arguments mentioned above, it is possible to assume that the design changes ensuring a uniform flow through the heating blocks do not lead to improvements in heating unit power.

8.1.3 Heating channel velocity

In the vast majority of the problems where convective heat transfer intensification is demanded, it is common to consider either local or global increase of velocity. With regard to the fixed mass flow rate given by the task, only the local variant is suitable for the considered case.

The quantification of the possible increase in heating unit power due to the velocity increase can be done by employing the iterative solution described in the previous chapter. First the steady state wire temperatures are calculated for a given range of velocities which allow the subsequent determination of the current and heat generation rate. The velocity dependence of the wire temperature, current and the heat generation rate relevant to one heating branch in a free stream of air at 20°C are shown in fig. 49, fig. 50 and fig. 51 respectively.

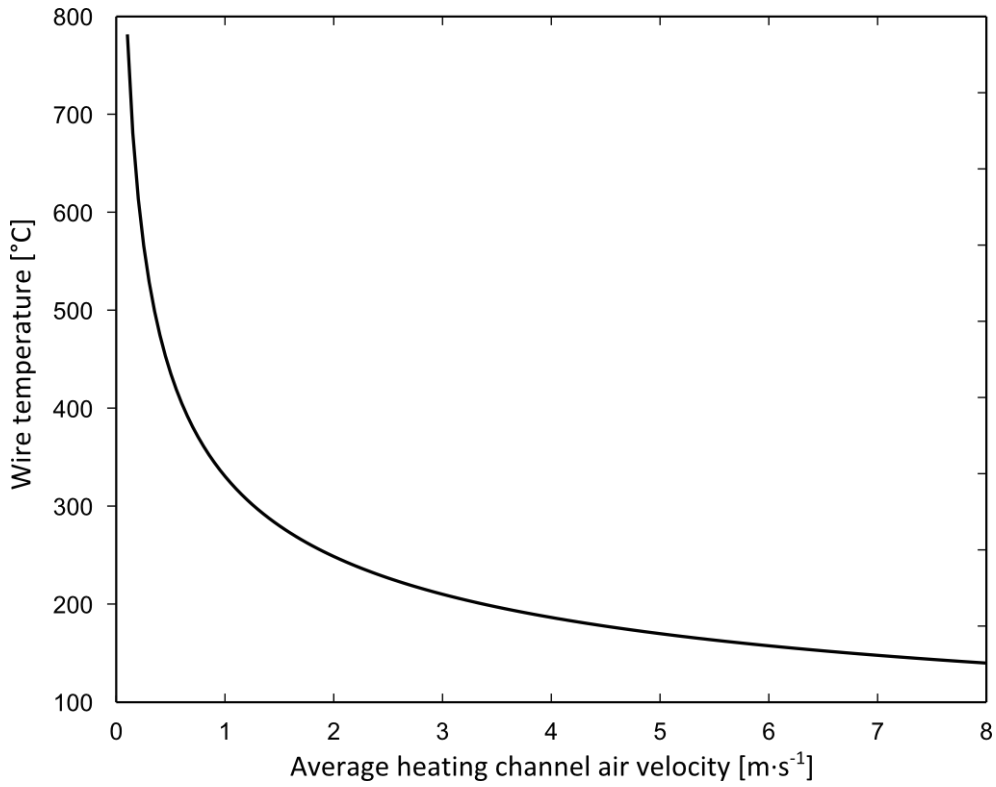


Fig. 49 – Graphical representation of the wire temperature as a function of the air velocity

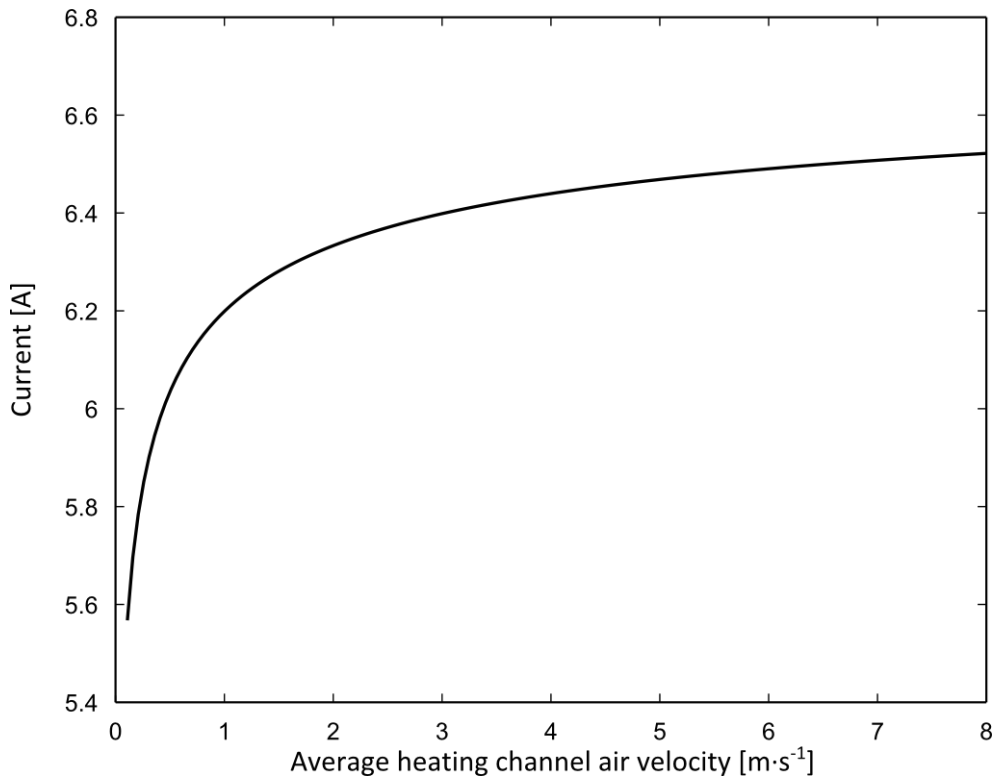


Fig. 50 - Graphical representation of the branch current as a function of the air velocity

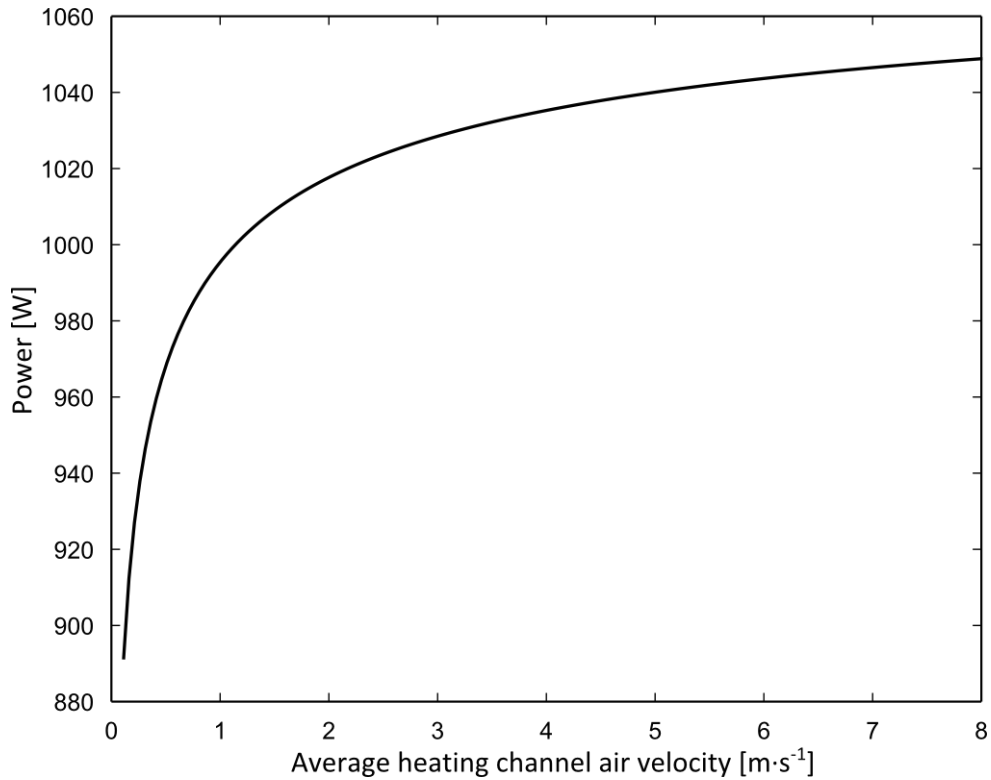


Fig. 51 - Graphical representation of the branch power as a function of the air velocity

In order to estimate the increase in the total heating unit power, it is first necessary to determine the average heating channel velocity for the considered heating unit configuration as:

$$\bar{v}_{HB} = \frac{\dot{V}_{AIR}}{n_{HB} A_{HB}} = \frac{950}{6 \cdot 0.01102} = 3.99 \approx 4 \text{ m} \cdot \text{s}^{-1} \quad \text{Eq. 8.11}$$

where \bar{v}_{HB} is the average heating channel velocity, n_{HB} is the number of heating blocks in the considered heating unit configuration and A_{HB} is the cross-sectional area of the heating block channel. Using the average heating channel velocity as a reference value, the heat generation rate increase can be estimated as:

$$\Delta\dot{Q} = \dot{Q}(\bar{v}_{HB,IN}) - \dot{Q}(\bar{v}_{HB}) \quad \text{Eq. 8.12}$$

where $\bar{v}_{HB,IN}$ is the increased average heating channel velocity. Even though the increase in the heat generation relevant to one branch can be read from fig. 51 it is necessary to assess the overall heating unit heating power and therefore tab. 15 was assembled to give an overall description for various values of $\bar{v}_{HB,IN}$.

		Increased average heating channel velocity $\bar{v}_{HB,IN}$ [m·s ⁻¹]			
		4.5	5	5.5	6
Increase in heat generation rate [W]	Branch	2.85	5.29	7.42	9.29
	Block	8.54	15.87	22.25	27.87
	Overall unit	25.63	47.61	66.75	83.62

Tab. 15 – Increase in heat generation rate for various average heating channel velocities

It is clear that the achievable increase in the heat generation rate is negligible and the design optimization employing the local velocity increase is not feasible.

8.1.4 Heating coil geometry

The last and rather radical optimization possibility lies in an adjustment of the heating coil geometry. A practical application of the coil geometry modifications is limited by the fact that the heating blocks used in all the variations of the heating unit are being supplied by an external manufacturer and therefore an in-house optimization is impossible.

To enumerate the heat generation rate for various combinations of geometry parameters, the approach involving an iterative solution of the wire temperature described in chapter 8.1.1 was used. In order to preserve the present design of the wire supports, it has been decided to keep the coil diameter unchanged and consider only variations in the helix pitch and the wire diameter.

The graphical representation of obtained data is shown in fig. 52 and fig. 53. Only suitable combinations of the helix pitch and the wire diameter were extracted from the complete set of data by limiting the wire temperature to 1000°C and by requiring the relationship:

$$S_c > 0.1d \quad \text{Eq. 8.13}$$

to be valid for the suitable combinations of the parameters. The constant 0.1 in eq. 8.13 was chosen to discard the non-realistic combinations where the wires forming the coil touch or intersect each other. However an increase of the constant is to be considered with respect to the limitation of the convective heat transfer coefficient correlation, which is expected to predict invalid values when the amount of inner spaces is decreased.

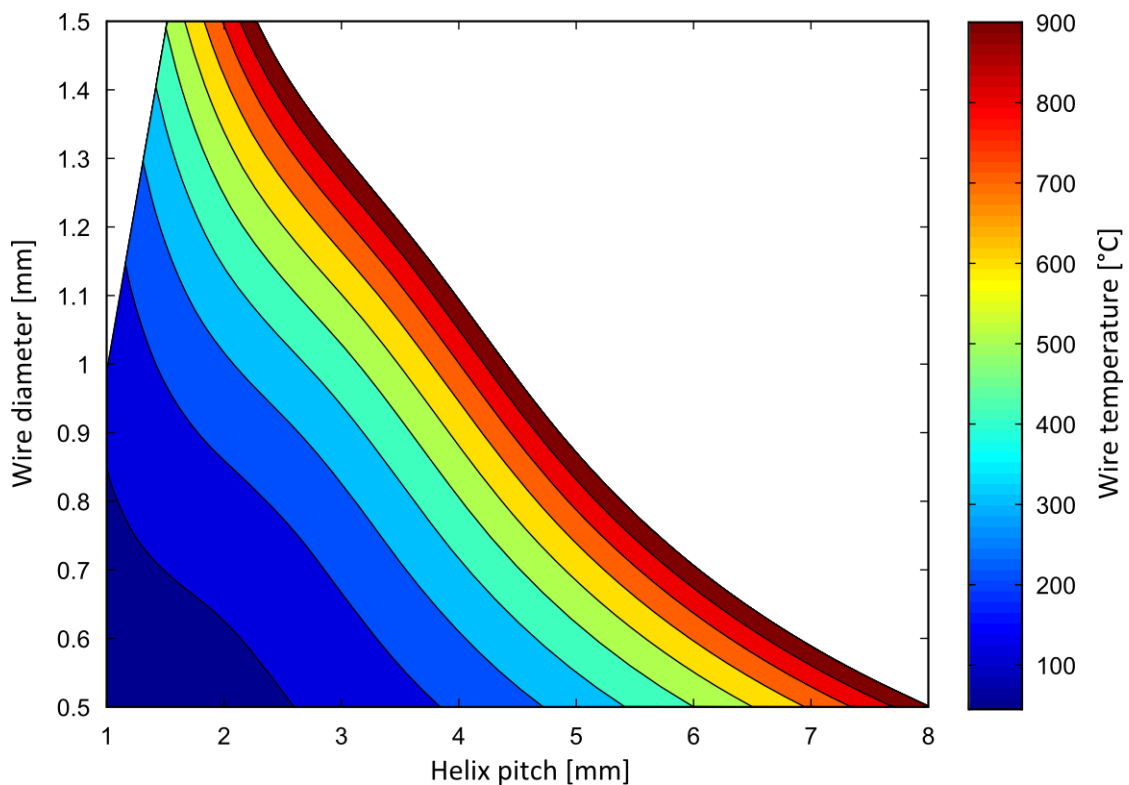


Fig. 52 – Visualization of the wire temperature dependence (white color = non-suitable combinations)

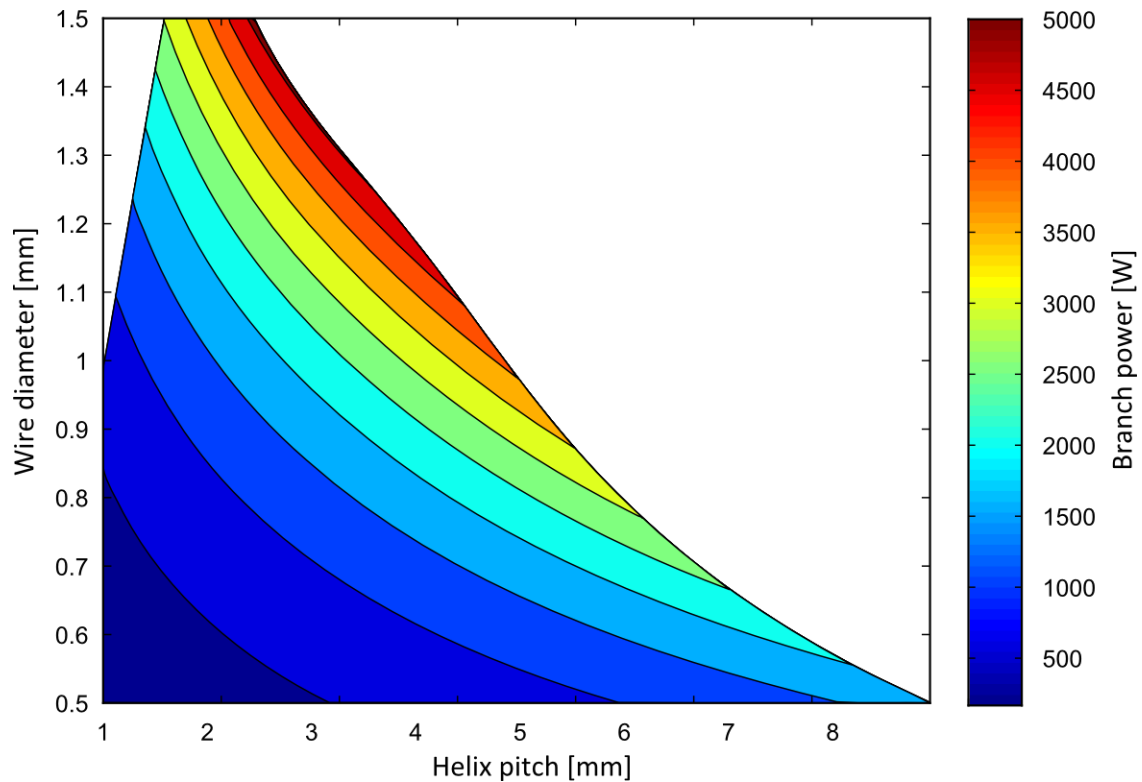


Fig. 53 - Visualization of the branch power dependence (white color = non-suitable combinations)

From the trends of the contour plots it is clear that a significant increase in the heating branch power is achievable. It is important to note that an increase in the power is always connected with an increase in the wire temperature. This poses a substantial complication as an increase in the wire temperature causes an increase in the peak wire temperatures due to the overheating in the wire supports region. Since the values of the overheated regions in the present design case are at the top of the allowable limit, any changes of the coil parameters can be introduced only if the overheating effect is reduced.

To select an appropriate combination of the coil parameters, many factors such as standard wire diameters and other production related characteristics have to be considered and therefore an explicit specification of the optimal parameter values is omitted.

8.2 Evaluation of optimization possibilities

The targeting procedure described in the previous chapter revealed a narrow space for the optimization of the heat transfer within the considered tumble clothes dryer. Except for the heating coil geometry modifications, none of the considered optimization techniques shows a significant improvement potential.

9 Conclusion

Within a scope of this thesis a complex optimization analysis of an electrically heated tumble clothes dryer was performed. The present case of the dryer was evaluated by the CFD simulation. Due to the geometrical simplifications necessary to reduce computing power requirements it was inevitable to introduce a model describing the heat transfer from the helically coiled heating wires in cross flow.

The concept of the model was based on the experimental study of heating wires in cross flow performed by Comini et al.[3]. The overall balance approach was modified in order to resolve the details of the heat transfer. While conductive and convective heat transfer mechanisms were taken into account, radiation was neglected. The main source of error is expected to be located in the wire supports region where the cross flow condition is locally violated.

Since the pulling effect of the rotating drum in the region adjacent to the outlet was, after extensive considerations, neglected, the results of the present case CFD analysis are expected to be distorted in the vicinity of the outlet boundary. To ensure a correct solution it is necessary to include a rotating drum in the simulation, which was unacceptable due to the available computing power. With respect to the long term research plan of NETME Centre, the question of the drum flow will be addressed in a close future as drying processes optimization is one of the key features of the collaboration with laundry equipment manufacturers. Thus the current work can be expanded and made more accurate by introducing a suitable method for the description of the drum flow.

The assessment of the improvement possibilities revealed a very narrow space for the heat transfer optimization. Neither of the factors emphasized in the task, namely the local wire overheating and the non-uniform flow through the heating blocks, does not significantly influence the resulting power of the heating unit. The only suitable improvement possibility including modifications of the heating coil geometry is limited by a combination of two negative factors. The first one, being purely of a manufacturing nature, lies in the fact that the heating blocks are supplied by an external company and the process involving the modifications of the heating coils geometry is therefore complicated. The second factor is related to the overheating located in the wire supports region. The present case analysis revealed the maximum temperature of the heating wire to be only approximately 50°C lower than the maximum allowed operating temperature. Since all the improvements based on the modifications of the heating coil geometry are connected with an increase in the wire temperature, it is possible to employ such a modification only if the overheating effect is reduced in the problematic region.

From a wider perspective, a resistive heating can be, after neglecting the heat losses in wiring, considered as 100% effective. Therefore the only optimization possibility employing the present heating coil geometry lies in the temperature dependence of the heating wire resistance. A reduced wire temperature causes a lower resistance which results in a higher heat generation rate. Since the change in resistance of the considered heating wire material is approximately 3% per 100°C it is clear that the heat generation rate cannot be increased significantly by lowering the wire temperature.

The presented thesis delivers a comprehensive answer to a practical problem given by a leading manufacturer of laundry equipment. Even though the demanded enhancement was proven to be unachievable for the considered conditions, it is necessary to highlight the fact that the detailed insight in the device characteristics together with the found physical limitations can serve as a basis for future design improvements. Moreover the heat transfer model developed within the thesis can be utilized in CFD simulations of devices including helically coiled heating wires.

10 References

- [1] ANSYS INC., *Ansys 14.0 Help: Fluent*, c 2011
- [2] MEIER, ALEXANDRA VON. *Electric power systems: a conceptual introduction*, New Jersey, A Wiley-Interscience publication, c 2006, xv, 309 p., ISBN-13: 978-0-471-17859-0
- [3] G. COMINI, et al., *Forced convection heat transfer from banks of helical coiled resistance wires*, International Journal of Thermal Sciences, Volume 47, Issue 4, April 2008, Pages 442-449, ISSN 1290-0729, 10.1016/j.ijthermalsci.2007.03.009.
- [4] ALEXANDER, C.K., SADIKU, M.N.O., *Fundamentals of Electric Circuits*, McGraw-Hill Higher Education, 2005
- [5] PRIMUS CE, *Technical specifications: Industrial tumble dryers*, Product brochure, 2012

Appendix A – Fluent UDF source code

```

#include "udf.h"
#include<stdio.h>
#define max_zone_ID 8
#define min_zone_ID 3
#define ncellzone 9696 // number of cells in one zone (ie in one heating block)
float sourceterm[max_zone_ID+1][ncellzone],Tw[max_zone_ID+1][ncellzone];
void LoadFromFile()
{
FILE *fp2;
int i,j,idcko;
float sourceval,Twloc;
char fname[20];
for (j=min_zone_ID;j<=max_zone_ID;j++)
{
sprintf(fname, "%s%i%s", "SourceTerms-z", j, ".dat");
fp2 = fopen(fname, "r");
if (fp2 != NULL)
{
for (i=0;i<ncellzone;i++)
{
fscanf (fp2, "%i", &idcko );
fscanf (fp2, "%f", &sourceval );
fscanf (fp2, "%f", &Twloc );
sourceterm[j][idcko]=sourceval;
Tw[j][idcko]=Twloc;
}
}
else
{
Message("Can't open file '%s' for reading\n", fname);
}
fclose(fp2);
}
}
DEFINE_SOURCE(SpiralHeatSourceWhat, c, t, dS, i)
{
C_UDMI(c,t,0) = sourceterm[THREAD_ID(t)][c];
C_UDMI(c,t,1) = Tw[THREAD_ID(t)][c];
return sourceterm[THREAD_ID(t)][c];
}
DEFINE_EXECUTE_AT_END(execute_at_end)
{
int dom_ID = 1;
int i,n;
cell_t c;
Domain *domain = Get_Domain(dom_ID);
Thread *thread;
Thread *tf;
face_t f;
FILE *fp;
float x[ND_ND], xf[ND_ND], min_face_x, max_face_x, cell_width;
fp = fopen("FlowData.dat", "w");
if (fp != NULL)
{
for (i=min_zone_ID;i<=max_zone_ID;i++)
{
thread = Lookup_Thread(domain, i);
begin_c_loop(c, thread)
{
C_CENTROID(x, c, thread);
min_face_x = x[0];
max_face_x = x[0];
c_face_loop(c,thread,n)

```

```
{
f = C_FACE(c, thread, n);
tf = C_FACE_THREAD(c, thread, n);
F_CENTROID(xf, f, tf);
if (xf[0]<min_face_x)
{
min_face_x = xf[0];
}
else if (xf[0]>max_face_x)
{
max_face_x = xf[0];
}
}
cell_width = max_face_x - min_face_x;
fprintf(fp, "%i %g %g %g %g %g %g %g %g %g %i\n", c, C_U(c, thread), C_V(c,
thread), C_W(c, thread), C_T(c, thread), x[0], x[1], x[2], C_VOLUME(c, thread),
cell_width,
i);
}
end_c_loop(c, thread);
}
}
else
{
Message("Can't open file for writing\n");
}
fclose(fp);
system("DryerHeatingMin.bat");
LoadFromFile();
}
```



```

end
Data(Data(:,7)>y_center,11)=1; % Y position index assignment
Data(:,12)=round(Data(:,10)/nzb+0.45); % Branch index assignment
Data(:,13)=2*Data(:,10)-Data(:,11); % Wire block index assignment
Data(:,14)=Data(:,13)-(Data(:,12)-1)*4-(Data(:,10)-(2*Data(:,12)-1)).*(-
1).^Data(:,11); % Wire branch index assignment
Data(:,15)=sqrt(Data(:,2).^2+Data(:,3).^2+Data(:,4).^2); % Velocity magnitude

alpha=zeros(nwb*nx,nb);
Cminus=zeros(nwb*nx,nb);
Cplus=zeros(nwb*nx,nb);
Aconv=zeros(nwb*nx,nb);
Rcell=zeros(nwb*nx,nb);
Tamb=zeros(nwb*nx,nb);
Lengths=zeros(nwb*nx,nb);
Vol=zeros(nwb*nx,nb);
Xcoord=zeros(nwb*nx,nb);
WireIndex=zeros(nwb*nx,nb);

talpha=zeros(nwb*nx,1);
tAconv=zeros(nwb*nx,1);
tRcell=zeros(nwb*nx,1);
tTamb=zeros(nwb*nx,1);
tVol=zeros(nwb*nx,1);
tRe=zeros(nwb*nx,1);
tNu=zeros(nwb*nx,1);
tLengths=zeros(nwb*nx,1);
tXcoord=zeros(nwb*nx,1);
tWireIndex=zeros(nwb*nx,1);

for i=1:nb % loop over branch indexes
    for j=1:nwb % loop over branch wire indexes
        [bx,~,bxn] = unique(Data(Data(:,12)==i & Data(:,14)==j,6));
        tTamb=accumarray(bxn,Data(Data(:,12)==i & Data(:,14)==j,5),[],@mean)-
273.15; % Temperatures averaging
        tRe=accumarray(bxn,Data(Data(:,12)==i &
Data(:,14)==j,15),[],@mean)*D_equiv(ver)/kinem_visc; % Reynolds number
        tNu=0.3+((0.62.*tRe.^0.5*Pr^(1/3)).*((1+(tRe./282000).^(5/8))).^(4/5))./(1+
(0.4/Pr)^(2/3))^0.25; % Nusselt number
        talpha=tNu*lambda/D_equiv(ver); % Convective heat transfer coefficient
        tLengths=accumarray(bxn,Data(Data(:,12)==i & Data(:,14)==j,16),[],@mean);
        % Control volume length = cfd cell length
        tAconv=pi*D_cent(ver)*pi*d_wire(ver)*tLengths/helix_pitch(ver);
        %Convection heat exchange area
        tRcell=Rlm(ver)*tLengths; % Electrical resistance per cell
        % Computational cell volume (= sum of CFD cell volumes)
        tVol=accumarray(bxn,Data(Data(:,12)==i & Data(:,14)==j,9),[],@sum);
        tXcoord=accumarray(bxn,Data(Data(:,12)==i & Data(:,14)==j,6),[],@min);
        tWireIndex=accumarray(bxn,Data(Data(:,12)==i & Data(:,14)==j,13),[],@mean);
        if (mod(j,2)==0)
            Tamb((j-1)*nx+1:j*nx,i)=tTamb;
            alpha((j-1)*nx+1:j*nx,i)=talpha;
            Aconv((j-1)*nx+1:j*nx,i)=tAconv;
            Rcell((j-1)*nx+1:j*nx,i)=tRcell;
            Vol((j-1)*nx+1:j*nx,i)=tVol;
            Lengths((j-1)*nx+1:j*nx,i)=tLengths;
            Xcoord((j-1)*nx+1:j*nx,i)=tXcoord;
            WireIndex((j-1)*nx+1:j*nx,i)=tWireIndex;
        else
            Tamb((j-1)*nx+1:j*nx,i)=flipud(tTamb);
            alpha((j-1)*nx+1:j*nx,i)=flipud(talpha);
            Aconv((j-1)*nx+1:j*nx,i)=flipud(tAconv);
            Rcell((j-1)*nx+1:j*nx,i)=flipud(tRcell);
            Vol((j-1)*nx+1:j*nx,i)=flipud(tVol);
            Lengths((j-1)*nx+1:j*nx,i)=flipud(tLengths);
        end
    end
end

```

```

        Xcoord((j-1)*nx+1:j*nx,i)=flipud(tXcoord);
        WireIndex((j-1)*nx+1:j*nx,i)=flipud(tWireIndex);
    end
end
Lengths_plus=[Lengths(2:end,:); zeros(1,numel(Lengths(1,:)))] ; % Length of j+1 cell
Lengths_minus=[zeros(1,numel(Lengths(1,:))]; Lengths(1:end-1,:) ] ; % Length of j-1
                                                    cell
Cplus=k_w*Acond(ver)./(Lengths/2+Lengths_plus/2);
Cminus=k_w*Acond(ver)./(Lengths/2+Lengths_minus/2);
Cminus(1,:)=0; % Adiabatic boundary condition
Cplus(end,:)=0; % Adiabatic boundary condition
A=zeros(nwb*nx,nwb*nx); % Coefficients matrix
b=zeros(nwb*nx,1); % Right hand side vector
Tw=ones(nwb*nx,nb).*250; % Initial guess of the wire temperature
Twold=zeros(nwb*nx,nb); % vector of old wire temperatures (for the convergence
                        conditioning)
twonorm=zeros(nb); % vector of 2 norms of (Tw-Twold) (convergence criterion)
eps=1e-5; % convergence threshold
max_it=100; % maximum number of iterations
for it=1:max_it
    R=sum(Rcell.*(1+Beta*(Tw-T_Rref))); % Calculation of branch resistances based
    on current Tw
    U_N=(R(2)*R(3)*U_c(1)+R(1)*R(3)*U_c(2)+R(1)*R(2)*U_c(3))/(R(2)*R(3)+R(1)*R(3)+
    R(1)*R(2)); % Voltage between grid neutral line (not present) and wye
    connection midpoint
    U=U_c-U_N; % Line to Wye middle point voltages
    U_amp=abs(U); % Line to Wye middle point voltages amplitude
    U_RMS=U_amp/sqrt(2); % Line to Wye middle point voltages RMS values
    I=U_RMS./R; % Currents through individual heating block branches
    Twold=Tw;
    % Assembly and solution of the linear systems
    for i=1:nb
        A=diag(I(i)^2*Rcell(:,i)*Beta-Cplus(:,i)-Cminus(:,i)-
        alpha(:,i).*Aconv(:,i)) + diag(Cplus(1:end-1,i),1) + diag(Cminus(2:end,i),-
        1);
        b=I(i)^2*Rcell(:,i)*(Beta*T_Rref-1)-alpha(:,i).*Aconv(:,i).*Tamb(:,i);
        Tw(:,i)=linsolve(A,b); % solution of the linear system A*Tw=b
    end
    itcrit=norm(Tw-Twold, 2); % convergence criterion
    if (itcrit<=eps)
        break; % loop break (if convergence threshold satisfied)
    end
end

end
SourceTerms=alpha.*Aconv.*(Tw-Tamb)./Vol; % Calculation of CFD energy equation
                        source terms [W/m3]
HeatTrans(z)=sum(sum(alpha.*Aconv.*(Tw-Tamb))); % Transferred heat (per heating
                        block)

fprintf(LogFile,'Currents: Branch 1 - %f | Branch 2 - %f | Branch 3 - %f\n', I);
fprintf(LogFile,'Heat Generated: %f\n', HeatTrans(z));
disp(['Calculation of zone ' num2str(zones(z)) ' finished at iteration '
num2str(it) ' with residue ' num2str(itcrit)]);
fprintf(LogFile, 'Calculation of zone %i finished at iteration %i with residue %e.
Exporting data\n',zones(z), it, itcrit);
fprintf(LogFile, '--\n');
% Data export
start=1;
Export=zeros(numel(Data(:,1)),3);
for i=1:nb
    for j=1:nwb*nx
        Export(start:start+7,:)= [Data(Data(:,13))==WireIndex(j,i) &
        Data(:,6)==Xcoord(j,i) ,1),ones(8,1)*SourceTerms(j,i), ones(8,1)*Tw(j,i)];
        start=start+8;
    end
end

```

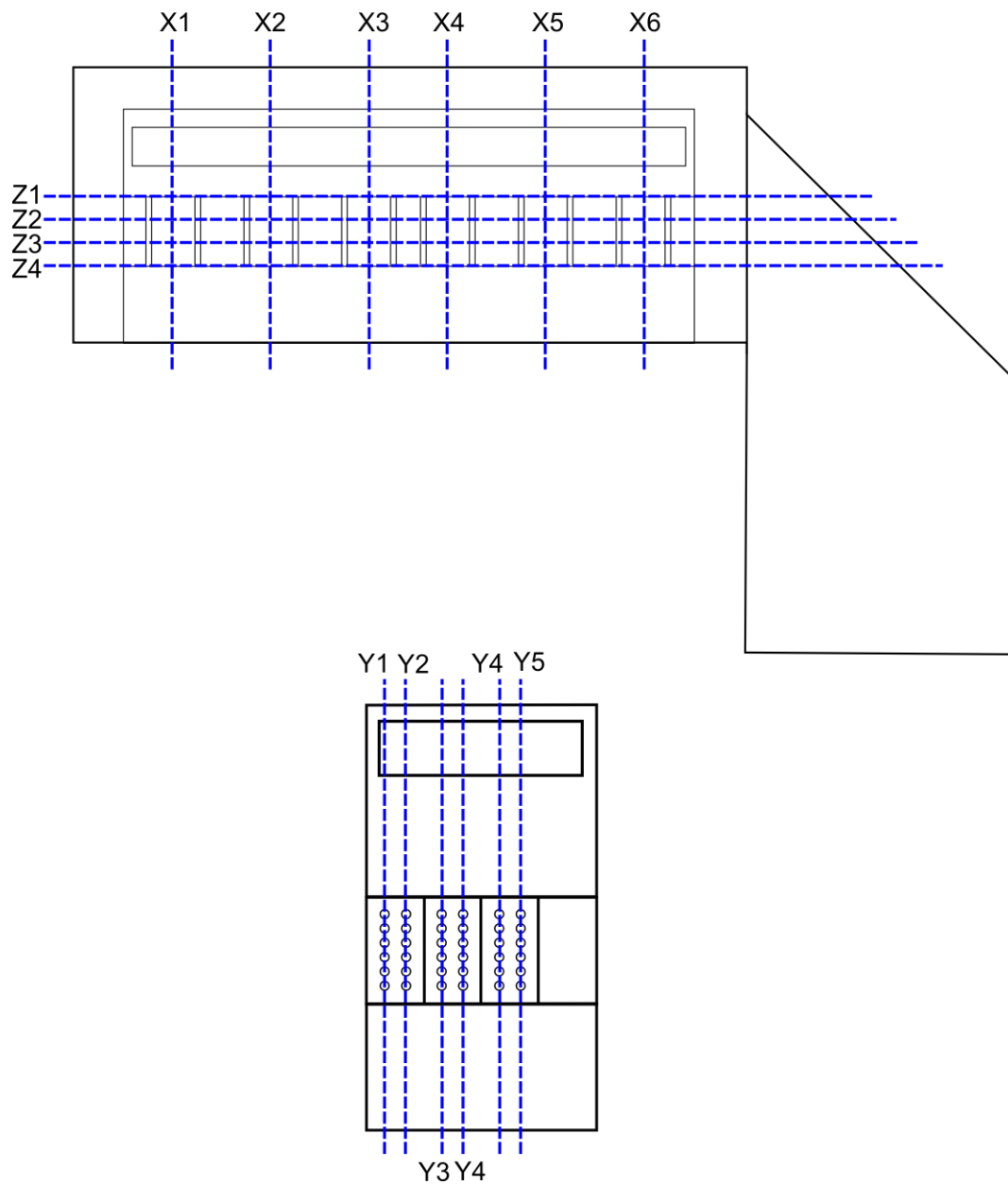
```
        end
    end
    exp_fname = strcat('SourceTerms-z',num2str(zones(z)),'.dat');
    dlmwrite(exp_fname, Export, ' ');
end
HeatTransTot=sum(HeatTrans); % Total transferred heat
fprintf(LogFile, 'Total heat transfered: %f\n', HeatTransTot);
fclose(LogFile);
```

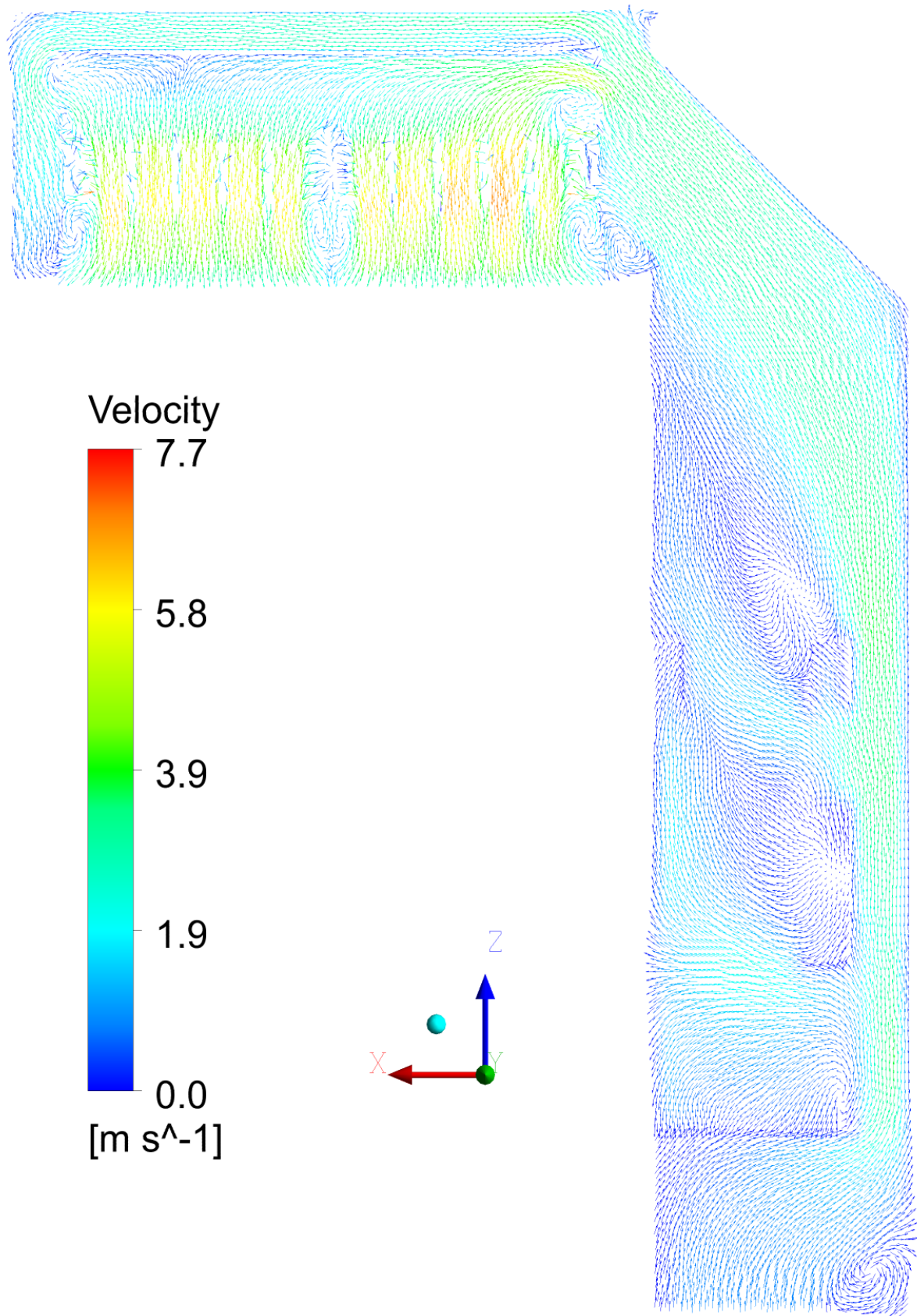
Appendix C – Visualization of the CFD results

Appendix content

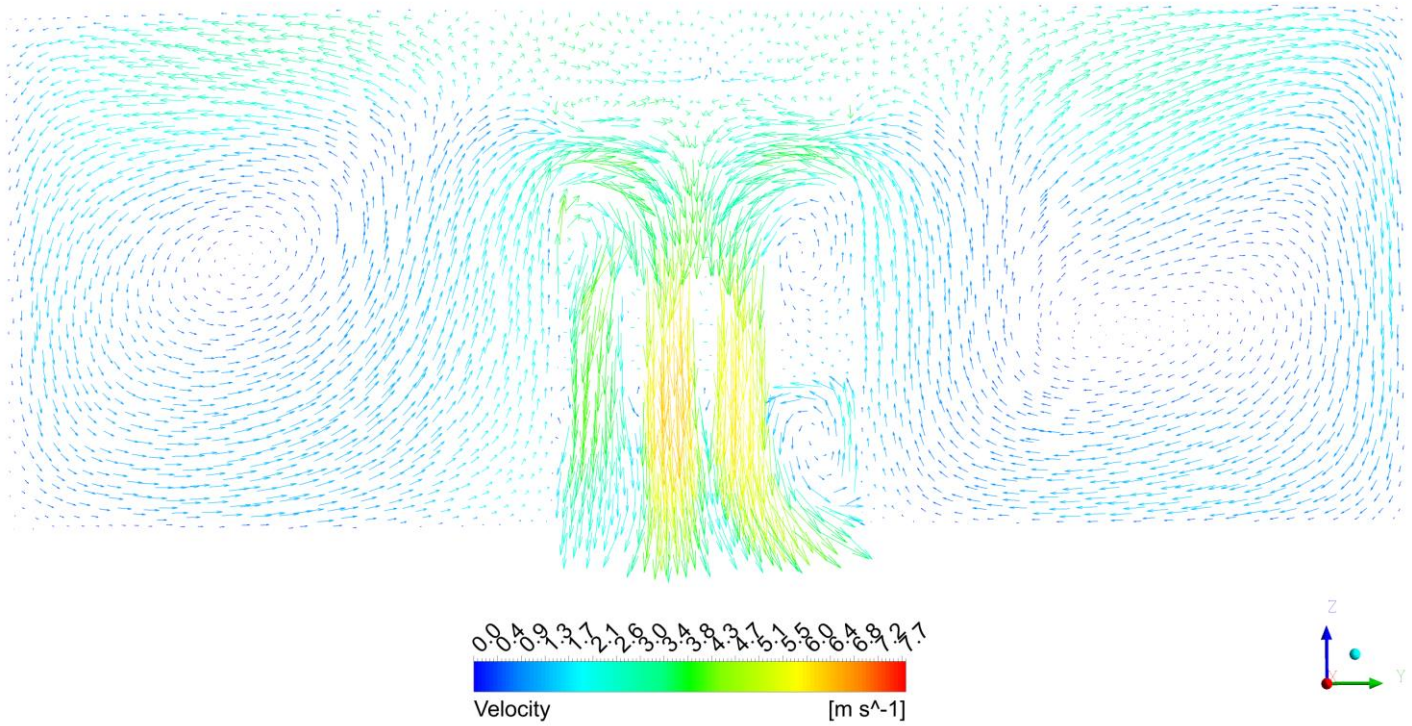
- Velocity vectors at plane Y1
- Velocity vectors at plane X2
- Velocity vectors at plane Y5
- Contours of velocity magnitudes at plane Y1
- Contours of velocity magnitudes at plane Y2
- Contours of velocity magnitudes at plane Y3
- Contours of velocity magnitudes at plane Y4
- Contours of velocity magnitudes at plane Y5
- Contours of velocity magnitudes at plane Y6
- Contours of velocity magnitude at plane Z1
- Contours of velocity magnitude at plane Z2
- Contours of velocity magnitude at plane Z3
- Contours of velocity magnitude at plane Z4
- Contours of temperature at plane Y1
- Contours of temperature at plane Y3
- Contours of temperature at plane Y6
- Contours of temperature at plane X1
- Contours of temperature at plane X2
- Contours of temperature at plane X3
- Contours of temperature at plane X4
- Contours of temperature at plane X5
- Contours of temperature at plane X6

Cutting planes notation

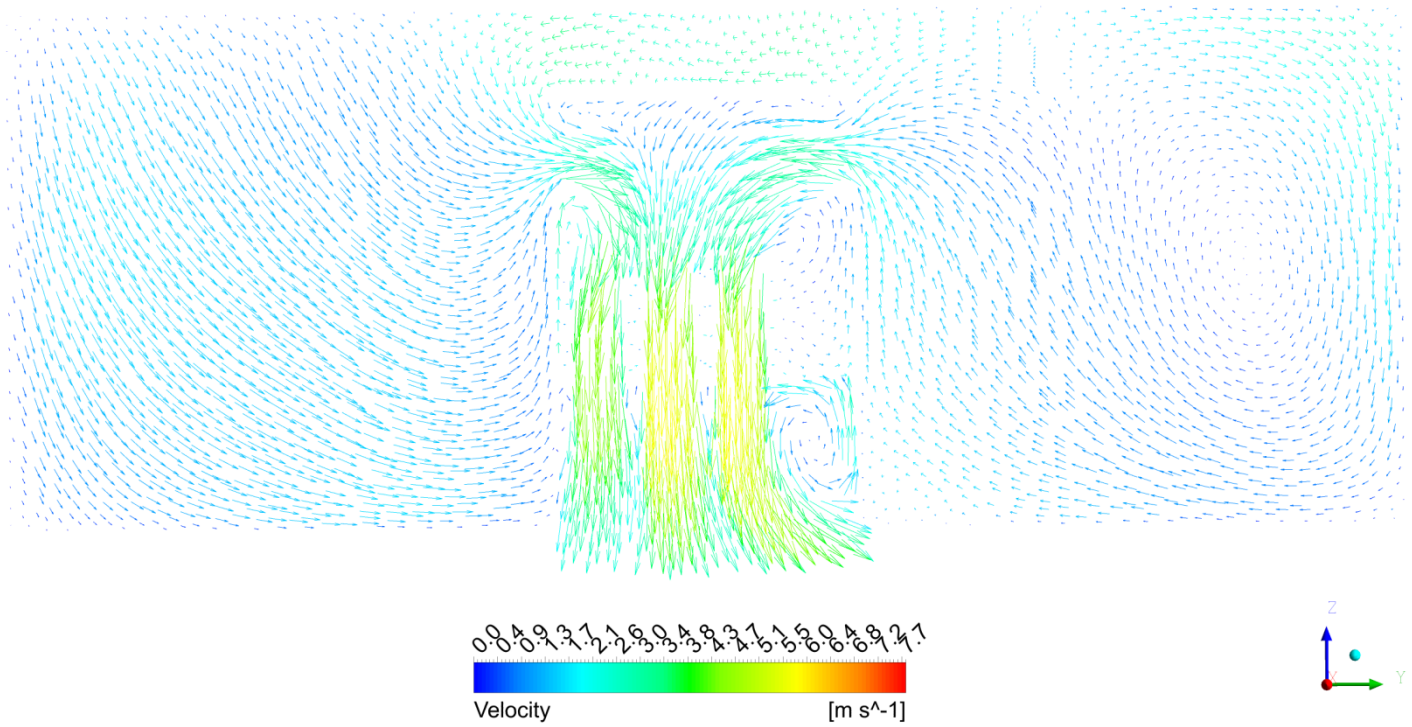


Velocity vectors at plane Y1

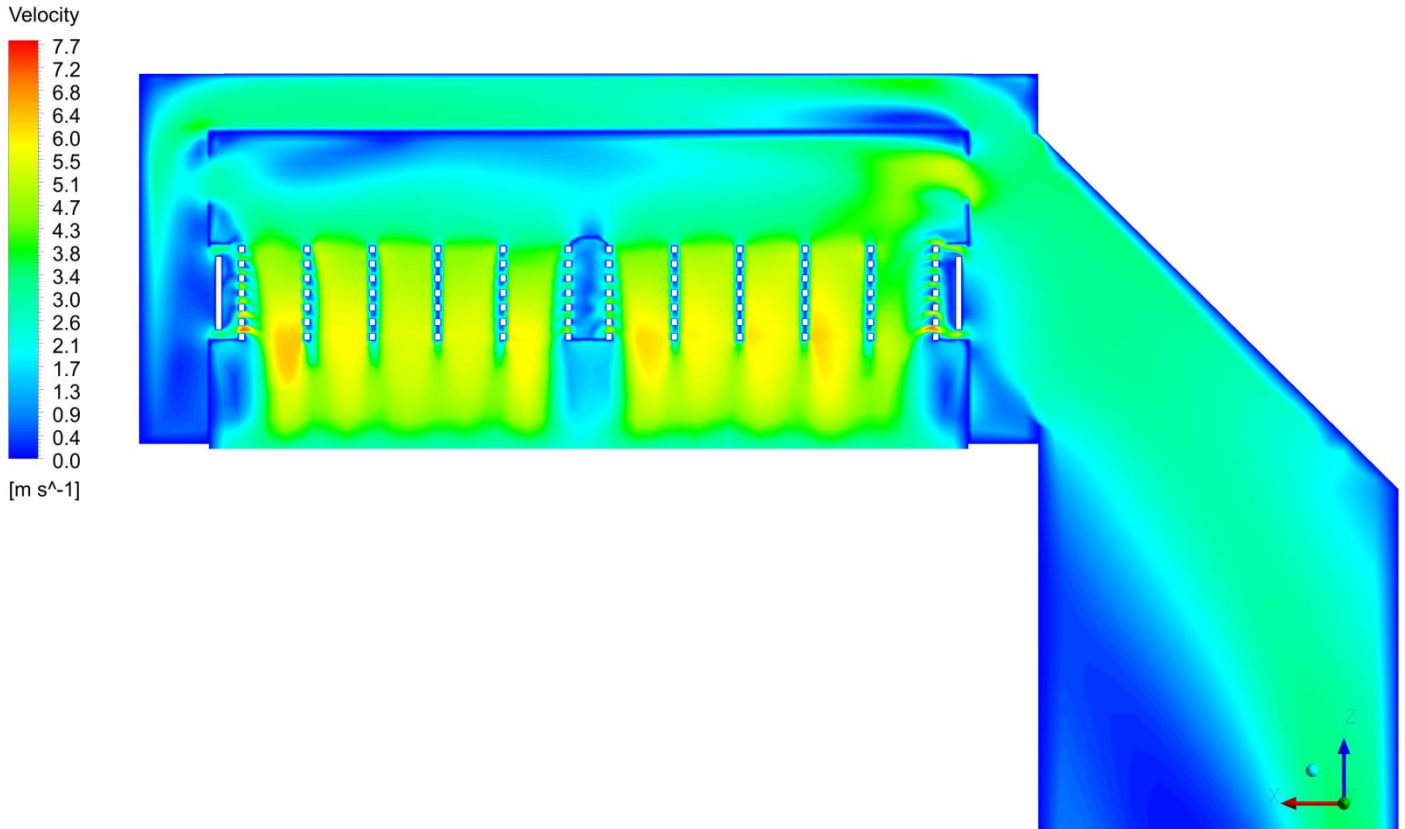
Velocity vectors at plane X2



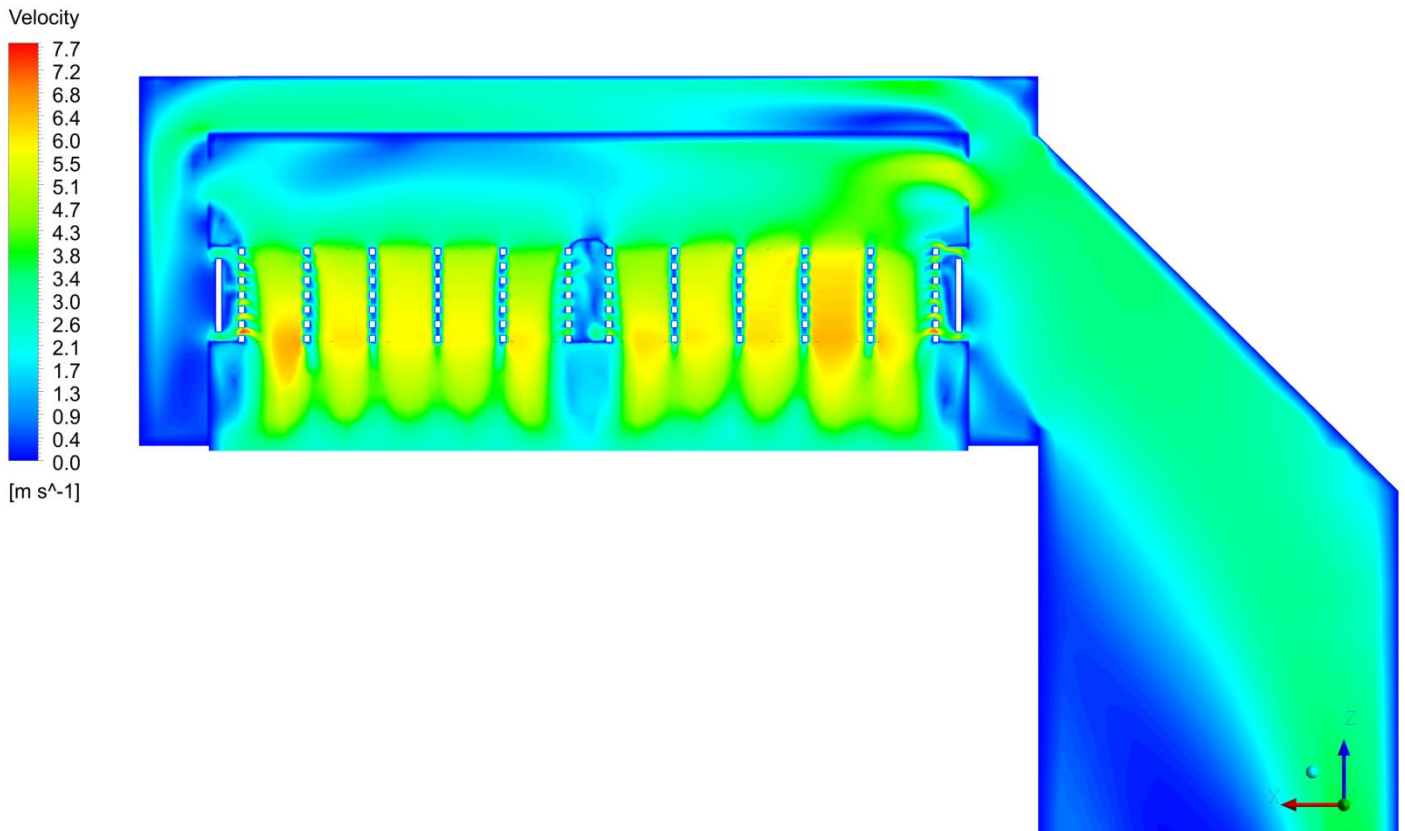
Velocity vectors at plane X5



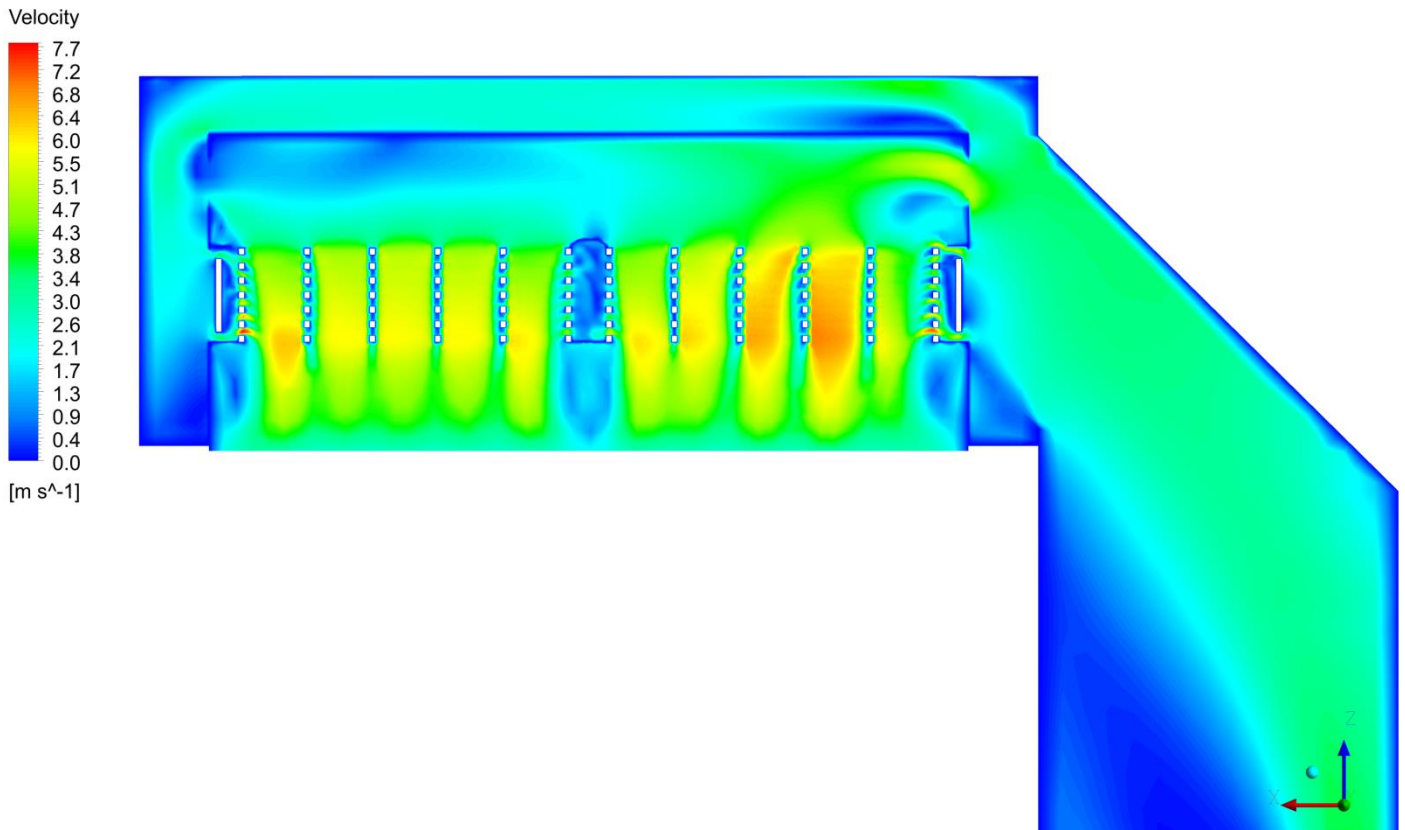
Contours of velocity magnitudes at plane Y1



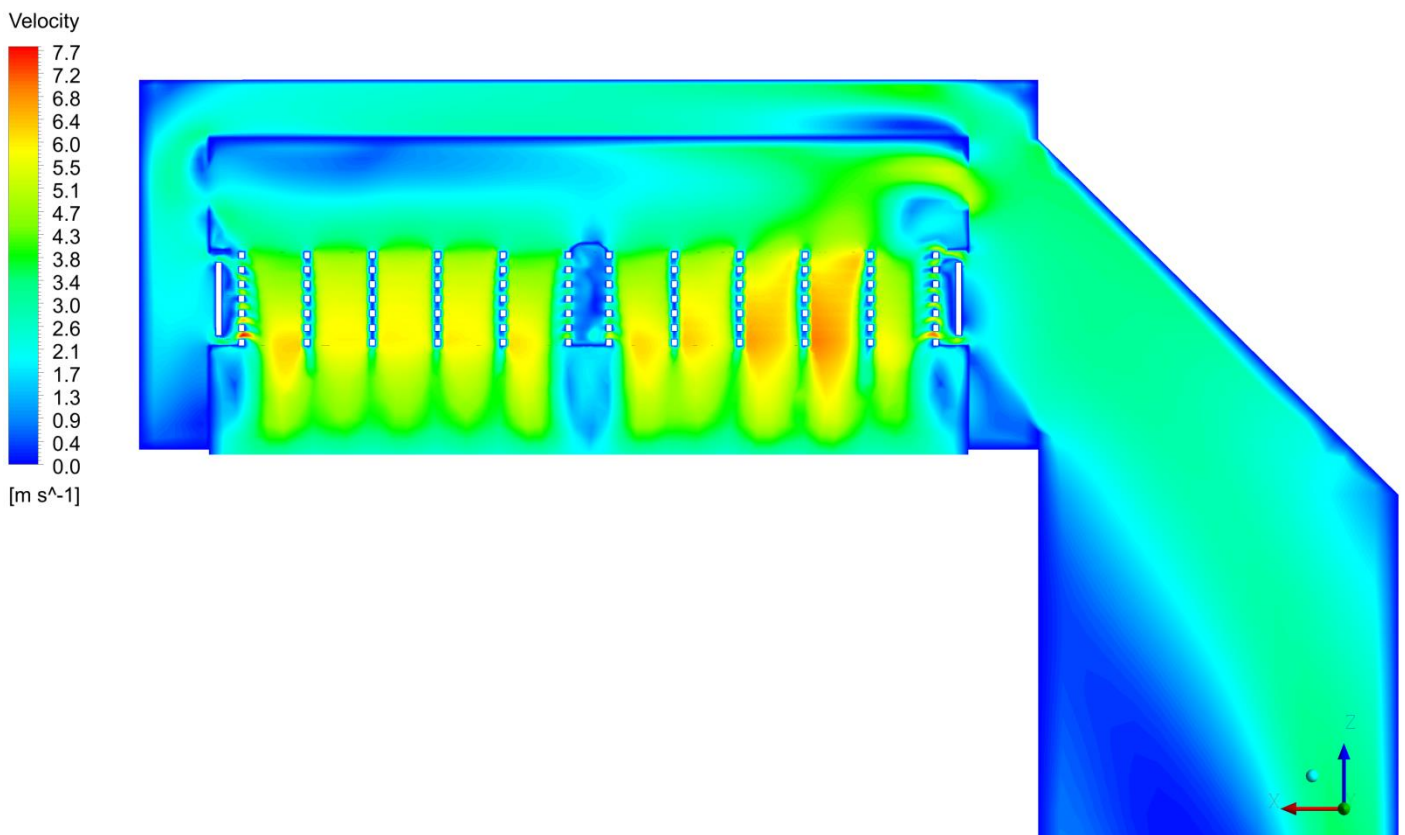
Contours of velocity magnitudes at plane Y2



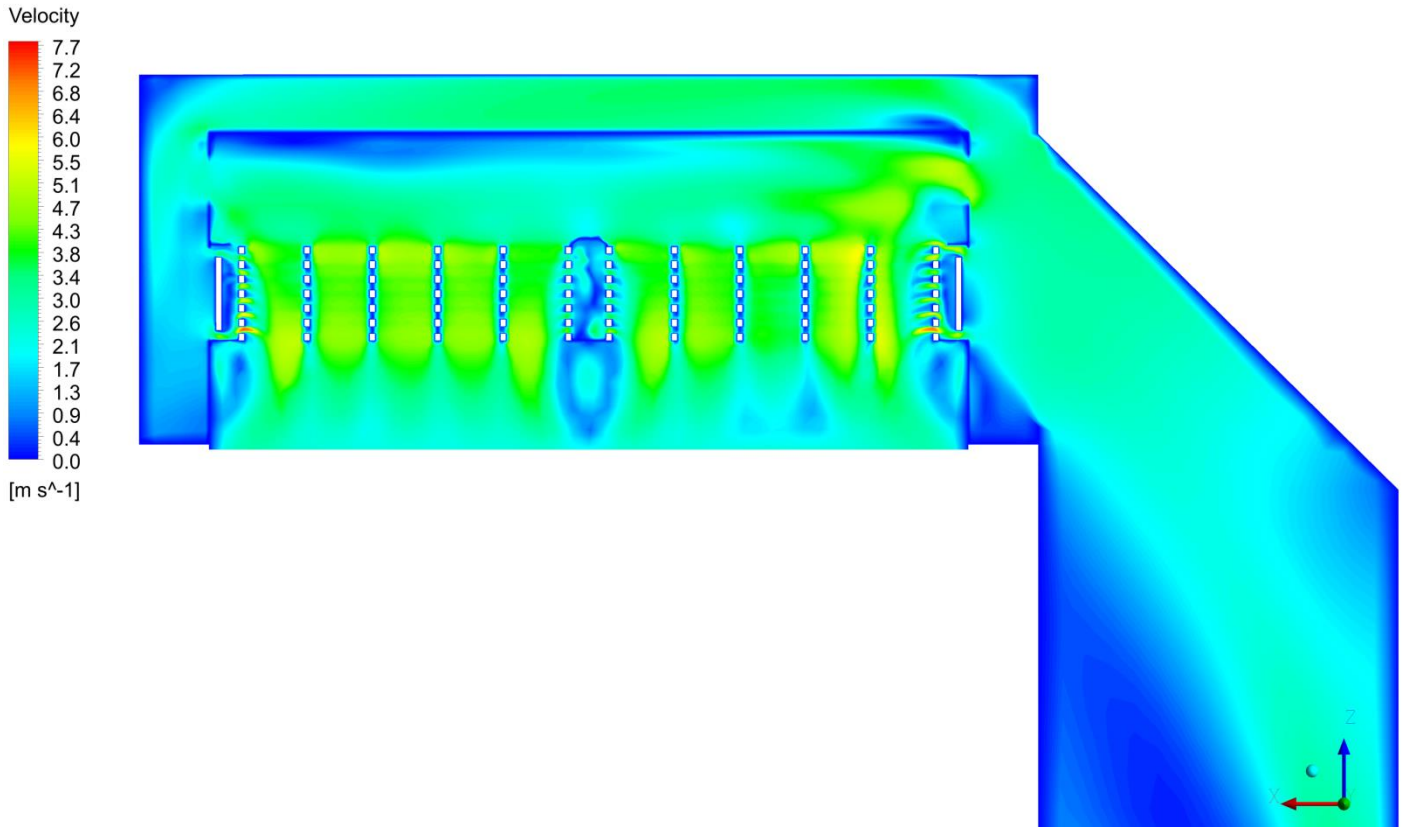
Contours of velocity magnitudes at plane Y3



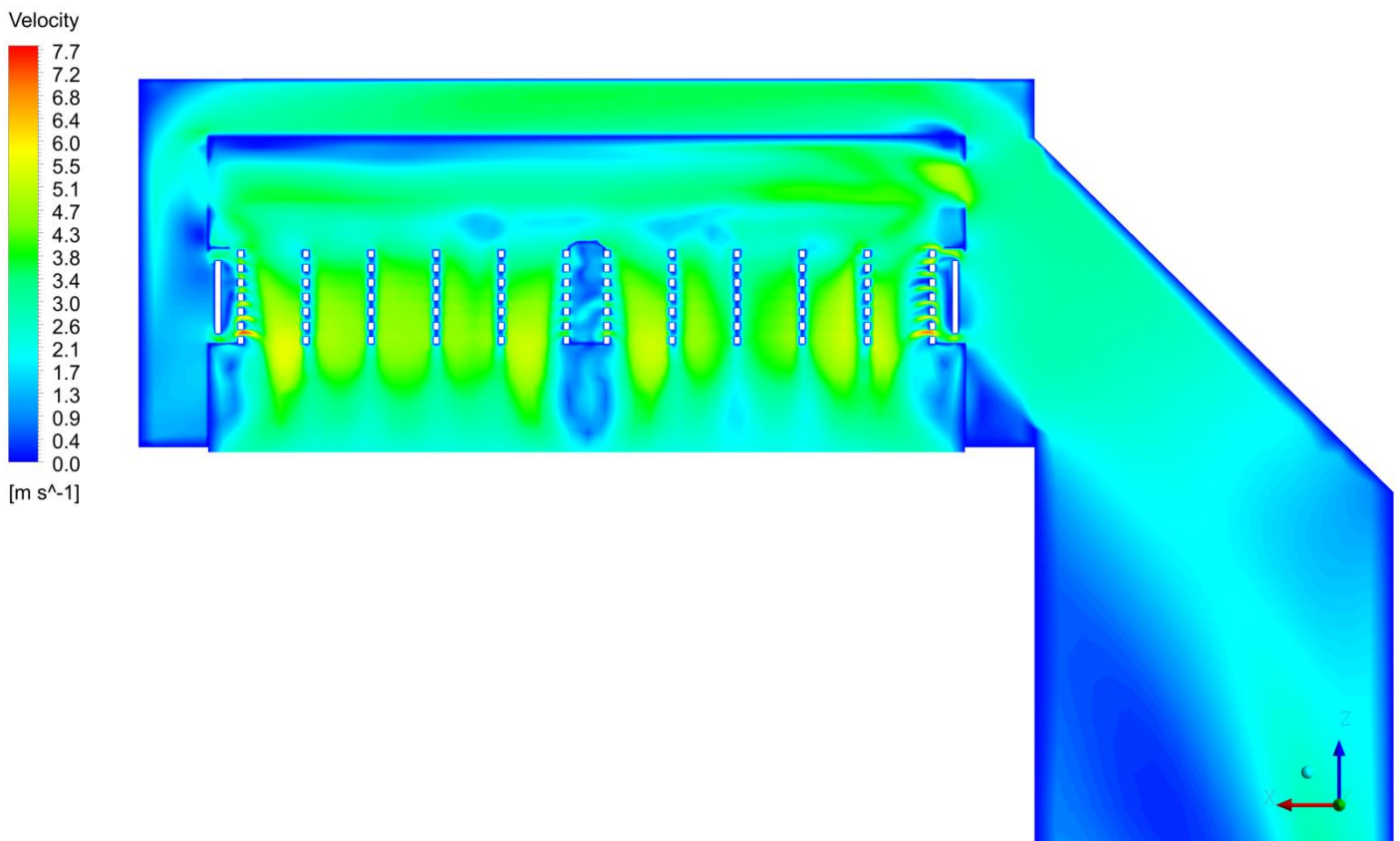
Contours of velocity magnitudes at plane Y4



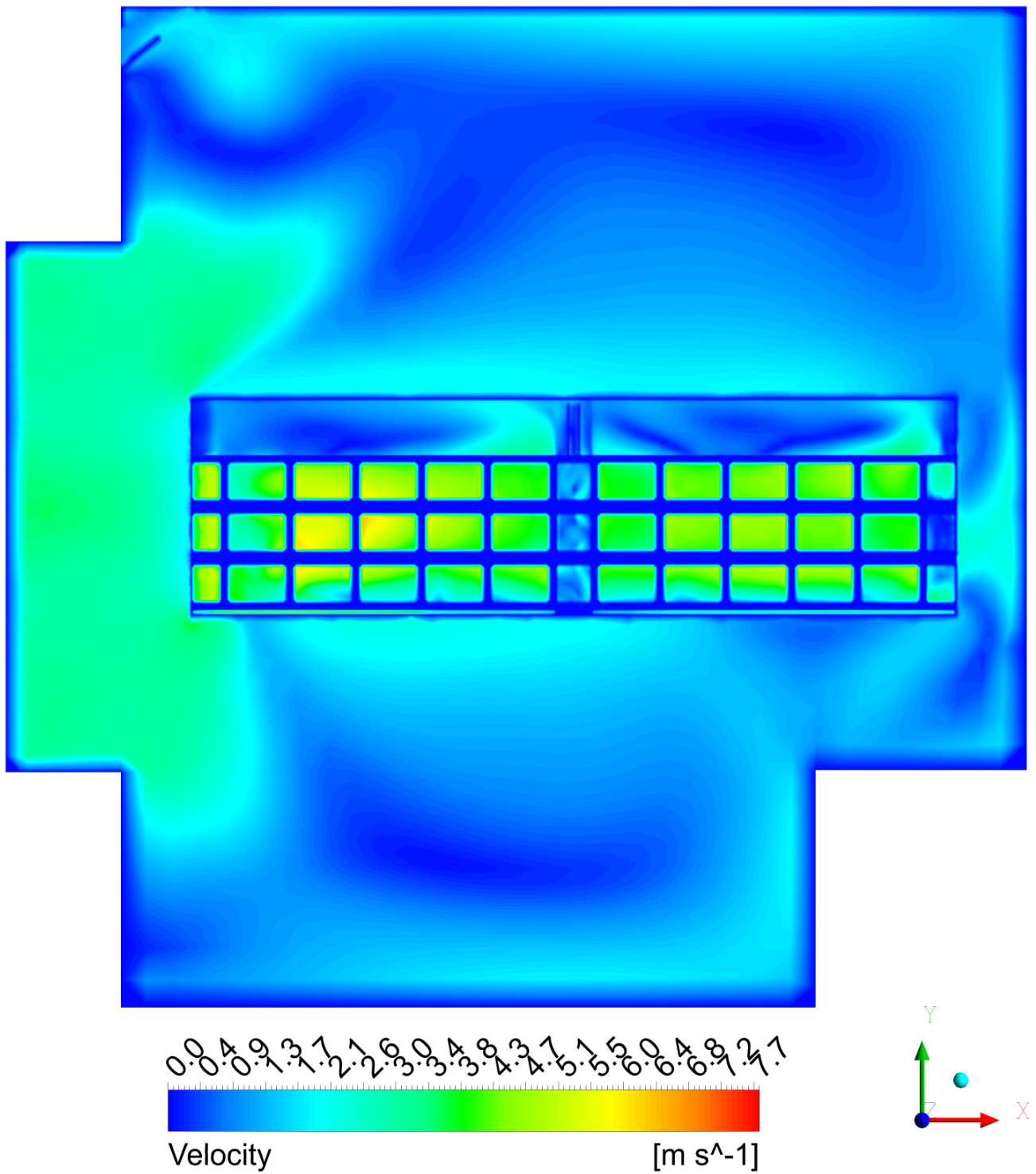
Contours of velocity magnitudes at plane Y5



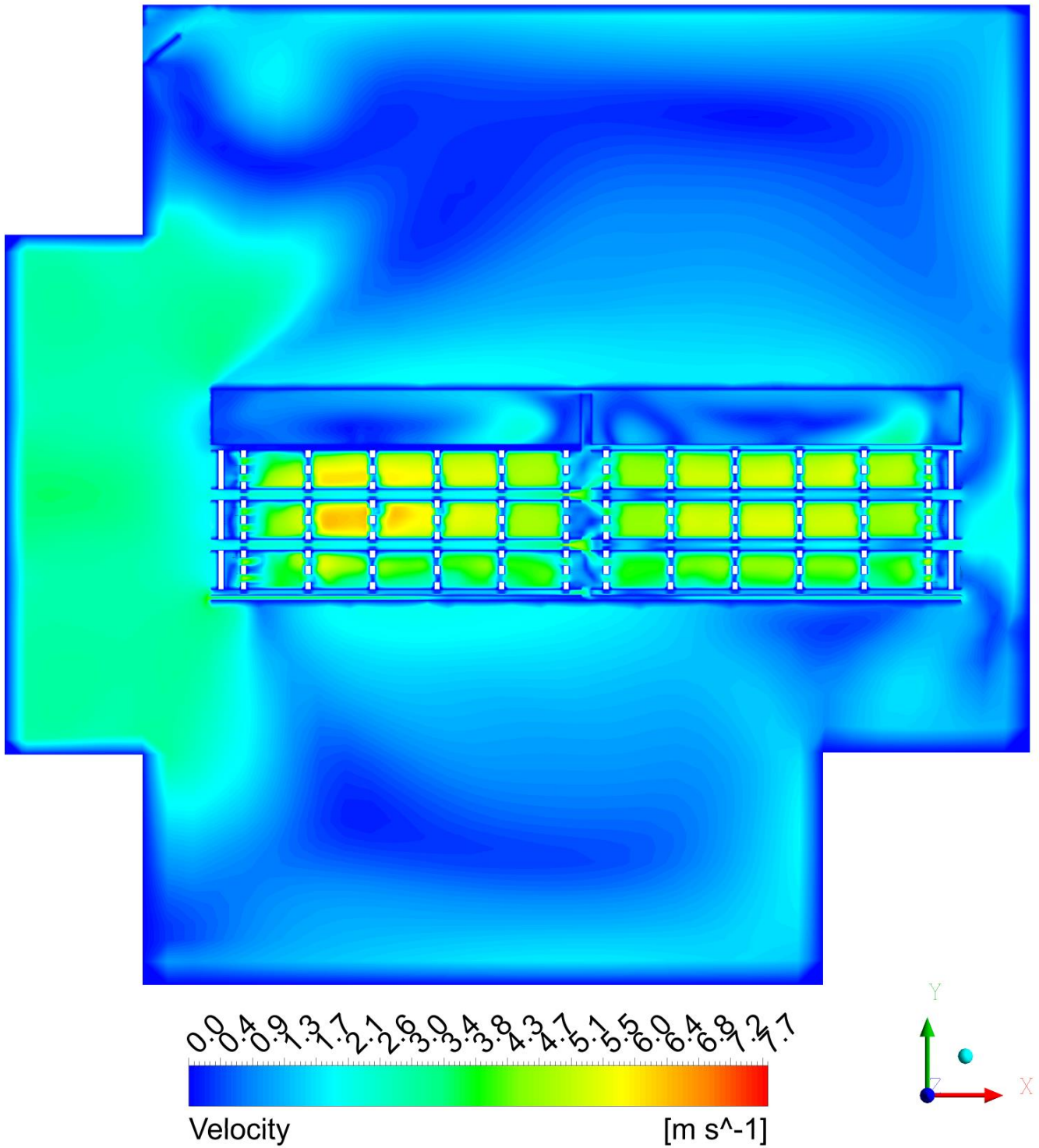
Contours of velocity magnitudes at plane Y6



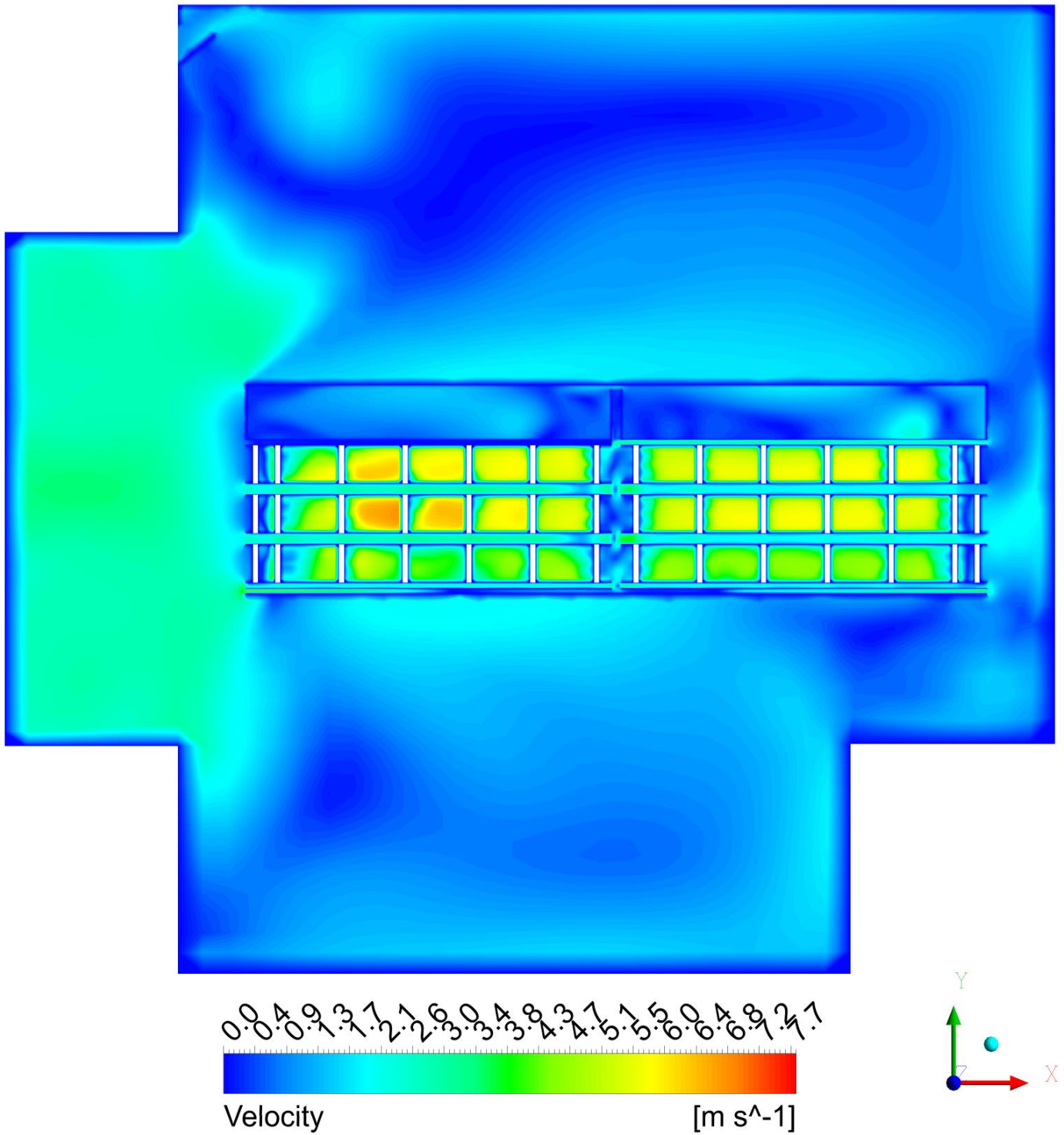
Contours of velocity magnitude at plane Z1



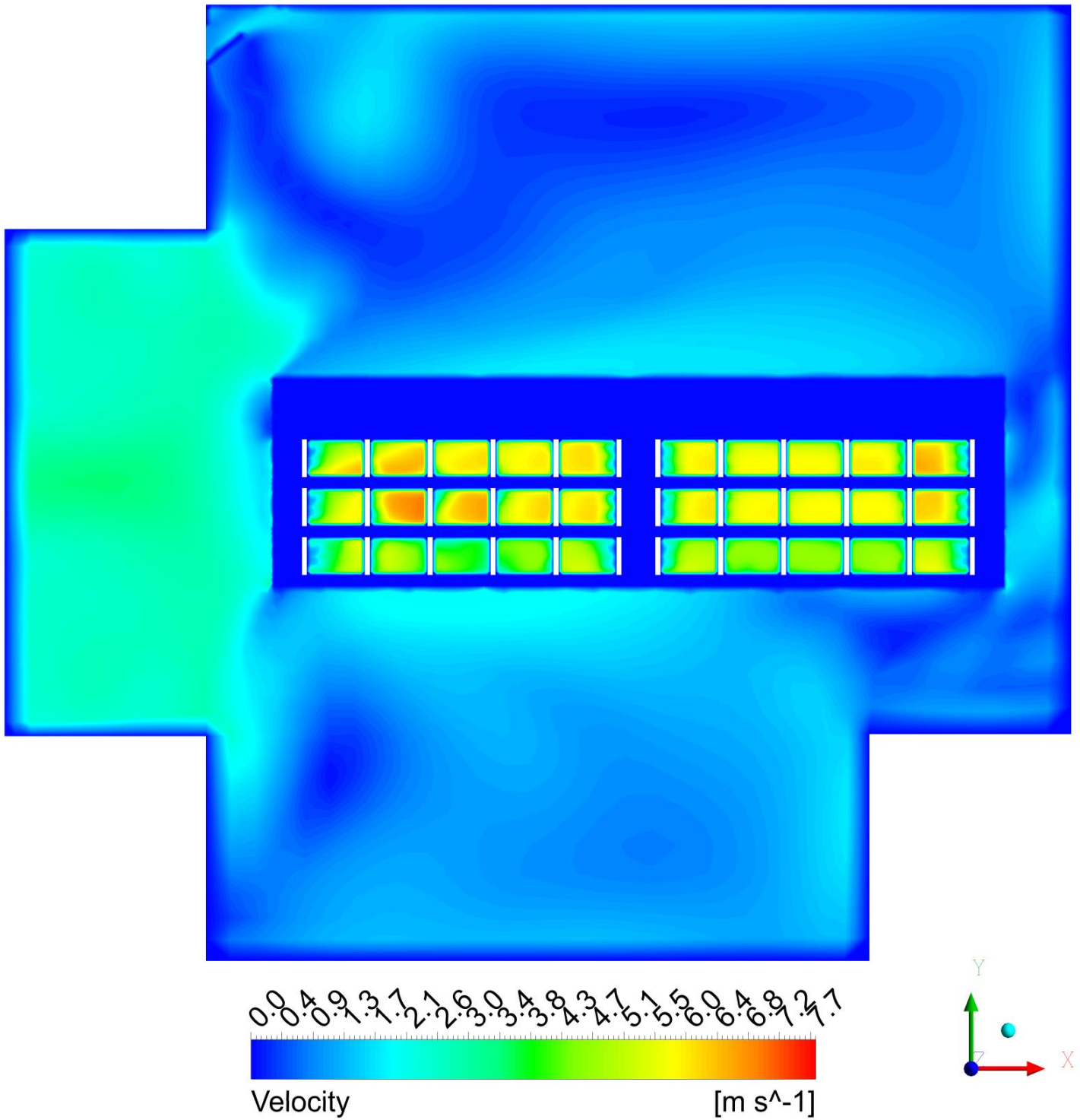
Contours of velocity magnitude at plane Z2



Contours of velocity magnitude at plane Z3

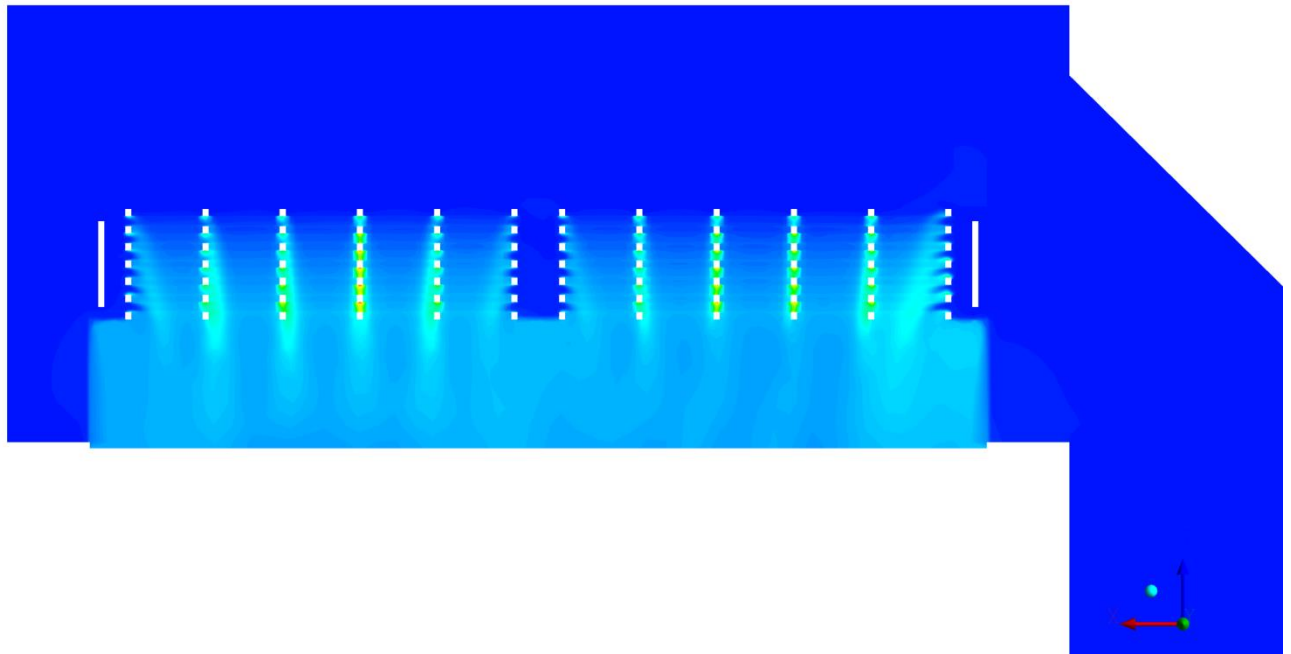
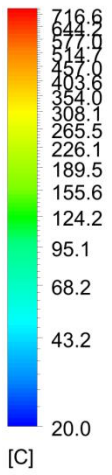


Contours of velocity magnitude at plane Z4



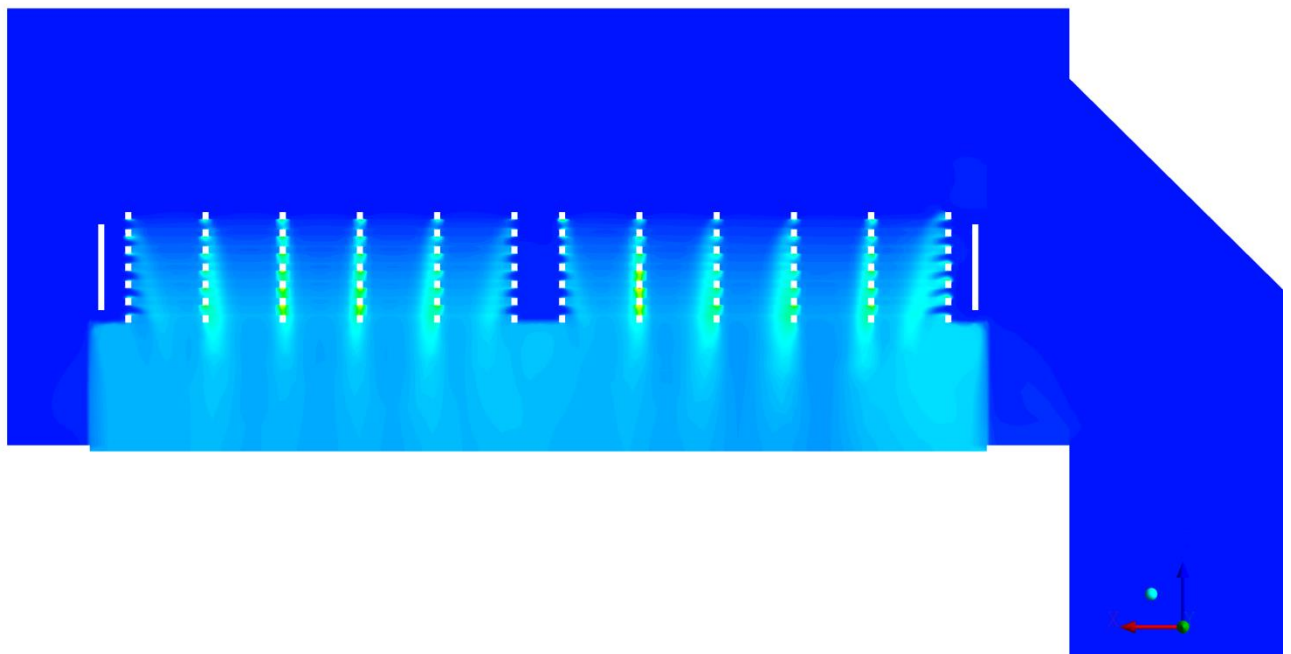
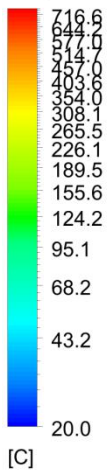
Contours of temperature at plane Y1

Temperature

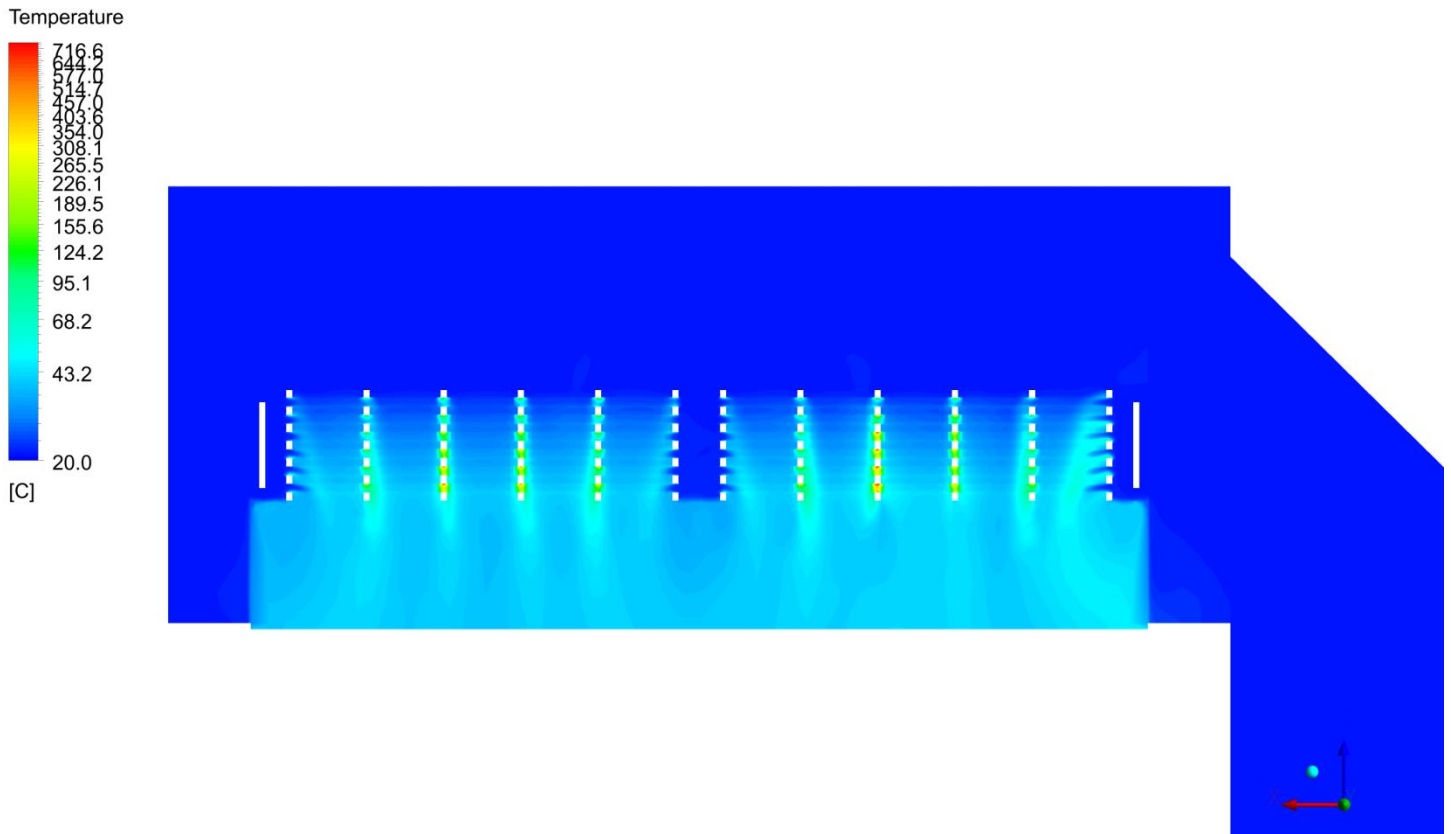


Contours of temperature at plane Y3

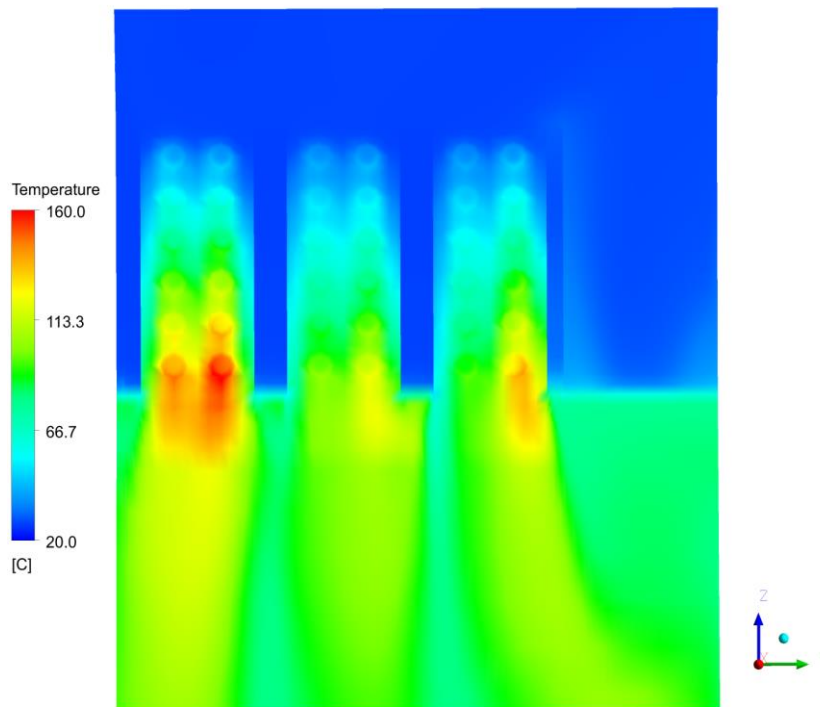
Temperature



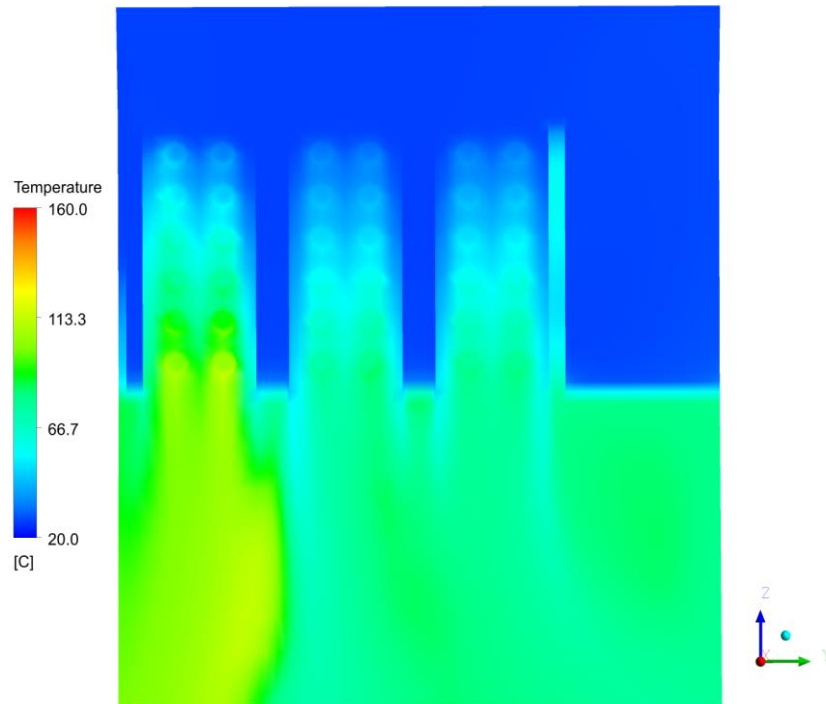
Contours of temperature at plane Y6



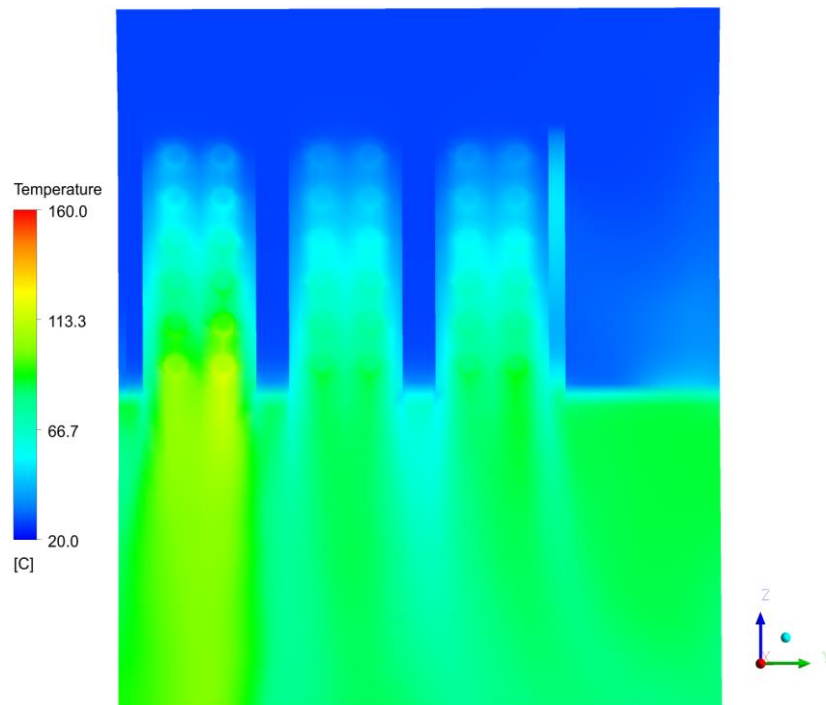
Contours of temperature at plane X1



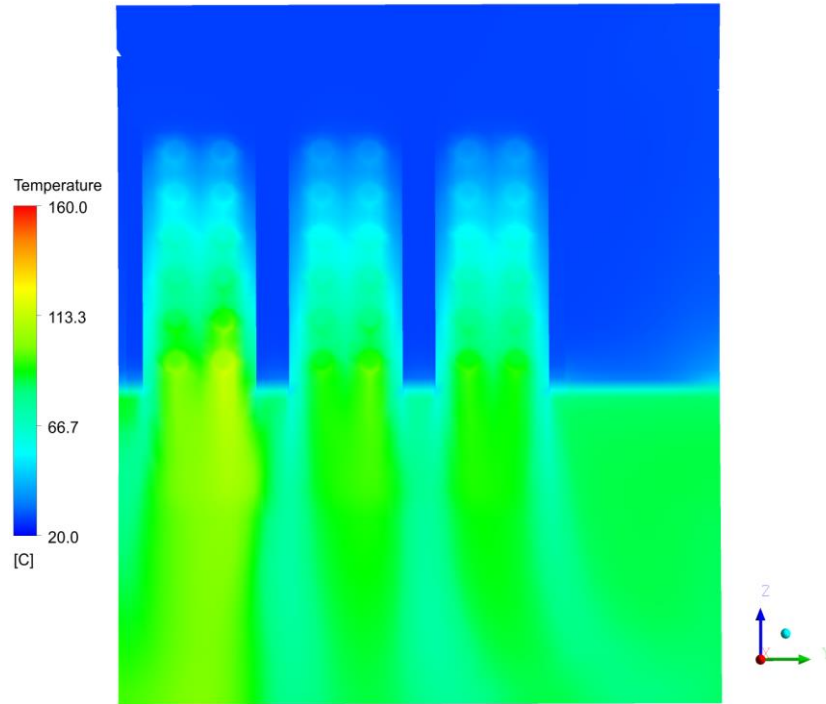
Contours of temperature at plane X2



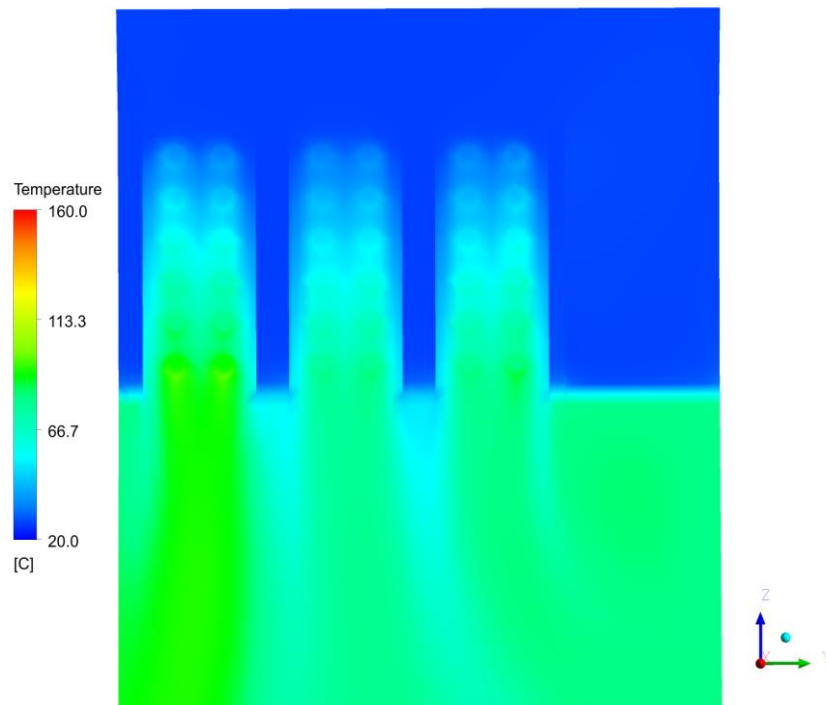
Contours of temperature at plane X3



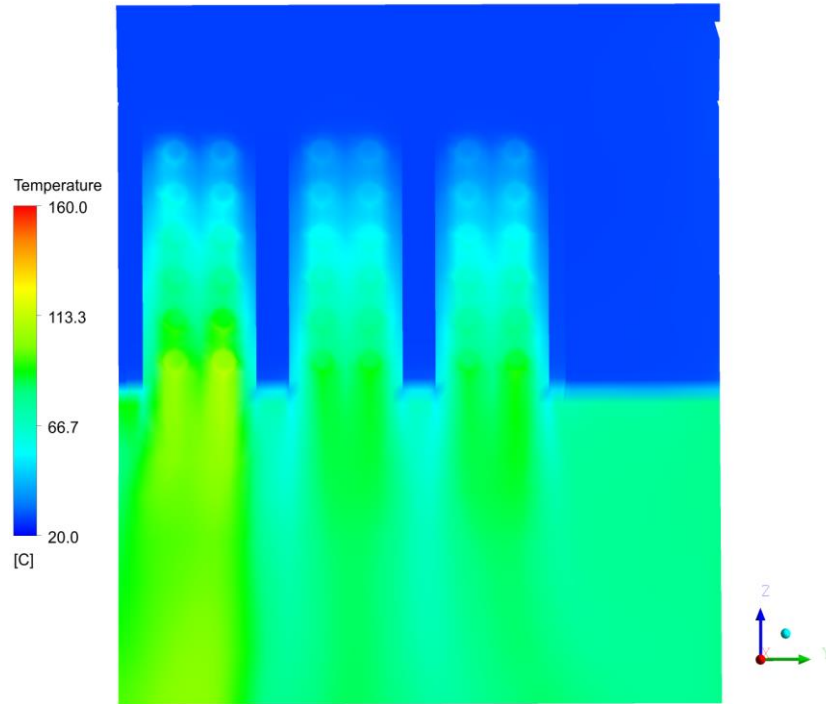
Contours of temperature at plane X4



Contours of temperature at plane X5



Contours of temperature at plane X6



Appendix D – Attached DVD content

- *~/HeatingUDF/* - Compiled version of the Fluent UDF
- *~/Cermak-Martin_MastersThesis_2013.pdf* - PDF version of the thesis
- *~/DryerHeating.exe* - Compiled version of the heat transfer model
- *~/DryerFluent.cas* - Fluent case file
- *~/DryerFluent.dat* - Fluent data file
- *~/DryerMesh.msh* - Mesh file in msh format
- *~/DryerMesh_Gambit.dbf* - Gambit geometry and mesh file
- *~/dist.dat* - Heating unit configuration data file
- *~/FlowData.dat* - Flow field data file (necessary to run the Matlab script)
- *~/HeatingUDF.c* - Fluent UDF source code
- *~/HeatTransferModel.m* - Heat transfer model Matlab code